Numerical phase-field modeling of damage in heterogeneous materials

Seleš, Karlo

UNIVERSITY OF ZAGREB

FACULTY OF MECHANICAL ENGINEEERING AND

NAVAL ARCHITECTURE

Karlo Seleš

NUMERICAL PHASE-FIELD MODELING OF DAMAGE IN HETEROGENEOUS MATERIALS

DOCTORAL THESIS

Zagreb, 2020

UNIVERSITY OF ZAGREB

FACULTY OF MECHANICAL ENGINEEERING AND

NAVAL ARCHITECTURE

Karlo Seleš

NUMERICAL PHASE-FIELD MODELING OF DAMAGE IN HETEROGENEOUS MATERIALS

DOCTORAL THESIS

Supervisor:

Prof. Zdenko Tonković, PhD

Zagreb, 2020

SVEUČILIŠTE U ZAGREBU

FAKULTET STROJARSTVA I BRODOGRADNJE

Karlo Seleš

NUMERIČKO MODELIRANJE OŠTEĆENJA U HETEROGENIM MATERIJALIMA PRIMJENOM TEORIJE FAZNIH POLJA

DOKTORSKI RAD

Mentor:

Prof. dr. sc. Zdenko Tonković

Zagreb, 2020

BIBLIOGRAPHY DATA

UDC:	519.6 : 539 519.6 : 624.044
Keywords:	numerical fracture analysis, phase-field method, finite element method, heterogeneous microstructure, generalized fracture model, crack growth, brittle fracture, ductile fracture, high cycle fatigue, low cycle fatigue, ABAQUS
Scientific area:	Technical sciences
Scientific field:	Mechanical engineering
Institution:	Faculty of Mechanical Engineering and Naval Architecture (FAMENA), University of Zagreb
Supervisor:	Prof. Zdenko Tonković, PhD
Number of pages:	136
Number of pictures:	85
Number of tables:	7
Number of references:	177
Date of oral examination:	28th October 2020.
Jury members:	Assoc. Prof. Tomislav Jarak, PhD, University of Zagreb, Croatia Prof. Jurica Sorić, PhD, University of Zagreb, Croatia Prof. Ferri M.H. Aliabadi, PhD, Imperial College London, United Kingdom Assist. Prof. Tomislav Lesičar, PhD, University of Zagreb, Croatia Dr.-ing, Fadi Aldakheel, PhD, Leibniz University Hannover, Germany
Archive:	FAMENA, University of Zagreb

ACKNOWLEDGMENTS

I wish to express my sincere gratitude to all those whose comments, insights and advices were of great help to me while working on the thesis, and to those who have supported me and been with me during this scientific trip into the unknown.

My deepest gratitude goes to my supervisor Prof. Zdenko Tonković for mentoring me not only in these past 4 years, but also during my undergraduate studies. For the great independence and trust he had granted me in shaping my own research, for utmost support as well as fast and painless resolution of all formalities and paperwork. To Prof. Jurica Sorić, for having me on the project he was leading, for his valuable advices and for connecting me with knowledgeable people in the field of computational fracture mechanics.

I would also like to give my deep appreciation to the Committee members: Assoc. Prof. Tomislav Jarak, Prof. Jurica Sorić, Prof. Ferri Aliabadi, Dr.-Ing. Fadi Aldakheel and Assist. Prof. Tomislav Lesičar for taking their valuable time to read this thesis, provide input and comments regarding the improvement of the thesis quality.

I am deeply thankful to Prof. Laura de Lorenzis from ETH Zürich, and her team at TU Braunschweig, many of whom have moved to other positions and locations since. The experience and knowledge acquired during my research visits to TU Braunschweig proved invaluable for my research, while work atmosphere and leisure activities brought me great joy and immanently changed my perspectives towards scientific community. Thank you for accepting me into your extended scientific family! In that sense, special thank goes to Dr.-Ing. Marreddy Ambati for his selfless help, utmost patience and valuable answers to my countless questions.

I wish to express my genuine gratitude to Dr.-Ing. Fadi Aldakheel for the ongoing collaboration, for spending many hours over skype calls, for his helpful advices, and for trusting my ideas. Important thanks go to Prof. Nenad Gubeljak and Primož Štefane from TU Maribor, for their experimental work on the fracture of acrylic glass specimens, which in the end unfortunately, could not be incorporated in this thesis. Special thanks go to Predrag Čanžar from KONČAR Electrical Engineering Institute for providing me with valuable experimental data obtained during the nodular cast iron fatigue testing.

Sincere thanks go to all my dear friends and colleagues, professors and staff of the Faculty of Mechanical Engineering and Naval Architecture in Zagreb, especially the Chair of Mechanics and Strength of Materials, and the Laboratory of Numerical Mechanics (LNM). I am truly grateful to my co-workers Ante Jurčević and Zoran Tomić who ran my codes extensively, found bugs and extracted many results. Thank you for your patience, trust and great efforts which contributed in the creation of this thesis! My deepest thanks go to Dr. sc. Lana Virag for countless proofreading and invaluable advices and comments on work- and non-work-related matters. I am thankful to Assist. Professor Tomislav Lesičar for his advices in the early stages of research, to Dr. sc. Boris Jalušić for his selfless help and advices, and to Assoc. Professor Tomislav Jarak for interesting remarks and conversations. In that sense, I would also like to thank Assist. Profesor Ivica Skozrit and Assoc. Professor Igor Karšaj. I am genuinely grateful to Nino Horvat for our endless conversations on number of interesting topics and big ideas which provided me with motivation beyond this scientific pursuit. To Matija Novak for helping me keep mind of work and updating me on sports. A pleasant and friendly work atmosphere made my office hours an enjoyable experience. Special thanks for keeping the atmosphere light to all my yet-unmentioned past and present colleagues (in alphabetical order): Daria Ćurko, Dr. sc. Damjan Čakmak, Bruno Dogančić, Joško Frančeski, Tomislav Polančec, Dr. sc. Filip Putar, Dr. sc. Marija Smoljkić, Toni Škugor, Ivan Trapić, Josip Živić and to our Head of Office Begzada Pinjić.

I am eternally grateful to all my friends I met at various stages of life; friends from my hometown, friends I met in Zagreb and around the world. A sincere *thank you* goes to each and every one of you for all the good and bad times spent together, and for being a big part of my life!

Words cannot express my thanks to my closest family for their unconditional love, trust and independence, and for utmost support. To my love, Ana Marija, thank you for tolerating me, inspiring me and amazing me through all these years.

Thank you,
Karlo Seleš

Zagreb, September 2020

SPECIAL ACKNOWLEDGEMENTS

I wish to express my genuine gratitude to the Croatian Science Foundation, which financed the research conducted in this thesis through the project “Multiscale numerical Modeling of Material Deformation Responses from Macro- to Nanolevel (2516)” led by Prof. Jurica Sorić, and funded me through "Young researchers' career development project – training of doctoral students" with my mentor Prof. Zdenko Tonković.

Karlo Seleš

Zagreb, September 2020

ABSTRACT

Material failure is still one of the central issues in modern engineering. Its prediction and prevention are being tackled early in the product design stage. Materials used in modern engineering often exhibit significant microstructural heterogeneity. The size, shape, distribution and properties of microconstituents considerably influence the heterogeneous material properties. Nowadays, numerical simulations play an essential role in component design and material development, gradually supplanting and replacing expensive and time-consuming experiments. However, it is worth noting that many complex fracture processes occur at microstructural scale making the fracture analysis an especially challenging and interesting problem.

One of the methods for the numerical modelling of fracture capable of efficiently recovering these complex fracture processes is the recently emerged phase-field method. It approximates the sharp crack discontinuity with a diffusive band regulated by a length-scale parameter, thus separating the broken and intact material states. Although extensive research has been carried out on the development of phase-field fracture theory over the past decade, certain challenges still exist in the computational implementation of the method. Within the finite element framework, a fine spatial discretization is often required to resolve the smooth phase-field distribution regulated by a small length scale parameter. Thus, coupling phase-field method with an inefficient solution scheme can be computationally rather expensive.

In this work, a novel generalized phase-field framework capable of simultaneously recovering brittle, ductile, and fatigue fracture in three-dimensional settings is developed. The robustness and accuracy of the results is ensured by the development of an efficient residual control algorithm and its implementation in the commercial finite element software ABAQUS. Major advantage of such implementation is the high usability of different underlying solvers, convergence criteria and other additional options including automatic incrementation, element deletion, coupled contact analysis, thread parallelization or restart analyses, used and thoroughly discussed in this work. The full source code together with the presented examples and explanations is made publicly available, thus promoting the phase-field fracture methodology.

The proposed implementation is exhaustively tested on a large number of different benchmark examples, verified and validated in comparison with numerical and experimental data from available literature. The importance of a stopping criterion within a staggered scheme is emphasised in the illustrative examples. The detailed discussions regarding the proposed implementation's accuracy and CPU time usage are provided. Special attention is given to the verification of fatigue fracture examples through the parametric study. Main features of fatigue, including Wöhler and Paris law curves in low- and high-cycle regimes, are easily recovered without any additional criteria. The cycle skipping technique is implemented to allow for the calculation of a very high number of cycles on moderate size examples. Finally, the potential of the implementation is demonstrated on the different-sized samples of nodular cast iron with their actual heterogeneous microstructure obtained from microtomography. Specimens are tested in both monotonic and cyclic loading regimes. The results clearly show the size-effect behaviour as well as the influence of microstructural topology on fracture patterns.

KEYWORDS: Numerical fracture analysis, phase-field method, finite element method, heterogeneous microstructure, generalized fracture model, crack growth, brittle fracture, ductile fracture, high cycle fatigue, low cycle fatigue, ABAQUS

PROŠIRENI SAŽETAK

UVOD

Neke od glavnih karakteristika modernih konstrukcija i strojnih komponenti su njihova sve veća složenost te učestalo korištenje novo razvijenih materijala s poboljšanim svojstvima. Time se zadovoljavaju potrebe za iznimnom sigurnošću, pouzdanošću i trajnošću, istovremeno zadovoljavajući visoke zahtjeve učinkovitosti i niskih cijena izrade, održavanja i upravljanja. Povećanje životnog vijeka komponenti također je važan čimbenik u rješavanju gorućih pitanja kao što su klimatske promjene i očuvanje okoliša. Degradacija i lom materijala još su uvijek problemi koji često dovode do materijalnih i financijskih gubitaka uzrokovanih oštećenjima proizvoda i neisporučenim uslugama, ili u ekstremnijim slučajevima, dovode do gubitaka života. Prema tome, predviđanje i prevencija pojave oštećenja i loma materijala u ranoj fazi konstruiranja nedvojbeno su iznimno važni, i kao takvi, od velikog su interesa mnogim inženjerima i istraživačima.

Numeričke simulacije nezaobilazan su dio konstruiranja proizvoda i razvoja novih materijala. Nakon odgovarajuće validacije, numeričke simulacije nadopunjuju te ponekad i u potpunosti zamjenjuju često skupe i dugotrajne eksperimente, smanjujući broj potrebnih prototipa i olakšavajući plansko održavanje.

Većina materijala koji se koriste u modernim konstrukcijama i strojnim komponentama sadrži određenu razinu mikrostrukturne heterogenosti. Razni geomaterijali poput betona i stijena, čelici visoke čvrstoće, kompoziti i polimeri, ili materijali dobiveni postupcima poput sinteriranja ili aditivne proizvodnje (3D printanja) samo su neki od primjera takvih mikrostrukturno heterogenih materijala. Na njihova materijalna stvojstva u velikoj mjeri utječu pojedinačna svojstva mikrokonstituenata te njihova veličina, oblik i raspodjela. Upravo se na mikrostrukturnoj razini pojavljuje većina složenih procesa loma kao što su lokalizacija oštećenja, nastanak, propagacija, grananje i srastanje pukotina, što analizu loma heterogenih mikrostruktura čini izrazito izazovnom i zanimljivom.

Stoga su numeričke analize oštećenja i loma heterogenih materijala koje u obzir uzimaju mikrostrukturnu topologiju i svojstva mikrokonstituenata važan čimbenik u procjeni pouzdanosti i strukturalne cjelovitosti, kao i predviđanju radnog vijeka modernih konstrukcija i strojnih komponenata. Također bi mogle dovesti do realnijeg opisa ponašanja materijala čime

bi se olakšao razvoj novih materijala s poboljšanim svojstvima koja proizlaze iz manipulacije mikrostrukturom. Time bi se omogućila proizvodnja učinkovitijih, sigurnijih i jeftinijih konstrukcija izrađenih od heterogenih materijala.

MODELIRANJE OŠTEĆENJA I LOMA

Numeričke metode modeliranja oštećenja i loma najčešće su razvijene u sklopu metode konačnih elemenata (MKE). MKE se temelji na konceptu podjele fizikalnog modela na manje segmente (elemente) jednostavne geometrije i konačnog broja stupnjeva slobode. Takav se diskretni model, koji se sastoji od mreže konačnih elemenata, može opisati sustavom algebarskih jednadžbi i jednostavno riješiti.

Numeričke metode modeliranja oštećenja i loma općenito se mogu podijeliti na diskretne i difuzne (tj. kontinuumske) prema načinu njihovog opisa oštećenja, odnosno loma. Diskretne metode pukotinu opisuju kao oštar geometrijski diskontinuitet u polju pomaka. Najpoznatije i najčešće korištene diskretne metode su metoda modeliranja kohezivnih zona (eng. *cohezive zone modelling*, CZM), razni algoritmi lokalne promjene mreže konačnih elemenata (eng. *remeshing*) te tehnike obogaćivanja konačnih elemenata čiji je najpoznatiji predstavnik proširena metoda konačnih elemenata, XFEM (eng. *extended finite element method*). Iako su se diskretne metode do sada pokazale točnim i vrlo korisnim u predviđanju oštećenja i loma, uz neizbježno korištenje dodatnih kriterija nastajanja i rasta pukotina, njihov najveći problem zapravo je numeričko praćenje diskontuiteta, odnosno pukotine. Tako kod pristupa koji se temelje na metodi konačnih elemenata pukotina raste samo duž rubova elementa što uzrokuje problem ovisnosti rezultata o veličini mreže (eng. *mesh dependency*) i problem ovisnosti rasta pukotine o usmjerenosti konačnih elemenata (eng. *bias dependency*). Taj problem najviše dolazi do izražaja pri složenim topologijama loma kakve se očekuju na miktrostrukturnim geometrijama ili složenim trodimenzijskim problemima. Posljednjih godina razvijene su i brojne bezmrežne metode koje omogućuju modeliranje razvoja pukotina bez *remeshinga*, kao npr. bezmrežna Galerkinova metoda (eng. *Element-free Galerkin*, EFG). Iako se često koriste za modeliranje linearnih i nelinearnih problema rasta pukotina, u usporedbi s MKE, takve metode imaju nekoliko još neriješenih problema među kojima se najviše ističe numerička nestabilnost i dugo vrijeme računanja.

S druge strane, kontinuumske metode modeliranja oštećenja i loma, umjesto modeliranja diskretne pukotine i stvaranja novih površina, uvode parametar oštećenja na razini integracijske

točke. Njime se kontrolira krutost materijala što omogućuje smanjenje naprezanja uzrokovano stvaranjem pukotine. U modelima utemeljenim na pretpostavci standardnog ili tzv. lokalnog kontinuuma pojavljuje se lokalizacija oštećenja koja uzrokuje lokalni gubitak eliptičnosti sustava diferencijalnih jednadžbi, zbog čega numerička rješenja često ne konvergiraju prema fizikalno smislenom rješenju. Kao što je ranije spomenuto, to se u okviru MKE-a očituje rezultatima ovisnim o gustoći i usmjerenosti mreže konačnih elemenata. Navedeni problemi riješeni su uvođenjem nelokalnih i gradijentno-poboljšanih kontinuumskih pristupa. Zajedničko svojstvo takvih modela je dodavanje parametra duljinske skale čime se omogućuje i računanje efekta veličine uzorka (eng. *size-effect*), što nije moguće s modelima temeljenim na pretpostavkama lokalne mehanike kontinuuma. Poznati nedostatci takvih, sad već standardnih, ne-lokalnih pristupa jesu rast zone oštećenja okomito na smjer rasta pukotine. Iako se taj nedostatak uspješno rješava uvođenjem parametra duljinske skale kao funkcije naprezanja, fizikalna utemeljenost takve pretpostavke je upitna. Drugi način rješavanja navedenog problema je primjena kontinuuma višeg reda (gradijentne, nelokalne i mikrokontinuumske teorije), međutim, to neizbježno uvodi nove komplikacije tokom numeričke ugradnje navedenih modela.

MODELIRANJE HETEROGENIH MATERIJALA

Iako je pretpostavka homogenosti materijala na materijalnoj točki makrorazine još uvijek valjana u mnogim primjerima iz inženjerske prakse, razvoj naprednih materijala korištenih u modernim konstrukcijama zahtijeva razmatranje materijalne mikroheterogenosti i njezinog utjecaja na konstitutivno ponašanje materijala na makrorazini. Eksperimentalne tehnike također su znatno napredovale u procjeni mikrostrukturne heterogenosti. Najbolji primjer je 3D rendgenska mikrotomografija koja je sada u stanju rutinski generirati realistične geometrijske modele mikrostruktura mnogih materijala na raznim skalama. Jedan od načina numeričkog modeliranja heterogenosti upotreba je izravnih numeričkih simulacija (eng. *direct numerical simulation,* DNS) pri čemu se heterogena mikrostruktura detaljno modelira izravno na makrorazini. To je ujedno i najpreciznija metoda za numeričku predikciju loma u heterogenim materijalima. Međutim, računalno je vrlo zahtjevna, posebno kad se radi o velikim razlikama između skala što zahtjeva vrlo gustu diskretizaciju konačnim elementima. S druge strane, razvijene su i višerazinske metode koje na odgovarajući način razdvajaju i prenose rješenja između različitih skala. Najpopularnija takva metoda zasigurno je računalna homogenizacija (eng. *computational homogenization*) koja uprosječuje rezultate dobivene

analizom problema na mikrostrukturnoj razini, te ih prosljeđuje numeričkom modelu na makrorazini. Takva analiza provodi se na tzv. reprezentativnim volumenskim elementima (RVE). Računalna homogenizacija standardno se koristi u problemima elastičnog i elastoplastičnog ponašanja materijala te spregnutih termomehaničkih problema. Također, razvijene su i metode računalne homogenizacije drugog reda koje u obzir uzimaju i gradijente deformacije na makrorazini koristeći prethodno spomenute modele kontinuuma višeg reda. Međutim, kad je u pitanju modeliranje oštećenja i loma, još uvijek postoje veliki problemi i otvorena pitanja u računalnim metodama homogenizacije. Možda i najvažnije, odnosi se na upitno postojanje RVE-a prilikom pojave oštećenja i loma. Naime, po svojoj definiciji, RVE gubi svoju statističku reprezentativnost prilikom lokalizacije oštećenja i pojave loma. Iako alternativne homogenizacijske sheme ukazuju na mogućnost rješavanja ovog problema za kvazi-krhke materijale, čini se da je dosljedna i pouzdana primjena višerazinskih metoda predikcije oštećenja i loma na realnim konstrukcijama još uvijek daleko. Prema tome, razvoj pouzdanih modela predikcije oštećenja i loma na vrlo složenim geometrijama kakve se javljaju na mikrorazini heterogenih materijala područje je od velikog interesa. Razvoj takvih modela uz razmatranje stvarne topologije mikrostrukture nudi način za preciznije modeliranje složenih procesa loma u heterogenim materijalima te je detaljnije obrađen u ovom radu.

TEORIJA FAZNOG POLJA

Teorija faznog polja (eng. *phase-field modelling*) postala je iznimno popularna u posljednjem desetljeću. Primjena metode u području modeliranja loma samo je jedna od mogućnosti ove teorije. Općenito, ona se uspješno koristi za modeliranje sustava s oštrim prijelazima između faza, kao što je npr. interakcija između fluida i čvrstih tijela (eng. *fluid-solid interaction*). U teoriji faznog polja, uvodi se kontinuirana varijabla čijim se glatkim prijelazom razlikuju fizičke faze unutar određenog sustava. U slučaju loma, ova varijabla razdvaja oštećeni i neoštećeni dio materijala aproksimirajući, na taj način nagli diskontinuitet pukotine difuznim pojasom. Širina takvog pojasa regulirana je parametrom duljinske skale. Prema tome, teorija faznog polja može se svrstati u kontinuumske metode modeliranja oštećenja i loma. Zanimljivo je da je metoda neovisno razvijena od strane dvije znanstvene zajednice, fizičara i inženjera, čiji se pristupi i polazišne točke za dobivanje osnovnih jednadžbi razvoja loma pomoću faznog polja znatno razlikuju. S jedne strane, zajednica fizičara razvila je modele predviđanja dinamičkih lomova koristeći Ginzburg-Landau teoriju, izvorno izvedenu za elektromagnetske fenomene faznih prijelaza. S druge strane, modeliranje loma metodom faznog polja na kojoj se

temelji ovaj rad, potječe od varijacijskog pristupa krhkom lomu gdje je osnovna Griffithova teorija loma pretvorena u problem minimizacije energije. Takav princip nalaže da pukotina može nastati ili rasti u čvrstom tijelu ukoliko tako rezultirajuća konfiguracija ima nižu ukupnu energiju u usporedbi s ostalim konfiguracijama u kojima nema nastajanja ili rasta pukotine. Smjerovi rasta pukotine prirodno se definiraju kao oni koji vode u konfiguraciju s minimalnom ukupnom energijom. Pukotine se mogu granati ili spojiti ukoliko to dovodi do konfiguracije s nižom energijom od jednostavnog rasta postojećih pukotina, bez potrebe za uvođenjem dodatnih kriterija rasta oštećenja i loma. Regularizacijom tako izvedenog energijskog funkcionala dobiva se sustav parcijalnih diferencijalnih jednadžbi koje u potpunosti određuju nastanak i rast pukotine. Upravo su prethodno navedene činjenice razlog popularnosti ove metode, koja se pokazala izrazito uspješnom u rješavanju složenih procesa loma, uključujući nastanak, rast, grananje i srastanje pukotina. Također, aproksimacijom diskretne topologije pukotine na fiksnoj mreži konačnih elemenata zaobilazi se složeni problem praćenja površina pukotina i značajno se pojednostavljuje numerička implementacija, posebno u trodimenzijskim postavkama. U zadnje vrijeme razvijen je velik broj takvih modela s različitom primjenom kao što su modeli faznog polja za predviđanje krhkog i duktilnog loma ili multifizikalni problemi kao što su lom uzrokovan termomehaničkim, elektromehaničkim ili hidrauličkim djelovanjem, što također pokazuje veliki potencijal ove metode.

Međutim, velika većina ovih modela uglavnom je verificirana kroz usporedbe sa standardnim numeričkim primjerima (*benchmark*) i kvalitativnom usporedbom s eksperimentalno dobivenom slikom putanje loma. Manji je broj modela kvantitativno validiran u usporedbi s eksperimentom, što je preduvjet kako bi modeli predikcije loma primjenom faznog polja uistinu mogli postati pouzdana alternativa numeričkih simulacija rasta pukotina u inženjerskoj praksi. Dio modela testiran je i na heterogenim mikrostrukturnim geometrijama. Neki od primjera su radovi na geometriji dobivenoj mikrotomografijom betona ili nodularnog lijeva u jednom od autorovih radova, proizvoljnoj (randomiziranoj) mikrostrukturi grafita H-451 ili uranovog dioksida (UO2) gdje su svojstva materijala kalibrirana prema simulacijama molekularne dinamike.

Tek je nedavno formulacija faznog polja proširena i na probleme zamornog loma. Predstavljeni modeli jasno pokazuju potencijal metode faznog polja za repliciranje glavnih značajki zamornog loma, uključujući nastanak pukotine, stabilne i nestabilne faze rasta, rezultat čega su poznata Wöhlerova krivulja i Parisov zakon. Navedeni modeli razvijeni su pod pretpostavkom

elastičnog ponašanja materijala što odgovara takozvanom visokocikličkom zamornom režimu. Budući da je zamorni lom jedan od glavnih uzroka loma inženjerskih konstrukcija, a njegovo numeričko predviđanje i dalje predstavlja veliki izazov, za očekivati je da će se uskoro pojaviti i još napredniji modeli zamora s temeljitom eksperimentalnom validacijom. Međutim, u ovom trenutku još uvijek nedostaje generalni model koji je sposoban replicirati lom pri monotonom opterećenju, kao i značajke nisko- i visokcikličkog zamora. Ovaj rad se također bavi i s razvojem takvog modela.

Određeni problemi u numeričkoj implementaciji modela unutar okvira metode konačnih elemenata i dalje postoje te su predmet intenzivnog istraživanja u znanstvenoj zajednici. Neki od glavnih problema su nekonveksnost temeljnog funkcionala slobodne energije s obzirom na stupnjeve slobode polja pomaka i faznog polja, način modeliranja ireverzibilnosti loma te dugo vrijeme računanja zbog često potrebnih, vrlo gustih mreža konačnih elemenata.

Konačno, većina implementacija modela loma metodom faznog polja razvijena je u nekomercijalnim softverima otvorenog koda baziranim na MKE ili kao samostalni algoritmi. Na taj je način značajno ograničen potencijal primjene ove metode u praktičnim inženjerskim problemima izvan znanstvene zajednice. S druge strane, primjena modela loma temeljenih na metodi faznog polja unutar najčešće korištenih komercijalnih računalnih MKE paketa ključna je za promicanje metodologije kod ostalih inženjera, istraživača i studenata. Zbog toga su modeli razvijeni u ovom radu implementirani u komercijalni računalni MKE paket ABAQUS te objavljeni i slobodno dostupni online.

HIPOTEZE, CILJEVI, ZNANSTVENI DOPRINOS I ZAKLJUČAK

Cilj ovog rada je razviti i implementirati novu unificiranu i robusnu metodu za numeričko modeliranje krhkih, duktilnih i zamornih procesa oštećenja i loma, ovisno o materijalnim svojstvima i vrsti opterećenja. Metoda bi trebala biti općenita te omogućiti modeliranje složenih procesa loma uključujući iniciranja oštećenja, propagaciju, grananje i srastanje pukotina bez uvođenja dodatnih specijalnih uvjeta. Takva metoda bi trebala omogućiti učinkovito rješavanje složenih procesa loma prisutnih na mikrostrukturnoj razini heterogenih materijala. Hipoteza ovog rada je mogućnost razvoja takve numeričke metode primjenom teorije faznog polja za modeliranje oštećenja i loma koja pokazuje prednosti u odnosu na postojeće postupke, kod kojih se pukotina modelira kao geometrijski diskontinuitet. Dobiveni rezultati trebali bi jasno prikazati utjecaj mikrostrukturne topologije te utjecaj veličine uzoraka

čime bi numeričke metode mogle pridonijeti boljoj procjeni strukturne pouzdanosti i sigurnosti te razvoju materijala s poboljšanim mehaničkim svojstvima.

U sklopu ovog rada razvijena je poopćena numerička metoda rješavanja krhkog, duktilnog te zamornog oštećenja i loma temeljena na teoriji faznog polja. Metoda je implementirana u komercijalni MKE softver ABAQUS. Razvijen je „staggered“ algoritam s novim kriterijem konvergencije, temeljenom na provjeri norme reziduala, čime se poboljšavaja stopa konvergencije. Implementacija navedenog algoritma prva je takva implementacija iterativnog algoritma teorije faznog polja za rješavanje loma u paket ABAQUS. Time je također riješen problem ne-konveksnosti osnovnog funkcionala slobodne energije, koji često dovodi do numeričkih nestabilnosti. Sam algoritam je temeljito testiran čime je potvrđeno da je robustan i učinkovitiji od uobičajenih algoritama loma primjenom teorije faznog polja. Glavne prednosti implementacije unutar komercijalnog softvera su učinkovite iskorištene, uključujući računalnu paralelizaciju i opciju brisanja elemenata kako bi se smanjilo vrijeme računanja; korištenje različitih rješavača koji omogućuju računanje primjera s opterećenjem zadanim putem pomaka, ali i sile; korištenje naprednih kriterija konvergencije; korištenje automatske inkrementacije, opcije ponovnog pokretanja, odnosno nastavka analiza; opcije računanja problema konktakta. Razmatrane su različite 1D, 2D i 3D formulacije elemenata. Kompletan izvorni kod zajedno s primjerima predstavljenim u ovom radu, uputama i objašnjenjima javno je dostupan drugim istraživačima, studentima i inženjerima, promovirajući metodologiju loma primjenom teorije faznog polja. Kod je otvoreno dostupan na: https://data.mendeley.com/datasets/p77tsyrbx2/4

Kroz veliki broj primjera dokazano je da razvijena poopćena metoda može točno reproducirati krhki/duktilni ili zamorni lom, u skladu s ponašanjem materijala i uvjetima opterećenja. U skladu s tim, prikazana je i detaljna rasprava o točnosti rezultata i trajanju analize. Metoda je temeljito validirana i verificirana na primjerima krhkog i duktilnog ponašanja materijala, pod pretpostavkom materijalne homogenosti, usporedbom s numeričkim i eksperimentalnim rezultatima iz dostupne literature. Posebna pozornost posvećena je verifikaciji modeliranja zamornog loma putem parametarske analize. Konačno, metoda je primijenjena na stvarnoj heterogenoj mikrostrukturi nodularnog lijeva dobivenoj metalografijom. Uzorci su monotono i ciklički opterećeni pri čemu je prikazano modeliranje krhkog, duktilnog i prijelaza između krhkog i duktilnog loma u monotonom opterećenju, te visoko- i niskocikličkog zamornog loma u cikličkom opterećenju.

U radu su prikazani sljedeći izvorni znanstveni doprinosi:

1. Razvoj novog poopćenog modela loma temeljenog na teoriji faznog polja

    - Dokazano je da model točno reproducira krhki/duktilni ili zamorni lom, u skladu s ponašanjem materijala i uvjetima opterećenja. Takva poopćena metoda također točno računa lom pri monotonom opterećenju bez utjecaja zamora. Dodatni parametri koji odgovaraju zamornim svojstvima materijala jasno su povezani s poznatim empirijskim parametrima.

    - Uključene su različite formulacije teorije faznog polja, s različitim opisom i utjecajem na početni linearno elastični strukturni odziv, i modeli plastičnosti za opisivanje duktilnog loma, uključujući kombinirani nelinearni izotropno-kinematički model očvršćenja. Ugrađena je tehnika preskakanja ciklusa za probleme cikličkog opterećenja.

    - Predloženi model je temeljito testiran, verificiran i validiran u usporedbi s numeričkim i eksperimentalnim rezultatima iz literature. Glavne značajke zamora, uključujući Wöhlerove i Parisove krivulje u nisko- i visokcikličkom režimu opterećenja, mogu se lako izračunati bez uvođenja dodatnih kriterija.

2. Razvoj „staggered“ iterativnog algoritma s kriterijom zaustavljanja koja se temelji na normi reziduala

    - Algoritam je dokazano robustan i učinkovitiji u usporedbi s uobičajeno korištenim algoritmom jednostruke iteracije. Točnost više ne ovisi o pažljivom odabiru veličine koraka računanja, dok je vrijeme računanja znatno smanjeno.

    - Naglašena je važnost kriterija konvergencije za „staggered“ algoritme modela loma pomoću teorije faznog polja.

3. Sustavno je ispitan potencijal predložene metode u modeliranju složenih procesa krhkog, duktilnog i zamornog loma analizom realne heterogene mikrostrukture nodularnog lijeva pri monotonom i cikličkom opterećenju

    - Uzorci različite veličine nasumično su odabrani iz metalografske slike nodularnog lijeva pritom zadovoljavajući globalni prosječni sadržaj grafitnih nodula. Ispitane su tri mogućnosti modeliranja nodula koje se razlikuju u razini modeliranih detalja, među kojima je i modeliranje nodula kao mikrostrukturnih uključina sa svojstvima grafita. Time je prikazana i mogućnost razvijene implementacije u rješavanju problema kontakta.

- Prikazan je utjecaj mikrostrukturne topologije, odnosno veličine, oblika i raspodjele mikrokonstituenata. Predloženi model može simulirati složene procese loma, uključujući nastajanje, lokalizaciju, rast, spajanje i grananje pukotina, koji se pojavljuju na mikrostrukturnoj razini.

- Provedena je parametarska analiza čime je prikazan utjecaj lomne žilavosti materijala na prijelaz između krkog i duktilnog ponašanja materijala i obrazaca loma, u okviru predložene metode. Primjeri s cikličkim opterećenjem pokazuju veliki potencijal predloženog modela za rješavanje zamornog loma u nisko- i visokocikličkom režimu opterećenja. Prikazan je jasni prijelaz između dva režima.

Ključne riječi: numerička analiza oštećenja i loma, metoda faznog polja, metoda konačnih elemenata, heterogena mikrostruktura, poopćeni model oštećenja i loma, rast pukotine, krhki lom, duktilni lom, visokociklički zamor, niskociklički zamor, ABAQUS.

TABLE OF CONTENTS

LIST OF FIGURES

LIST OF TABLES

NOMENCLATURE

CALLIGRAPHY LETTERS

$\mathcal{I}$	-	fourth order unit tensor
$\mathcal{H}(t)$	-	history field parameter

LATIN SYMBOLS

a	-	crack length
a_0	-	initial notched crack length
A1, A2, A3	-	amplitudes of the prescribed sinusoidal displacement
b	-	saturation rate of the yield surface
$\bar{\mathbf{b}}$	-	prescribed volume force vector
B	-	CT specimen thickness
B1, B2	-	prescribed sinusoidal displacement
$\mathbf{B}^{\mathrm{v}}, \mathbf{B}^{\phi}$	-	matrix of shape functions derivatives
C	-	initial kinematic hardening modulus, Paris law parameter
C_1, C_2, C_3, C_4	-	parameters of general power law isotropic hardening function
$\mathbf{C}$	-	material matrix
$\mathbf{C}^{\mathrm{e}}$	-	elastic tangent matrix
$\left(\mathbf{C}^{\mathrm{e}}\right)^{\pm}$	-	positive and negative part of the elastic tangent matrix
$\mathbf{C}^{\mathrm{ep}}$	-	elastoplastic tangent matrix
$\mathrm{d}\Omega$	-	surface of n-dimensional body
$\mathrm{d}a/\mathrm{d}N$	-	crack length growth rate
$\tilde{D}$	-	crack driving state function
E	-	Young's modulus
$f\left(a/W\right)$	-	geometric function for stress intensity factor calculation

F	-	force, pressure-independent yield function
$F_{\min}$	-	minimal loaded force
$F_{\max}$	-	maximal loaded force
ΔF	-	loading force range
$\hat{F}$	-	fatigue degradation function
$\mathbf{F}_{\text{ext}}^{\mathbf{v}}, \mathbf{F}_{\text{ext}}^{\phi}, \mathbf{F}_{\text{int}}^{\mathbf{v}}, \mathbf{F}_{\text{int}}^{\phi}$	-	internal and external force vectors
$g(\phi)$	-	degradation function
G_{c}	-	fracture toughness
$h_{\text{iso}}, h_{\text{kin}}$	-	isotropic and kinematic hardening modulus
H	-	Heaviside function
$I_{\text{L}}, I_{\text{G}}$	-	user set number of iterations for automatic incrementation
$\mathbf{I}$	-	second-order unit tensor
J	-	J-integral
$\mathbf{K}, \mathbf{K}^{\mathbf{vv}}, \mathbf{K}^{\phi}$	-	stiffness matrices
K	-	stress intensity factor
ΔK	-	change in stress intensity factor
l	-	length scale parameter
L	-	length of the microstructural specimen
m	-	Paris law parameter
$\mathbf{n}$	-	unit outward-pointing normal vector
N	-	cycle number
N	-	shape function
N1, N2, N3	-	nodule modelling options
$\mathbf{N}^{\mathbf{v}}$	-	shape function matrix
P_1, P_2, P_3	-	consecutive cycle data point for cycle jumping technique
q_{y}	-	user-input allowed relative error for cycle jumping technique

Q_∞	-	user-input allowed relative error for cycle jumping technique
R	-	load ratio
$\mathbf{R}, \mathbf{R}^{\mathbf{v}}, \mathbf{R}^{\phi}, \mathbf{R}^{\text{total}}$	-	residual vectors
s_{12}, s_{23}	-	discrete slopes of the function $\mathbf{y}(t)$ in cycle jumping technique
S, M, L	-	microstructural sample sizes
t	-	time
Δt_{cycle}	-	time length of a cycle in cycle jumping technique
Δt_{jump}	-	number of cycles to skip in cycle jumping technique
$\bar{\mathbf{t}}$	-	prescribed surface traction vector
$\mathbf{u}, \bar{u}$	-	displacement vector
$\delta\mathbf{u}$	-	variation of the displacement vector
u	-	displacement in x direction
Δu	-	displacement-control loading increment size
v	-	displacement in y direction
$\mathbf{v}$	-	vector of nodal degrees of freedom
$\delta\mathbf{v}$	-	variation of nodal degrees of freedom vector
W	-	CT specimen hight
W^{ext}	-	external energy potential
δW^{ext}	-	variation of the external energy potential
W^{int}	-	internal energy potential
δW^{int}	-	variation of the internal energy potential
x	-	coordinate in Carthusian system
y	-	coordinate in Carthusian system
$\mathbf{y}$	-	set of variables for cycle jumping technique
z	-	coordinate in Carthusian system

GREEK SYMBOLS

α	-	loading angle in Single edge notched specimen

$\boldsymbol{\alpha}$ - backstress tensor

β - coefficient used in calculation of elastoplastic tangent matrix

$\boldsymbol{\varepsilon}$ - strain tensor

$\boldsymbol{\varepsilon}^{\mathrm{e}}$ - elastic strain tensor

$\boldsymbol{\varepsilon}_{\mathrm{dev}}$ - deviatoric part of the strain tensor

$\boldsymbol{\varepsilon}^{\mathrm{p}}$ - plastic strain tensor

$\varepsilon_{\mathrm{eqv}}^{\mathrm{p}}$ - equivalent plastic deformation

ε_M - mean strain

$\boldsymbol{\varepsilon}^{\pm}$ - positive and negative parts of the strain tensor

$\boldsymbol{\varepsilon}^{\pm}$ - positive and negative parts of the strain tensor

$\delta\boldsymbol{\varepsilon}$ - variation of the strain tensor

ϕ - phase-field parameter

$\delta\phi$ - variation of the phase-field parameter

$\delta_{\mathrm{B}}, \delta_{\mathrm{D}}$ - coefficients of increment increase/decrease in automatic incrementation

$\boldsymbol{\phi}$ - vector of phase-field degrees of freedom

γ - crack density function, rate of kinematic modulus decrease, shear strain

$\hat{\gamma}$ - plastic multiplier

Γ - crack surface

$\boldsymbol{\eta}, \boldsymbol{\eta}^{\mathrm{trial}}$ - relative (trial, predictor) stress vector

λ - Lamé constant

μ - Lamé constant

ν - Poisson's ratio

$\theta_1, \theta_2, \theta_3$ - coefficients used in calculation of elastoplastic tangent matrix

$\boldsymbol{\sigma}$ - Cauchy stress tensor

$\boldsymbol{\sigma}_{\mathrm{dev}}, \boldsymbol{\sigma}_{\mathrm{dev}}^{\mathrm{trial}}$ - deviatoric part of the predictor trial stress tensor

$\boldsymbol{\sigma}^{\mathrm{trial}}$ - predictor stress tensor in return-mapping algorithm

$\left(\boldsymbol{\sigma}^{\text{trial}}\right)^{\pm}$ - positive and negative part of the predictor stress tensor

$\boldsymbol{\sigma}^{*}$ - effective (non-degraded) stress tensor

$\sigma^{\max}$ - maximal stress

σ_{y} - yield surface

σ_{y}^{0} - initial value of the yield surface

τ - time-like scalar variable

ξ - fine-tuning fatigue parameter

ψ - strain energy density

ψ_{c} - critical fracture energy density

ψ_{e} - elastic strain energy density

$\psi_{\text{e}}^{\pm}$ - positive and negative part of the elastic strain energy density

ψ_{p} - plastic energy density

$\bar{\psi}$ - local energy density accumulation variable

$\bar{\psi}_{N}$ - local energy density accumulation variable at increment N

$\bar{\psi}_{\infty}$ - fatigue parameter

Ψ - internal energy functional

$\delta\Psi$ - variation of the internal energy potential

Ψ^{b} - bulk energy

Ψ^{s} - fracture induced dissipated energy

Ω - volume of n-dimensional body

ζ - non-dimensional parameter controlling the post-critical behaviour after the crack initialization

Chapter 1

Introduction

Summary

1.1. Motivation

Some of the main characteristics of modern structures and machine components are their ever-increasing design complexity and use of new materials with enhanced properties to meet rising safety, reliability and durability requirements while simultaneously satisfying high efficiency and low-cost demands in manufacturing, maintenance and optimal control. Moreover, increasing component lifetime is an important factor in dealing with pressing issues of climate changes and environment preservation. One of the central issues, often directly causing a loss of products, services or in more extreme cases, life, is material failure. Its prediction and prevention are thus undoubtedly still a major concern, and as such, an area of great interest to many engineers and researchers.

In modern engineering, numerical simulations are an inevitable part of component design and material development. Following appropriate validation procedure, numerical simulations are complementing and gradually replacing often expensive and time-consuming experiments,

reducing the number of needed prototypes and improving predictive maintenance, thus directly tackling the aforementioned industrial and environmental demands.

The materials used in modern structures and machine components often exhibit significant microstructural heterogeneity. Various geomaterials such as concrete and rocks, high-strength steels, composites and polymers, or materials produced by emerging procedures like sintering or additive manufacturing, are just some examples of such materials. Their properties are affected to a great extent by the individual microconstituent properties and microstructural topology, i.e., size, shape and distribution of the microconstituents. Furthermore, most of the complex fracture processes (e.g., crack initiation, localization, propagation, merging and branching) occur at the microstructural scale, making the fracture analysis of heterogeneous microstructure an especially challenging and interesting problem.

Therefore, numerical fracture analysis of heterogeneous materials which considers their microstructural properties and topology could be a valuable asset for the assessment of structural integrity, reliability, and component lifetime in modern structures and machine components. It could lead to a more realistic material behaviour description, which could, in turn, assist the development of materials with enhanced properties coming from the desired microstructure, and enable the production of more efficient, safer and cheaper structures built from heterogeneous materials.

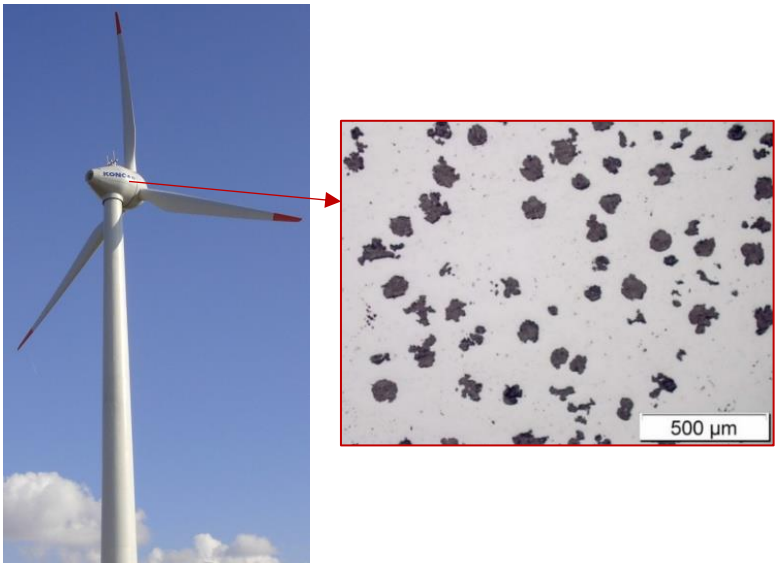

Fig. 1.1. Example of microheterogeneous materials used in modern-day engineering (Končar KO VA 57/1 wind turbine with nodular cast iron hub)

1.2. State of the art

1.2.1. Historical development of fracture mechanics

A significant progress has been achieved in understanding the fundamental physics and mechanics of fracture since the early works of Griffith [1] in the 1920s. The Griffith's theory provided a quantitative connection between the fracture stress and flaw size in ideally brittle materials, and thus introduced the branch of fracture mechanics into the field of classical mechanics. It stated that a fracture occurs, i.e., a material flaw becomes unstable, when the change of strain energy resulting from the incremental crack growth is larger than the surface energy of the material. Later development of the theory by Irwin [2, 3], who introduced the energy release rate concept, provided its application to the range of ductile materials making it more useful for solving engineering problems of the time. Essential difference between the class of brittle and ductile materials is the ability of ductile materials to undergo significant plastic deformation before fracture. This is schematically displayed in Fig. 1.2. together with some real-life examples. In 1961 Paris and his co-workers [4] applied fracture mechanics principles to the fatigue crack growth. Fatigue refers to the process of material weakening due to repeated applied loads individually too low to cause monotonic fracture. Rapid advancements in the computer technology and the simultaneous progress of numerical modelling in the past century significantly raised the practical relevance of fracture mechanics. Computational fracture mechanics thus became an indispensable tool in fracture analysis with early fracture mechanics theories providing its criteria for crack propagation.

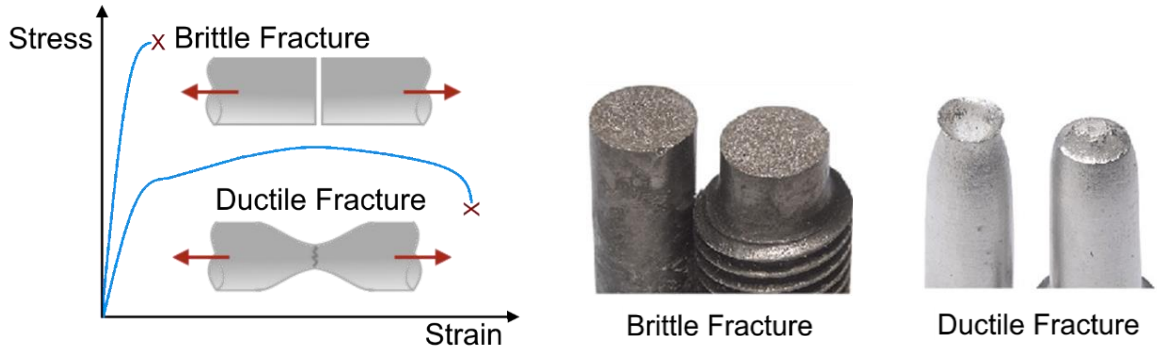

a) b) c)

Fig. 1.2. Brittle vs Ductile fracture. a) Schematic representation of stress-strain, b) Brittle fracture in a mild steel [5] and c) Ductile fracture in aluminium [5]

1.2.2. Numerical damage and fracture models

The numerical damage and fracture modelling methods are most commonly included within the Finite Element Method (FEM) framework. It is based on the concept of dividing the

physical model into smaller segments (elements) with simple geometry and a finite number of degrees of freedom. Such a discrete model of an object consisting of the finite element mesh can then be described by a boundary value problem resulting in a system of algebraic equations and easily solved.

These numerical damage and fracture modelling methods can be generally divided into discrete and diffusive, or continuum, formulation approaches based on their description of fracture.

1.2.2.1. Discrete crack modelling approaches

Discrete crack modelling approaches introduce the crack as a sharp geometrical discontinuity. One of the most used techniques to handle discrete crack propagation is the cohesive zone modelling (CZM) first introduced in Barenblatt [6] and Dugdale [7] to address the stress singularity and nonlinear processes in front of a pre-existent crack. It is implemented through interface or generalized contact elements which compose a narrow-band called cohesive zone ahead of the crack front [8, 9]. At this zone the material follows a nonlinear constitutive law relating the cohesive traction to the separation displacement of the cohesive surfaces. Traction first increases until the maximum value is reached, and subsequently reduces to zero resulting in a complete separation. Despite physical separation of the surfaces, CZM maintains continuity conditions and eliminates stress singularity at the crack tip limiting it to the cohesive strength of the material. However, since the crack propagates along the element edges, the standard CZM finite element implementation exhibits a strong dependence of the results on the mesh size and orientation during crack growth, as presented in Chandra et al. [10]. A comprehensive literature review of the CZMs, including their advantages and limitations has been done in Elices et al. [11]. On the other hand, to properly model arbitrary crack topologies, remeshing algorithms presented in [12, 13] and enriched FEM discretization techniques, most notably the extended finite element method (XFEM) [14, 15], were developed. In XFEM, the displacement field is enriched with the Heaviside functions to model the crack surface displacement discontinuity, and the asymptotic near-tip singularity functions to capture the stress singularity at the crack tip. This enables the prediction of crack growth independent of the finite element discretization. XFEM shows great success in resolving the crack tip stress singularities and true stress behaviour at the vicinity of the crack tip, as presented in Moës et al. [16]. Along with the additional criteria for crack initiation, propagation and growth direction required in the discrete crack modelling methods, a major problem arises with the numerical

tracking of the crack discontinuities, which can lead to significant implementation difficulties in three-dimensional (3D) settings.

In recent years, a number of meshless methods have been developed enabling the crack evolution without remeshing. The element-free Galerkin (EFG) method as a representative, proposed by Belytschko et al. [17, 18], has been used extensively to model linear and nonlinear crack propagation problems. However, these methods suffer from the following key problems when compared with FEM: the numerical integration of a weak form, the enforcement of essential boundary conditions, numerical instability and computational expense as reported in Babuška et al. [19], and Qian and Zhou [20].

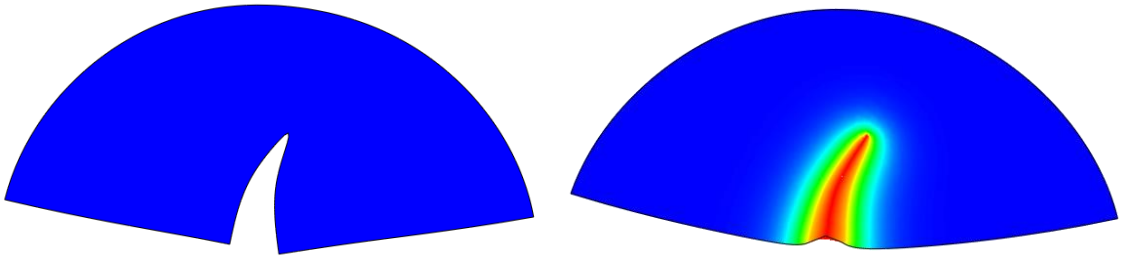

Fig. 1.3. Discrete versus diffusive crack modelling

1.2.2.2. Diffusive crack modelling approaches

Diffusive crack modelling approaches, often called continuum damage or smeared crack modelling approaches, introduce a damage parameter at the material point level instead of modelling an actual crack topology. Damage parameter then controls the stiffness of the material, incorporating the stress release associated with the crack formation into the constitutive model (see de Borst [21] for a detailed overview). A number of continuum damage models are based on the assumption of standard continuum (also called the local continuum). The material behaviour is then characterized by the constitutive law at each material point, which does not exhibit the influence of the surrounding points. The increase of the damage parameter value in these models leads to a strong softening behaviour followed by an intense strain and damage localization, as reported in Aifantis [22]. Consequently, it causes a local loss of ellipticity of the governing differential equations, which in turn leads to numerical solutions converging to physically meaningless solutions, as discussed in de Borst et al. [23]. In the FEM discretization framework, the problem is manifested through the non-objective results caused by the strong mesh refinement and alignment dependence, reported in Bazant and Belytschko [24]. To alleviate this problem, the non-local [25], and gradient-enhanced continuum

approaches [26] have been developed. They introduce a non-local state variables which usually depend on their local counterpart through the use of length scale parameters. These models are also able to predict size effects, previously not possible with the local continuum models. Similar approaches based on the introduction of the length scale parameters also include the crack band model [27], micropolar [28] and later micromorphic theory [29]. Particular drawback of the non-local approaches presented in [25, 26] is the widening of the damage zone normal to the crack propagation direction, reported in Simone et al. [30]. This problem is commonly avoided by the introduction of length scale parameter as a function of strain level in Geers et al. [31], and Pijaudier-Cabot et al. [32]. However, the underlying assumption of this models might not have a microstructurally correct physical background as explained in Poh and Sun [33]. The damage zone expansion problem has also been alleviated by the introduction of a nonlocal continuum theory in Putar et al. [34].

1.2.3. Numerical modelling of heterogeneous materials

Advancements in the computer technology also gave rise to the numerical methods combining the field of mechanics of materials with the field of material science. While the assumption of the material macrohomogeneity is often still valid in engineering practice, the development of advanced materials, used in modern day complex structures, requires the consideration of material microheterogeneity and its influence on the macroscale constitutive response. Experimental techniques have also gone a long way in assessing the microstructural heterogeneity and aiding the numerical simulations. The best example is the X-ray microtomography [35], which is now able to routinely generate realistic geometrical models of microstructure for many materials at various scales by using 3D imaging techniques [36-39]. One way of dealing with microheterogeneity is the use of direct numerical simulation (DNS), where detailed heterogeneities are modelled directly at the macroscale. Although computationally very intensive, especially when dealing with large scale transitions consequently requiring very fine meshes, it is obviously the most accurate method to calculate heterogeneous materials failure. On the other hand, in order to cut the computational costs, multiscale methods are developed separating the scales by transporting the solutions between the scales in an appropriate way. A detailed overview of multiscale methods, their development and application, is presented in [40-42]. The most popular method within the class of multi-scale methods is the computational homogenization (CH) method. It is based on the averaging of certain mechanical properties over a representative volume element (RVE), assumed to be

a statistical representative of the macroscopic material point, as first explained by Hill [43]. The first-order homogenization has become a standard tool in CH [44-46], with most applications conducted in elastic or elasto-plastic hardening regimes. Moreover, it has been extended to the thermomechanically coupled computational homogenization in Ozdemir et al. [47, 48], and the second-order computational homogenization schemes considering the higher order deformation gradients at the macroscale in Kaczmarczyk et al. [49], and Lesičar et al. [50, 51]. However, when it comes to modelling the material failure, which is essentially a multiscale phenomenon as macroscopic cracks are a direct result of the cascade of events happening at the microstructural level [52, 53], there are still major problems with computational homogenization methods, as reported in Budarapu et al. [54]. Some works report the use of the continuous–continuous second-order scheme [55, 56], where continuum damage models are used on both scales. However, it only enables the resolution of moderate localization bands (the macroscopic strain field varies only linearly over the microscale RVE), but is inadequate when dealing with sharper localization regions, e.g., ductile damage coalescence on RVE [40]. The use of discontinuous-continuous scale-transition approaches [57-59], where a discrete crack modelling approach is introduced at the macroscale, seems to alleviate the sharp localization problem. However, it comes with the additional computational complexity and issues not arising in the conventional computational homogenization. An important issue in the CH multiscale treatment of the material failure arises with the questionable existence of the RVE, where, by its definition, it loses its statistical representativeness upon the onset of localization. Alternative homogenization schemes indicate the possibility of resolving this issue for quasi-brittle materials [59-61].

As presented, the multiscale methods have been proven successful in general when no material softening is expected, and while they give promise to multiscale modelling of material fracture, there still seems to be a long way before they can be consistently and reliably applied in actual structural problems. On the other hand, as fracture processes at the microstructural level of highly heterogeneous materials often consists of complex crack processes, the development of a generalized numerical method capable of reliably describing these processes including the fracture nucleation and propagation, without *ad hoc* criteria, is still an area of major interest. Development of the damage and fracture models for the highly heterogeneous materials, while considering actual microstructural topologies, offers a way to more accurately predict the fracture processes in related materials and will be dealt with in this thesis.

1.2.4. Phase-field fracture models

The phase-field modelling approach has been gaining tremendous popularity over the past decade. The phase-field framework is commonly related with modelling the systems consisting of different phases divided by sharp interfaces. It incorporates an order parameter – a continuous variable differentiating between the physical phases within a given system through a smooth transition. In case of fracture modelling, broken and unbroken material states are separated. The sharp crack discontinuity is thus approximated by a diffusive band whose width is regulated by a length-scale parameter. Therefore, phase-field fracture method can be classified as a diffusive crack modelling method. Interestingly, the phase-field fracture framework has been independently developed by physics and mechanics community with considerably different approaches and starting points to derive the phase-field evolution equations. The physics community developed dynamic fracture models [62, 63] using the Ginzburg-Landau theory [64] originally derived for electromagnetic second-order phase transition phenomena. On the other hand, the phase-field fracture models which this thesis is focused on, originate from the variational approach to brittle fracture proposed by Francfort and Marigo [65]. It was proposed as an extension of the Griffith's energy-based fracture theory and recast as the energy minimization problem. The energy functional is then akin to the potential used in image segmentation presented by Mumford and Shah [66]. It has later been regularized by Bourdin et al. [67, 68], based on the Γ-convergence theory by Ambrosio and Tortorelli [69], reformulating it as a system of partial differential equations that completely determine the crack evolution, thus enabling an efficient numerical implementation. The regularized models closely resemble gradient-damage models with the clear differences in the choice of the free energy and dissipation function, as discussed by de Borst and Verhoosel [70].

One reason of the popularity of the phase-field approach to fracture is its success in solving complex fracture processes (e.g. crack nucleation in absence of stress singularity, crack propagation, merging, kinking or branching), without introducing any *ad hoc* criteria. Moreover, its smooth approximation of the crack topology on a fixed finite element mesh circumvents the complex crack-surface tracking problem. This, in turn, significantly simplifies the finite element implementation, especially in 3D settings.

A considerable number of various phase-field brittle fracture formulations has been recently developed for the quasi-static [71-75] and dynamic [76-78] models. A great overview of the phase-field brittle fracture models is done by Ambati et al. [79]. Furthermore, the framework

has been extended to handle the ductile fracture in [80-86] by different formulations with various advantages and disadvantages, well summarized by Alessi et al. [87]. Moreover, it has been extended to multiphysics problems related to thermomechanical fracture in [88-90], hydraulic fracture [91, 92], electromechanical fracture [93], fracture in porous media [94-97] or soil-like materials [98], and many more, showing the great potential of this method. A summary of phase field state-of-the-art approaches to fracture has been compiled in the special issue [99] and more recently in a book chapter by de Lorenzis and Gerasimov [100].

A majority of the listed phase-field formulations have been thoroughly verified by available numerical benchmark tests, and qualitative experimental data comparing the predicted and observed crack paths. In contrast, phase-field brittle fracture formulations have been quantitatively validated on a plaster material by Nguyen et al. [101], and the Polymethylmethacrylate (PMMA) material by Pham et al. [102], while Zhou et al. [103] used quantitative experimental data on rock fracture testing available in literature. Moreover, quantitative experimental validation has been done on anisotropic brittle materials by Bleyer and Alessi [104], where fibre-reinforced composites have been used, while the ductile fracture formulation has been validated by Ambati et al. [105]. A proper validation of phase-field algorithms remains an open issue and is needed for phase-field fracture approaches to become a truly reliable tool for the crack propagation simulation in real-life structural components.

The phase-field method has been applied to the analysis of brittle fracture in heterogeneous microstructural geometries obtained from the X-ray microtomography of concrete by Nguyen et al. [106]. Similarly, a phase-field fracture model has been used on the simplified heterogeneous microstructural geometry obtained by microtomography of nodular cast iron in the author's works [107, 108]. Phase-field brittle fracture models have also been used on the randomized microstructure of nuclear grade graphite H-451 in [109], and uranium dioxide (UO_2) in [110], where material properties were calibrated from the molecular dynamics based fracture simulations. A microscale phase-field model for fracture in poro-elasto-plastic media has been proposed by Aldakheel [111] to model concrete failure on micro-CT scanned geometry. On the other hand, Patil et al. [112] included uniform heterogeneities in standard numerical benchmark examples. Therefore, phase-field fracture models proved highly appropriate for modelling complex fracture processes in heterogeneous microstructures.

The phase-field fracture framework has been very recently extended to the fatigue crack propagation problems, too. Unlike the fatigue models using empirical data or parameters with

no clear physical interpretation [113-115], the extended phase-field fracture method is able to reproduce the main features of fatigue failure with fracture-based input parameters. Boldrini et al. [116] presented a phase-field model coupling the fracture behaviour with thermal and fatigue problem, where fatigue behaviour is introduced via additional scalar parameter. On the other hand, Caputo and Fabrizio [117] as well as Amendola et al. [118] adopted the phase-field fracture model with Ginzburg-Landau formalism, where the material degradation under cyclic loading is introduced by incorporating a fatigue potential. On the other hand, a more intuitive approach has been very recently proposed by Alessi et al. [119], Carrara et al. [120] and Seiler et al. [121], where not only the stiffness is being degraded due to phase-field evolution, but also the fracture energy on the account of strain or stress history. The presented models clearly show the potential of the phase-field method to reproduce the main features of fatigue failure including the crack nucleation, stable and unstable propagation phases, while recovering Paris law and the Wöhler curve naturally. The models are developed under the assumption of elastic material behaviour, which corresponds to the so-called high-cycle fatigue regime. Since the fatigue failure is one of the critical causes of engineering structures failure with its numerical prediction still representing a great challenge, it is expected that even more advanced phase-field fatigue models with thorough experimental validation will emerge soon. However, at this time a general framework able to reproduce the monotonic fracture as well as the features of low- and high-cycle fatigue is still missing. This thesis deals with such a framework.

Certain challenges in the computational treatment of the phase-field fracture method within the finite element framework still exist and have recently become a subject of intensive research, providing some great insights and innovative solutions. Namely, the non-convexity of the underlying free energy functional with respect to the phase-field and displacement field; the irreversibility of the crack phase-field parameter; and the size of the length scale regularization parameter often requiring extremely fine meshes in the crack propagation zone.

The non-convexity of the underlying free energy functional constitutes a major problem within the so-called *monolithic* treatment of the variational formulation. Such monolithic algorithms attempt to solve this coupled system by computing the unknowns, i.e., displacement and crack phase-field, simultaneously. However, due to the lack of convexity, local minima exist (schematically shown in Fig. 1.4) thus creating obvious convergence issues. As a result, pure monolithic algorithms are unstable in the so-called brutal crack evolution as well as in the post-peak loading regime. Only a few works have been published utilizing the fully monolithic

treatment of the phase-field fracture problem. Nevertheless, some improvements to the robustness of the monolithic approach have been studied recently. To this end, a dissipation-based arc-length procedure for the monolithically solved system has been presented by Verhoosel et al. [122], a modified line-search assisted monolithic solver has been proposed by Gerasimov and de Lorenzis [123], a modified Newton scheme with Jacobian modification has been used by Wick [124]. Furthermore, Heister et al. [125] proposed the linearization of the elastic part of total energy by replacing the unknown phase-field parameter with its known and fixed extrapolated value in order to obtain a convex energy functional. A slightly different approach to tackle the non-convexity issue has been presented by Kopanicakova and Krause [126] where a recursive multilevel trust region method is used.

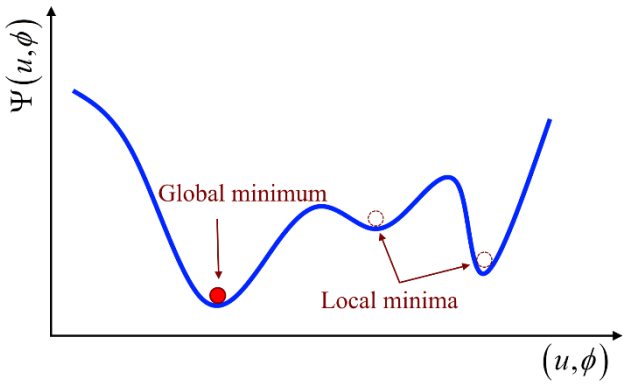

Fig. 1.4. Schematic representation of non-convex free energy functional

On the other hand, a very common remedy to the non-convexity problem is the use of staggered (also called alternate minimization) solution strategy. It is based on the observation that, while the free energy functional is generally non-convex, it is convex with the respect either to the displacement or the phase-field variable if the other one is held constant [67]. Thus, utilizing the operator split principle, the weak formulation is decoupled yielding a two-equation system to be solved in an iterative manner. Due to its proved robustness, this solution procedure is very popular. The staggered solution scheme proposed in Miehe et al. [72] is based on a single staggered iteration procedure. Because of its implementation simplicity and proved robustness, it is widely used [77, 127-129]. However, it requires small loading increments in order to provide an accurate solution, making it computationally rather expensive for more complex problems. In contrast, utilizing more iterations per increment allows the use of larger loading increments, while the efficiency and convergence rate depends on the stopping criterion. Duda et al. [130] and Bourdin et al. [68] have used the criteria of running the iterative scheme until the successive solution variables were close enough to one another. In Ambati et al. [79], the

issue of convergence rate has been tackled through a stopping criterion based on a normalized change of the system's energy. On the other hand, the slow iterative convergence rate typical of the staggered solution strategy was overcome by employing the over-relaxed alternate minimization with Newton-type methods in Farrell and Maurini [131]. Part of this thesis's contribution is the development of the staggered solution scheme with a stopping criterion based on the control of the residual norm presented in author's work [132, 133] and emphasizing the importance of using a stopping criterion within a staggered scheme through the illustrative examples [107, 132].

The enforcement of fracture process irreversibility, i.e. the prevention of crack healing, in phase-field fracture models is achieved through the introduction of the irreversibility constraint on the crack phase-field parameter. This makes the formulation a constrained minimization problem. A direct way of introducing the irreversibility is by enforcing the monotonicity of the phase-field parameter through the variational inequality conditions [134-136]. However, it comes with an additional computational cost. Another way is the enforcement of much simpler and computationally cheaper variational equality conditions which have been classified as relaxed, penalized and implicit in Gerasimov and De Lorenzis [137], where a great overview of the irreversibility problem in phase-field fracture models is given as well. What is termed relaxed variational equality is actually enforcing the irreversibility only on the fully developed crack, while allowing the transition zone to heal [67, 68, 123]. Penalized approaches, as the word itself says, incorporate the irreversibility through the use of penalty functions [91, 124, 125, 137]. On the other hand, an implicit enforcement of the constraint was proposed by Miehe et al. [72] by introducing the strain-history field. This approach is particularly attractive due to its efficiency as its only computational cost is a floating-point comparison. It has been used in the majority of works on the topic of phase-field fracture as well as in this thesis. However, it violates the full variational nature of the approach.

The fine meshes needed to resolve small regularization length scale sizes within the finite element framework are one of the aspects of the high computational cost of the phase-field fracture models. While it is fairly easy to model the fracture process whose final pattern is known in advance by using the appropriately pre-refined meshes, using fixed uniform meshes would generally lead to too high computational costs. To that end, mesh adaptivity through the error-controlled refinement strategies is presented in [112, 124, 138], while the physically-motivated procedures for mesh adaptivity were proposed in [125, 139-141]. Moreover, a

computational parallelization is another remedy to the computational cost of phase-field fracture models, presented in Liu et al. [128] and Mesgarnejad et al. [135]. The problem of computational parallelization is tackled in this thesis as well. From the point of view of computational cost, it can be seen that there is still a lot of room for improvement in the phase-field fracture models.

Finally, most of the listed phase-field fracture implementations are developed within the open-source Finite element (FE) programs or as the standalone algorithms. Only a few authors openly shared the source codes, thus considerably limiting the potential applications outside of the phase-field fracture community and its use in practical problems. To the best of author's knowledge, the shared source codes for the phase-field fracture models are made available by Bourdin[1] related to [68], Farrel[2] related to [131] and Heister[3] related to [125], in FE programs mef90 [142], FEniCS [143] and deal.II [144], respectively. On the other hand, the implementation of the phase-field fracture models within the more commonly used commercial FE software packages seems vital in promoting the methodology with engineers, researchers and students. The first such implementation into the commercial finite element software ABAQUS [145] was done by Msekh et al. [146] by utilizing a user finite element with an additional nodal degree of freedom (DOF) describing the phase-field variable and solving the system in a monolithic manner. The monolithic strategy has also been used in Pillai et al. [147], however the source codes were not provided. The staggered algorithm has been implemented in Molnar and Gravouil [127] by separating the displacement and phase-field DOFs into two user element types arranged in a layered manner with the addition of third layer used for the visualization. Similarly, the staggered algorithm has also been implemented in [128, 148], but unfortunately, the source codes were not provided. Mentioned staggered algorithm implementations [127, 128, 148] are based on the single iteration solution scheme [72]. The first commercial software implementation of the iterative phase-field staggered scheme with a stopping criterion was proposed in author's work [132], where a three-layered system has been introduced into the ABAQUS software, exhibiting computational efficiency and accuracy with no influence on the selection of loading increment size. Recently, a phase-field ductile fracture model has been implemented in the ABAQUS software in Fang et al. [149] using an iterative staggered solution scheme. Furthermore, an iterative staggered strategy has been used in Zhang

[1] https://github.com/bourdin/mef90
[2] https://bitbucket.org/pefarrell/varfrac-solvers/src/master/
[3] https://github.com/tjhei/cracks

et al. [150], where a phase-field model for cohesive fracture was implemented into ABAQUS. Lastly, Wu et al. [151] proposed the use of the Broyden-Fletcher-Goldfarb-Shanno (BFGS) method within the monolithic ABAQUS implementation providing robustness and better efficiency in comparison with staggered implementations. A comprehensive overview and comparisons of ABAQUS implementations has been recently done in Wu and Huang [152]. The phase-field models proposed and developed in this thesis are made freely available at Mendeley repository [133].

1.3. Research hypothesis and objectives/present contribution

The objective of this study is to develop and implement a novel unified and robust method for modelling of brittle, ductile, and fatigue damage and fracture processes, depending on material behaviour and loading type. The method should be general to allow the modelling of complex fracture processes including damage initiation, crack propagation, branching, and merging without the introduction of *ad hoc* criteria. The framework should be capable of efficiently solving complex fracture processes occurring at the microstructural level of heterogeneous materials. The hypothesis is the possibility of development of such method by applying the phase-field fracture methodology, which shows advantages over existing discrete damage and crack modelling procedures. The obtained results will show the effects of the microstructural randomness and exhibit size-effect, which will contribute to the assessment of structural reliability and safety and the development of advanced materials.

To that end, a generalized phase-field method for brittle, ductile and fatigue fracture is developed. The method is implemented into commercial FE software ABAQUS. A staggered algorithm has been developed with a new stopping criterion based on the residual norm control. It also solves the problem of non-convexity of the phase-field free energy functional. The implementation of the algorithm is the first such implementation of an iterative phase-field fracture solution scheme in the ABAQUS software. Thorough testing is conducted to assess the accuracy and stability of the implementation. The main advantages of implementation within commercial software are effectively utilized, including the thread parallelization and the element deletion option to reduce the common problem of high computational cost; the use of different solvers pre-programmed in ABAQUS (Newton-Raphson or Riks) allows the calculation of both displacement- and force-controlled loading cases; the advanced convergence criteria; automatic incrementation, restart and continuation of analyses; contact

problem options. Different 1D, 2D and 3D element formulations are considered. The complete source code along with the examples presented in this work, guides, and explanations is publicly available to other researchers, students, and engineers, promoting fracture methodology by applying phase field theory. The code is openly available at: https://data.mendeley.com/datasets/p77tsyrbx2/4

The capability of the proposed method to reproduce the brittle/ductile or fatigue fracture, according to the material behaviour and loading conditions is presented. Detailed discussions on the accuracy of the results and the computational costs are given throughout the work. The method is thoroughly validated and verified on the examples of brittle and ductile material behaviour, assuming the material homogeneity, in comparison with the numerical and experimental results from the available literature. Special attention is given to the verification of the modelling of fatigue fracture by conducting the parametric analysis. Finally, the proposed method is applied to the real heterogeneous microstructural geometries of nodular cast iron obtained by metallography procedure. The brittle and ductile failure behaviour is observed in monotonically loaded specimens while high- and low-cyclic fatigue fracture features are clearly recovered in cyclically loaded specimens.

The work behind this thesis makes the following contributions to the field of computational fracture mechanics:

1. **The phase-field fracture staggered algorithm with stopping criterion based on the control of the residual norm is developed**. The algorithm is thoroughly tested in comparison with commonly used single iteration staggered phase-field fracture algorithm. Detailed discussion on the accuracy of results and analysis duration is given. Furthermore, emphasis is put on the importance of using a stopping criterion within a staggered scheme by illustrative examples.

2. **The developed algorithm framework is extended to simultaneously tackle brittle, ductile and full range low- and high-cyclic fatigue fracture**, depending on the material properties and loading scenario. A novel description of energy accumulation variable is introduced allowing the accurate monotonic fracture analysis without the influence of the fatigue extension. Different phase-field formulations affecting the (linear-) elastic material behaviour stage are included together with a few different plasticity material models to account for the ductile fracture behaviour, as well as cyclic

plasticity in low-cyclic fatigue regime. The developed models are verified and validated in comparison with numerical and experimental data from available literature. Special attention is given to the verification of such a model through parametric study, obtaining well-known features of low- and high-cyclic fatigue such as the Paris law and the Wöhler curve. The cycle skipping technique is implemented to allow the calculation of very high number of cycles on moderate size examples.

3. **The potential of the proposed model in modelling of the complex brittle, ductile and fatigue fracture processes is thoroughly examined on real heterogeneous microstructural geometries of nodular cast iron obtained by metallography procedure**. The different specimen sizes are tested clearly observing the size-effect behaviour corresponding to the verified results reported in the literature. The capability of the phase-field framework in capturing the influence of microstructural topology, i.e., size, shape and arrangement of microconstituents, on the crack initiation and complex crack propagation patterns, is clearly observed in both monotonic and cyclic testing.

1.4. Thesis outline

The thesis is organized as follows. After the introductory discussion on motivation, state-of-the-art and thesis objectives, the general concepts of phase-field fracture model are provided in Chapter 2. The basic relations of phase-field brittle, ductile and fatigue fracture modelling are explained together with different phase-field formulations used in this thesis. Chapter 3 deals with the numerical implementation of the phase-field fracture model into FE software ABAQUS, where monolithic, single iteration staggered, and the proposed stopping criterion staggered algorithm are explained in detail. Advantages of such implementation and additional options such as thread-parallelization, element deletion, or contact problems are discussed. Chapter 4 deals with the examples of brittle, ductile and fatigue fracture on homogeneous materials and its numerical verification and/or experimental validation. Different phase-field formulations as well as material models are tested. Heterogeneous microstructural geometries obtained by the microtomography of nodular cast iron is analysed in Chapter 5. Different specimen sizes are used showing the influence of size, shape and arrangement of microconstituents. Finally, concluding remarks are given in Chapter 6 with suggestions for future research directions.

Chapter 2

Phase-field fracture formulation

Summary

This chapter presents the theoretical background for the phase-field fracture models of solid deformable bodies used in this thesis. The models are considered isothermal and derived under the assumptions of small-strain settings. The main features, detailed explanation and the derivation of governing equations based on the variational minimization problem is presented for the brittle fracture model. Two different phase-field formulations, used in this thesis and named AT-2 and TH, are shown with their main differences clearly displayed through the derivation of governing equations and their homogeneous solutions. The brittle fracture models are then used as a basis for extension towards ductile fracture problems. Hereby, the incorporation of plastic material behaviour with nonlinear isotropic hardening and combined nonlinear kinematic-isotropic hardening is introduced, while leaving the framework open for the implementation of many other plastic material models. Finally, the phase-field fracture model is extended to fatigue fracture problem, thus presenting a novel generalized phase-field fracture framework which is able to recover the quasi-static brittle/ductile fracture as well as the low- and high-cycle fatigue regime and transition, depending on the type of loading.

2.1. Brittle fracture model

2.1.1. Governing functional

An n-dimensional body $\Omega \subset \mathbb{R}^n$, $n \in [1,3]$ with its surface $\mathrm{d}\Omega \subset \mathbb{R}^{n-1}$ is considered with the evolving crack surface $\Gamma(t)$ and the corresponding displacement field **u**. Following the variational approach to fracture proposed by Francfort and Marigo [65], as an extension of the Griffith's fracture theory [1], the entire fracture process is governed by the minimization of the internal energy functional Ψ consisting of the body's internal, or bulk energy Ψ^{b} and the fracture-induced dissipating surface energy Ψ^{s}, as follows

$$\Psi = \Psi^{\mathrm{b}} + \Psi^{\mathrm{s}} = \int_{\Omega/\Gamma} \psi(\boldsymbol{\varepsilon}) \mathrm{d}\Omega + \int_{\Gamma} G_c \mathrm{d}\Gamma. \tag{2.1}$$

Such approach to fracture states that a body that is initially without a flaw may nucleate a crack under the influence of external load, if the resulting configuration has a lower total energy compared to the configuration where no crack forms. The crack propagation directions are then naturally obtained as those leading to the minimum energy configuration. Moreover, the cracks may branch and merge if it leads to a lower energy configuration than the simple crack extension, without the need to introduce any additional criteria.

For the case of (quasi-)brittle fracture the material behaviour is assumed to be linear elastic. Therefore, $\psi(\boldsymbol{\varepsilon})$ here corresponds to the elastic strain energy density function $\psi_{\mathrm{e}}(\boldsymbol{\varepsilon})$ given by $\psi_{\mathrm{e}}(\boldsymbol{\varepsilon}) = \frac{1}{2}\lambda \mathrm{tr}^2(\boldsymbol{\varepsilon}) + \mu \mathrm{tr}(\boldsymbol{\varepsilon}^2)$ with the Láme constants λ and μ, and the small strain tensor $\boldsymbol{\varepsilon}$.

The dissipated fracture surface energy Ψ^{s} is associated to the creation of new free surfaces upon the formation of crack. According to the Griffith's theory of fracture, the material fails upon reaching the critical value of fracture energy density G_{c}, which is a material parameter. In this work, the energy dissipation due to heat and sound release at the onset of fracture is neglected.

2.1.2. Fracture surface regularization

The explicit tracking of fracture surface $\Gamma(t)$ can be numerically costly and complicated when the interactions between multiple cracks are considered, especially in 3D settings. Therefore, the basic idea of the phase-field models is to approximate this discrete surface $\Gamma(t)$ by a crack density function $\gamma(\phi, \nabla\phi)$, using a phase-field order parameter $\phi \in [0,1]$. The parameter ϕ

describes the scalar damage field ranging smoothly between the broken $(\phi = 1)$ and the intact $(\phi = 0)$ material states, as proposed by Bourdin et al. [67]. That way the surface energy Ψ^s can be calculated as a domain integral. One way of obtaining the crack density function γ is by following the analogy of an infinite 1D bar and expanding it to 2D and 3D, as presented by Miehe et al. [71]. The bar is schematically represented in Fig. 2.1 with a fully formed crack at $x = 0$.

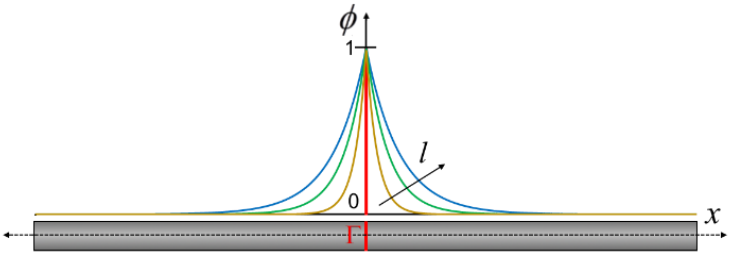

Fig. 2.1. An infinite 1D bar with a discrete crack Γ

The fracture surface energy Ψ^s can be then simply calculated as

$$\Psi^s = \int_\Gamma G_c \mathrm{d}\Gamma = G_c \cdot \Gamma, \tag{2.2}$$

where Γ, in this case, corresponds to the cross-sectional area of the bar. However, for the nontrivial solution of this problem, where the crack surface is not known, a sharp crack topology may be described by a scalar crack function

$$\phi(x) = e^{-|x|/l} \tag{2.3}$$

The length scale parameter l governs the width of the diffusive zone. The discrete fracture surface is then recovered for $l \to 0$. The exponential function (2.3) is the solution of the Euler homogenous differential equation

$$\phi(x) - l^2 \phi''(x) = 0 \quad \text{in } \Omega, \tag{2.4}$$

subjected to the boundary conditions $\phi(0) = 1$, $\phi(\pm\infty) = 0$, as shown in Fig. 2.1. Furthermore, (2.4) is associated with the variational problem

$$\phi(x) = Arg\left\{\inf_{\phi \in W} I(\phi)\right\}, \tag{2.5}$$

where

$$I(\phi)=\frac{1}{2}\int_{\Omega}\left(\phi^{2}+l^{2}\phi'^{2}\right)\mathrm{d}\Omega, \tag{2.6}$$

and $W=\left\{\phi\,|\,\phi(0)=1,\ \phi(\pm\infty)=0\right\}$. The integration of (2.6) over the volume $\mathrm{d}\Omega=\Gamma\mathrm{d}x$ returns $I\left(\phi=e^{-|x|/l}\right)=l\cdot\Gamma$, thus clearly relating the fracture surface to the length scale parameter *l*. A functional $\Gamma(\phi)$ can be then introduced as

$$\Gamma(\phi)=\frac{1}{l}I(\phi)=\frac{1}{2l}\int_{\Omega}\left(\phi^{2}+l^{2}\phi'^{2}\right)\mathrm{d}\Omega=\int_{\Omega}\gamma(\phi,\phi')\mathrm{d}\Omega, \tag{2.7}$$

where $\gamma(\phi,\phi')$ is the crack density function. Expanding (2.7) to the multiple dimensions yields

$$\gamma(\phi,\nabla\phi)=\frac{1}{2}\left[\frac{1}{l}\phi^{2}+l\left|\nabla\phi\right|^{2}\right]. \tag{2.8}$$

Note that the gradient of the phase-field significantly contributes to the phase-field description of fracture topology, showing great similarities to the gradient damage models [70]. Furthermore, the local part of the crack density function γ defines the decaying profile of ϕ, which will be discussed more thoroughly later. Schematic representation of the sharp crack topology approximation by the phase-field parameter ϕ and the influence of length scale parameter *l* on the width of transition zone is clearly displayed in Fig. 2.2.

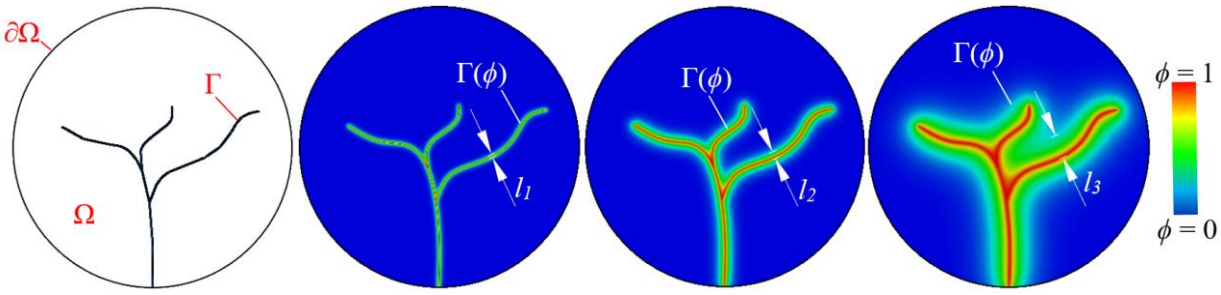

Fig. 2.2. Sharp crack topology Γ approximation represented with the parameter ϕ and the influence of length scale parameter "*l*" on the width of transition zone

The diffusive crack function (2.3) has to be bounded $\left(\phi\in[0,1]\right)$, symmetric and monotonically decreasing away from the location of crack. While it is obviously not the only function satisfying these conditions, it is the most commonly used function in the phase-field fracture models and is used in this work as well.

Some examples of different $\phi(x)$ function choices can be seen in Borden et al. [74], where $\phi(x) = \mathrm{e}^{-|x|/l} \cdot \left(1 + \frac{|x|}{l}\right)$ is used leading to the higher order phase-field theory, or in Pham et al. [153] where $\left\{\phi(x) = \left(1 - \frac{|x|}{\sqrt{2}l}\right)^2 \text{ for } x \in \left[-\sqrt{2}l, \sqrt{2}l\right], \text{ otherwise } \phi(x) = 0\right\}$ leads to a variational inequality problem.

2.1.3. Bulk Energy degradation

Correspondingly, the bulk energy term Ψ^{b} is regularized by the introduction of monotonically decreasing degradation function $g(\phi) \in [0,1]$ with the following properties

$$\begin{aligned} g(0) &= 1, \quad g'(0) < 0, \\ g(1) &= 0, \quad g'(1) = 0, \end{aligned} \tag{2.9}$$

to account for the subsequent loss of stiffness caused by the fracture initiation and propagation. For the detailed argumentation on the degradation function properties see Pham et al. [153].

The bulk energy term can now be written as

$$\Psi^b = \int_{\Omega/\Gamma} \psi(\boldsymbol{\varepsilon}) \mathrm{d}\Omega = \int_{\Omega} g(\phi) \cdot \psi(\boldsymbol{\varepsilon}) \mathrm{d}\Omega. \tag{2.10}$$

A commonly used form of degradation function satisfying (2.9) is the quadratic function $g(\phi) = (1-\phi)^2$ which is used throughout this thesis. On the other hand, the cubic function $g(\phi) = s\left[(1-\phi)^3 - (1-\phi)^2\right] + 3(1-\phi)^2 - 2(1-\phi)^3$ was proposed in Borden et al. [82], with the parameter *s* controlling the degradation function slope at the unbroken material state, i.e., $g(0)$. Moreover, Sargado et al. [154] proposed an exponential-type degradation function with 3 additional parameters and a corrector term, and made a detailed comparison with the already mentioned degradation function forms.

2.1.4. Strain energy decompositions

The bulk energy form (2.10) corresponds to the so-called isotropic case. This formulation cannot distinguish between the tensile and compressive state and is generally used in the problems where the tensile stresses are predominant. However, an additive decomposition of the elastic strain energy can be introduced to prevent the unphysical crack propagation in the

compressive stress state. Assuming only the degradation of the tensile strain energy part, the strain energy density term now reads $\psi_{\mathrm{e}}(\boldsymbol{\varepsilon},\phi) = g(\phi)\psi_{\mathrm{e}}^{+}(\boldsymbol{\varepsilon}) + \psi_{\mathrm{e}}^{-}(\boldsymbol{\varepsilon})$. Two most common energy decompositions used in the phase-field fracture models are considered here and will be used in the later examples, when necessary. First, the split into the volumetric and deviatoric contributions, proposed by Amor et al. [134], is considered as

$$\begin{aligned} \psi_{\mathrm{e}}^{+} &:= \tfrac{1}{2}\left(\lambda + \tfrac{2\mu}{n}\right)\left\langle \mathrm{tr}(\boldsymbol{\varepsilon})\right\rangle_{+}^{2} + \mu(\boldsymbol{\varepsilon}_{\mathrm{dev}} : \boldsymbol{\varepsilon}_{\mathrm{dev}}), \\ \psi_{\mathrm{e}}^{-} &:= \tfrac{1}{2}\left(\lambda + \tfrac{2\mu}{n}\right)\left\langle \mathrm{tr}(\boldsymbol{\varepsilon})\right\rangle_{-}^{2}, \end{aligned} \tag{2.11}$$

where $\langle x\rangle_{\pm} := \frac{1}{2}(x \pm |x|)$ are the Macaulay brackets, n represents the dimension number, and $\boldsymbol{\varepsilon}_{\mathrm{dev}} := \left(\boldsymbol{\varepsilon} - \frac{1}{3}\mathrm{tr}(\boldsymbol{\varepsilon})\mathbf{I}\right)$ stands for the deviatoric part of the strain tensor, with $\mathbf{I}$ being the second order unit tensor. Second option is the spectral split, which is based on the spectral decomposition of the strain tensor $\boldsymbol{\varepsilon}$. It was proposed by Miehe et al. [71] in the following form

$$\psi_{\mathrm{e}}^{\pm} := \tfrac{1}{2}\lambda\left\langle \mathrm{tr}(\boldsymbol{\varepsilon})\right\rangle_{\pm}^{2} + \mu\,\mathrm{tr}\left(\boldsymbol{\varepsilon}_{\pm}^{2}\right), \tag{2.12}$$

where $\boldsymbol{\varepsilon}_{\pm} := \sum_{i=1}^{n}\left\langle \varepsilon_i^{*}\right\rangle_{\pm}\mathbf{n}_i^{*}\otimes\mathbf{n}_i^{*}$ are the positive and negative parts of the strain tensor $\boldsymbol{\varepsilon}$ with $\left\{\varepsilon_i^{*}\right\}_{i=1}^{n}$ and $\left\{\mathbf{n}_i^{*}\right\}_{i=1}^{n}$ as the principal strains and their directions, respectively. It has to be noted that, although successfully resolving the unrealistic crack evolution behaviour under compressive loading, both energy decompositions show certain problems with the so-called crack boundary conditions [155]. Differences in the presented decomposition results on complex microstructural geometries is shown in [156]. More advanced energy decompositions have been proposed by Freddi and Royer-Carfagni [157] to model “no-tension masonry-like materials”. The decomposition is referred to as “No-tension split” where only the energy related to the positive-definite symmetric part of the strain tensor is degraded. Very recently Wu et al. [158] proposed similar split based on the effective stress tensor projection in energy norm thus alleviating some spurious behaviour of [157]. The directional split is presented in [155], decomposing the stress tensor with respect to the crack orientation.

2.1.5. Regularized functional

Finally, the regularized internal energy potential is obtained as follows

$$\Psi\left(\boldsymbol{\varepsilon},\phi\right)=\int_{\Omega}\left[g\left(\phi\right)\psi_{\mathrm{e}}^{+}\left(\boldsymbol{\varepsilon}\right)+\psi_{\mathrm{e}}^{-}\left(\boldsymbol{\varepsilon}\right)\right]\mathrm{d}\Omega+G_{\mathrm{c}}\int_{\Omega}\gamma\left(\phi,\nabla\phi\right)\mathrm{d}\Omega. \tag{2.13}$$

Different phase-field fracture formulations can be obtained by the combination of different degradation and crack density functions. The standard model used in a part of this thesis is obtained with $g\left(\phi\right)=\left(1-\phi\right)^{2}$ and $\gamma_{\text{AT-2}}\left(\phi,\nabla\phi\right)=\frac{1}{2}\left[\frac{1}{l}\phi^{2}+l\left|\nabla\phi\right|^{2}\right]$. It is commonly referred to as "AT-2" model [87, 100, 137], where AT stands for Ambrosio-Tortorelli and the corresponding type of regularization [69].

$$\Psi\left(\boldsymbol{\varepsilon},\phi\right)=\int_{\Omega}\left[\left(1-\phi\right)^{2}\psi_{\mathrm{e}}^{+}\left(\boldsymbol{\varepsilon}\right)+\psi_{\mathrm{e}}^{-}\left(\boldsymbol{\varepsilon}\right)\right]\mathrm{d}\Omega+G_{\mathrm{c}}\int_{\Omega}\frac{1}{2}\left[\frac{1}{l}\phi^{2}+l\left|\nabla\phi\right|^{2}\right]\mathrm{d}\Omega. \tag{2.14}$$

However, as it will be seen from the homogeneous solution of phase-field evolution, the phase-field parameter in this model evolves as soon as the material is loaded, thus omitting the fully linear elastic stage before the onset of fracture. On the other hand, linear elastic stage is recovered through the use of non-standard degradation function $g\left(\phi\right)$ in [82, 154], or the use of different crack density function in [153], corresponding to the so-called AT-1 model. Very similar model was proposed by Miehe et al. [88] and termed "Strain criterion with threshold model". Therein, the local part of fracture energy is represented by a linear term responsible for recovering the linear elastic stage. The model is introduced as

$$\Psi\left(\boldsymbol{\varepsilon},\phi\right)=\int_{\Omega}\left[\left(1-\phi\right)^{2}\psi_{\mathrm{e}}^{+}\left(\boldsymbol{\varepsilon}\right)+\psi_{\mathrm{e}}^{-}\left(\boldsymbol{\varepsilon}\right)\right]\mathrm{d}\Omega+\psi_{\mathrm{c}}\int_{\Omega}\left[2\phi+l^{2}\left|\nabla\phi\right|^{2}\right]\mathrm{d}\Omega, \tag{2.15}$$

where $\psi_{\mathrm{c}}=\frac{3}{8\sqrt{2}}\frac{G_{\mathrm{c}}}{l}$ is a constant specific fracture energy serving as an energetic threshold preventing the damage evolution. It is thus obvious that the model can be obtained from the general form (2.13) by choosing the standard degradation function $g\left(\phi\right)=\left(1-\phi\right)^{2}$, and the crack density function $\gamma_{\text{TH}}\left(\phi,\nabla\phi\right)=\frac{3}{8\sqrt{2}}\left[\frac{1}{l}2\phi+l\left|\nabla\phi\right|^{2}\right]$. The model shows great resemblance to AT-1 model [153]. Alongside the standard "AT-2" model, this model is also used in this thesis and will be termed "Threshold (TH)" model.

Note that the formulation (2.15) can also be obtained by introducing the threshold energy term ψ_c into the model with the standard $\gamma(\phi,\nabla\phi)$ function containing the quadratic local term as

$$\Psi(\boldsymbol{\varepsilon},\phi)=\int_\Omega\left\{(1-\phi)^2\left[\psi_e^+(\boldsymbol{\varepsilon})-\psi_c\right]+\psi_e^-(\boldsymbol{\varepsilon})+\psi_c\right\}\mathrm{d}\Omega+\psi_c\int_\Omega\left[\phi^2+l^2|\nabla\phi|^2\right]\mathrm{d}\Omega. \quad (2.16)$$

In the following steps, the governing equations for both models will be derived using the general form of the internal energy potential (2.13), until the point of departure.

2.1.6. Governing equations

The variation of the internal energy potential (2.13) yields

$$\delta\Psi=\frac{\partial\Psi}{\partial\boldsymbol{\varepsilon}}\delta\boldsymbol{\varepsilon}+\frac{\partial\Psi}{\partial\phi}\delta\phi=\int_\Omega\boldsymbol{\sigma}\,\delta\boldsymbol{\varepsilon}\,\mathrm{d}\Omega+\int_\Omega\left[\psi_e^+\frac{\mathrm{d}g(\phi)}{\mathrm{d}\phi}+G_c\frac{\partial\gamma(\phi,\nabla\phi)}{\partial\phi}\right]\delta\phi\,\mathrm{d}\Omega, \quad (2.17)$$

where the Cauchy stress $\boldsymbol{\sigma}$ is obtained as

$$\boldsymbol{\sigma}=g(\phi)\frac{\partial\psi_e^+}{\partial\boldsymbol{\varepsilon}}+\frac{\partial\psi_e^-}{\partial\boldsymbol{\varepsilon}}. \quad (2.18)$$

Accordingly, the variation of the external energy potential is formulated as

$$\delta W^{\mathrm{ext}}=\int_\Omega\bar{\mathbf{b}}\delta\mathbf{u}\,\mathrm{d}\Omega+\int_{\partial\Omega_{\bar{\mathbf{t}}}}\bar{\mathbf{t}}\delta\mathbf{u}\,\mathrm{d}\partial\Omega, \quad (2.19)$$

where $\bar{\mathbf{b}}$ and $\bar{\mathbf{t}}$ are the prescribed volume and surface force vectors, respectively. Expanding the (2.17) with appropriate crack density function $\gamma(\phi,\nabla\phi)$, implementing the small strain settings as $\boldsymbol{\varepsilon}=\frac{1}{2}\left[\nabla\mathbf{u}+\nabla^T\mathbf{u}\right]$ and applying the divergence theorem yields the variation of internal energy potential as

$$\begin{aligned}\delta\Psi_{\text{AT-2}}&=-\int_\Omega\nabla\cdot\boldsymbol{\sigma}\delta\mathbf{u}\mathrm{d}\Omega+\int_\Omega\left\{\frac{\mathrm{d}g(\phi)}{\mathrm{d}\phi}\psi_e^+(\boldsymbol{\varepsilon})+\frac{G_c}{l}\left[\phi-l^2\Delta\phi\right]\right\}\delta\phi\mathrm{d}\Omega\\&+\int_{\partial\Omega}\boldsymbol{\sigma}\cdot\mathbf{n}\delta\mathbf{u}\mathrm{d}\partial\Omega+\frac{G_c}{l}\int_{\partial\Omega}l^2\nabla\phi\cdot\mathbf{n}\delta\phi\mathrm{d}\partial\Omega\end{aligned} \quad (2.20)$$

for AT-2 model, and

$$\begin{aligned}\delta\Psi_{\text{TH}}&=-\int_\Omega\nabla\cdot\boldsymbol{\sigma}\delta\mathbf{u}\mathrm{d}\Omega+\int_\Omega\left\{\frac{\mathrm{d}g(\phi)}{\mathrm{d}\phi}\psi_e^+(\boldsymbol{\varepsilon})+2\cdot\frac{3}{8\sqrt{2}}\frac{G_c}{l}\left[1-l^2\Delta\phi\right]\right\}\delta\phi\mathrm{d}\Omega\\&+\int_{\partial\Omega}\boldsymbol{\sigma}\cdot\mathbf{n}\delta\mathbf{u}\mathrm{d}\partial\Omega+2\cdot\frac{3}{8\sqrt{2}}\frac{G_c}{l}\int_{\partial\Omega}l^2\nabla\phi\cdot\mathbf{n}\delta\phi\mathrm{d}\partial\Omega\end{aligned} \quad (2.21)$$

for TH model, where $\mathbf{n}$ is the outward-pointing normal vector on the boundary $\partial\Omega$.

Corresponding Euler equations can be now written in the strong form for both models as follows

$$\nabla\boldsymbol{\sigma}+\bar{\mathbf{b}}=0 \quad \text{in } \Omega, \tag{2.22}$$

$$\boldsymbol{\sigma}\cdot\mathbf{n}=\bar{\mathbf{t}} \quad \text{on } \partial\Omega_{\bar{\mathbf{t}}}, \tag{2.23}$$

$$\mathbf{u}=\bar{\mathbf{u}} \quad \text{on } \partial\Omega_{\bar{\mathbf{u}}}, \tag{2.24}$$

$$-l^2\Delta\phi+\left[1+\tilde{D}\right]\phi=\tilde{D} \quad \text{in } \Omega, \tag{2.25}$$

$$\nabla\phi\cdot\mathbf{n}=0 \quad \text{on } \partial\Omega, \tag{2.26}$$

with $\bar{\mathbf{u}}$ as the prescribed displacement vector. The Helmholtz type equation (2.25) representing the evolution of the phase-field parameter ϕ is derived in terms of the crack driving state function $\tilde{D}$ [88], which takes the form

$$\tilde{D}_{\text{AT-2}}=\frac{\psi_{\text{e}}^{+}}{\frac{1}{2}\frac{G_{\text{c}}}{l}} \tag{2.27}$$

for AT-2 model, and

$$\tilde{D}_{\text{TH}}=\frac{\psi_{\text{e}}^{+}}{\frac{3}{8\sqrt{2}}\frac{G_{\text{c}}}{l}}-1=\frac{\psi_{\text{e}}^{+}}{\psi_{\text{c}}}-1 \tag{2.28}$$

for TH model. It is then clear that the fracture evolution in the phase-field brittle fracture model is governed by the elastic strain energy term $\psi_{\text{e}}^{+}(\boldsymbol{\varepsilon})$. Note that $\tilde{D}_{\text{TH}}$ can be negative, leading to the unphysical solution $\phi<0$. Such behaviour is typical of models with linear local term in the crack density function $\gamma(\phi,\nabla\phi)$. A penalty function is introduced in [137, 153]. On the other hand, the addition of Macaulay brackets also resolves the issue, as presented in Miehe et al. [88]

$$\tilde{D}_{\text{TH}}=\zeta\left\langle\frac{\psi_{\text{e}}^{+}}{\psi_{\text{c}}}-1\right\rangle_{+}. \tag{2.29}$$

The non-dimensional parameter $\zeta>0$ is often embedded in [80, 88, 159-161] for calibration purposes, controlling the post-critical behaviour after the crack initialization. In TH model used in this work, the parameter ζ is set to 1, unless stated otherwise.

To summarize, two different phase-field formulations, named AT-2 and TH, will be used in this work. Although derived from different starting points and assumptions, their difference boils down to the description of crack driving state function $\tilde{D}$ as presented in this subsection.

2.1.7. Homogeneous solution

The homogeneous solution of the differential equation (2.25) can be calculated by ignoring all spatial derivatives of ϕ as

$$\phi_{\text{AT-2, TH}} = \frac{\tilde{D}_{\text{AT-2, TH}}}{1+\tilde{D}_{\text{AT-2, TH}}}, \tag{2.30}$$

with the assumption of isotropic model $\psi_{\text{e}}^{+} = \psi_{\text{e}}$, where no strain energy decomposition is included. Substitution of (2.30) into the constitutive equation $\sigma = g(\phi)\frac{\partial \psi_{\text{e}}}{\partial \varepsilon} = g(\phi) E\varepsilon$, where E is the Young's modulus, yields

$$\begin{aligned} \sigma_{\text{AT-2}} &= \frac{E\varepsilon\left(\frac{G_{\text{c}}}{l}\right)^2}{\left(\frac{G_{\text{c}}}{l}+E\varepsilon^2\right)^2}, \\ \sigma_{\text{TH}} &= \frac{E\varepsilon}{\left(\zeta\left\langle\frac{\psi_{\text{e}}^{+}}{\psi_{\text{c}}}-1\right\rangle_{+}+1\right)^2}. \end{aligned} \tag{2.31}$$

The maximal stress can then be calculated as

$$\begin{aligned} \sigma_{\text{AT-2}}^{\max} &= \frac{9}{16}\sqrt{\frac{EG_{\text{c}}}{3l}}, \\ \sigma_{\text{TH}}^{\max} &= \sqrt{2\frac{3}{8\sqrt{2}}\frac{EG_{\text{c}}}{l}}, \end{aligned} \tag{2.32}$$

from $\frac{\partial \sigma}{\partial \varepsilon} = 0$ for AT-2 model and the assumption $\psi_{\text{c}} = \frac{1}{2}E\varepsilon_{\text{c}}^2$ for TH model, as the σ_{TH} relation is not continuous. The parameter ε_{c} describes the critical strain at which fracture starts. This maximal stress $\sigma^{\max}$ is a material property corresponding to the ultimate stress commonly obtained from experimental measurements.

Note that the length scale parameter "*l*" influence can be clearly observed from (2.32) where the lower value of "*l*" leads to a higher critical value of maximal stress $\sigma^{\max}$, and vice versa.

As E, G_c and σ^{max} are material properties, the unknown length scale parameter l can be calculated for each model as

$$l_{\text{AT-2}} = \frac{27}{256}\frac{G_c E}{\left(\sigma^{max}\right)^2}, \qquad l_{\text{TH}} = \frac{3}{4\sqrt{2}}\frac{G_c E}{\left(\sigma^{max}\right)^2}. \tag{2.33}$$

It can thus be concluded that the length scale parameter l_{TH} calibrated for the TH model is approximately 5 times greater than the one for the AT-2 model, i.e. $l_{\text{TH}} = 5.0283 \cdot l_{\text{AT-2}}$. This allows the use of much coarser FE meshes. The homogeneous solutions are presented in Fig. 2.3.a) clearly showing differences between the two models in terms of stress-strain and phase-field parameter versus strain curves. Furthermore, the influence of the TH model parameter ζ is shown in Fig. 2.3.b).

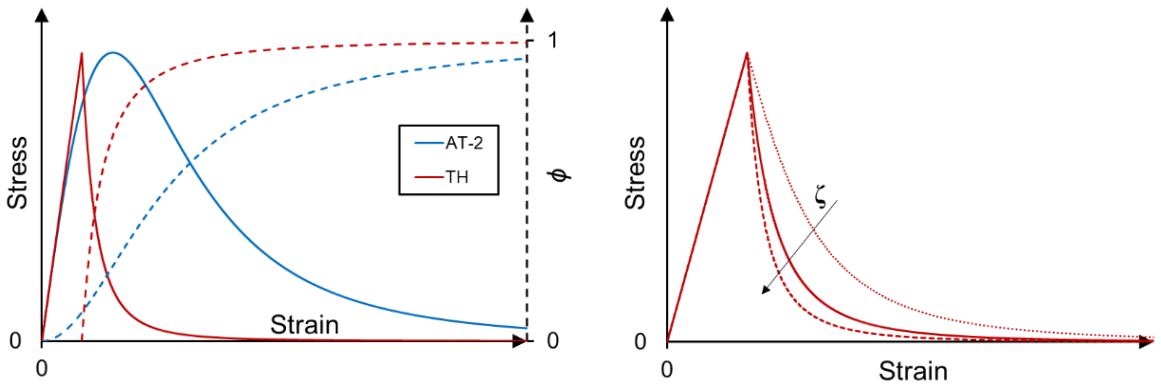

a) b)

Fig. 2.3. a) Homogeneous solution of the phase-field evolution, b) influence of the parameter ζ on the post-peak behaviour

2.1.8. Fracture irreversibility

To satisfy the principle of irreversibility, i.e., the second axiom of thermodynamics, the rate of dissipative fracture energy $\dot{\Psi}^s$ has to be non-negative, $\dot{\Psi}^s \geq 0$. Physically, it means preventing the crack healing after the load is removed. The basic idea is to somehow enforce the monotonicity of the phase-field parameter ϕ, i.e., $\dot{\phi} \geq 0$. As previously discussed in Introduction, there are a few different approaches to achieve irreversibility within the phase-field community. In this thesis, the so-called implicit enforcement of the constraint is used. It is based on the previous observation that $\tilde{D}\left(\psi_e^+\right)$ drives the fracture evolution (2.25). The

irreversibility condition can then be imposed by introducing the history field parameter $\mathcal{H}(t)$ [72] as

$$\mathcal{H}(t) := \max_{\tau=[0,t]} \tilde{D}\left(\psi_{\mathrm{e}}^{+}(\tau)\right), \tag{2.34}$$

thus rewriting the evolution equation (2.25) as

$$-l^2 \Delta\phi + \left[1+\mathcal{H}\right]\phi = \mathcal{H} \quad \text{in } \Omega. \tag{2.35}$$

As the crack driving force is now not allowed to decrease upon unloading, i.e., when ψ_{e}^{+} decreases, the constraint $\dot{\phi} \geq 0$ is enforced. Furthermore, the introduction of history field parameter $\mathcal{H}(t)$ enables an elegant decoupling of the governing equation system characteristic to the staggered solution scheme, presented in Chapter 3.

The presented brittle fracture models will now serve as a foundation for further expansion to the ductile and fatigue fracture problems.

2.2. Extension to ductile fracture

Ductile fracture is characterized by an extensive plastic deformation prior to the actual fracture. To extend the model to account for such fracture phenomenon, the bulk energy term Ψ^{b} is expanded to describe the plastic material behaviour as follows

$$\Psi^{\mathrm{b}}\left(\boldsymbol{\varepsilon}^{\mathrm{e}}, \boldsymbol{\varepsilon}^{\mathrm{p}}, \phi\right) = \int_{\Omega}\left[g(\phi)\psi_{\mathrm{e}}^{+}\left(\boldsymbol{\varepsilon}^{\mathrm{e}}\right) + \psi_{\mathrm{e}}^{-}\left(\boldsymbol{\varepsilon}^{\mathrm{e}}\right)\right]\mathrm{d}\Omega + \int_{\Omega} g(\phi)\psi_{\mathrm{p}}\left(\boldsymbol{\varepsilon}^{\mathrm{p}}\right)\mathrm{d}\Omega, \tag{2.36}$$

where $\boldsymbol{\varepsilon}^{\mathrm{e}}$ and $\boldsymbol{\varepsilon}^{\mathrm{p}}$ represent elastic and plastic strain tensors additively contributing to the total strain $\boldsymbol{\varepsilon} = \boldsymbol{\varepsilon}^{\mathrm{e}} + \boldsymbol{\varepsilon}^{\mathrm{p}}$. Such additive decomposition implies that the elastic response is not affected by plastic flow. The extension (2.36) directly follows the popular phase-field ductile fracture model proposed in Miehe et al. [80, 160], where the coupling between the accumulated plastic energy and fracture is achieved by the degradation of both elastic and plastic bulk energy. The coupling is one of the main differences between various phase-field ductile fracture models. For example, Ambati et al. [83] presented the model where the bulk degradation function is imposed only on elastic strain energy and embedded with the plasticity term $g\left(\phi, \varepsilon^{\mathrm{p}}\right)$ while no degradation of plastic energy is introduced. Therefore, the yield surface is not being

degraded, leading to the plastic strain evolution halt at the onset of damage which seems more physically correct. However, the model uses an additional parameter which should be somehow calibrated. Similar notion is presented in Alessi et al. [84, 162]. As already mentioned, the presented coupling is widely used due to its implementation simplicity. Moreover, it is easily extended to the fatigue fracture models, as presented in the next subchapter, and is therefore used in this thesis.

The plastic energy potential $\psi_{\mathrm{p}}\left(\boldsymbol{\varepsilon}^{\mathrm{p}}\right)$ can be represented by a large variety of plasticity models. The governing equations derivation is straightforward, analogous to the previously shown brittle models. In fact, the same governing equations are obtained with the only difference being the crack driving state function which is now expanded with plastic energy term as

$$\begin{aligned} \tilde{D}_{\text{AT-2}} &= \frac{\psi_{\mathrm{e}}^{+}}{\frac{1}{2}\frac{G_{\mathrm{c}}}{l}} + \frac{\psi_{\mathrm{p}}}{\frac{1}{2}\frac{G_{\mathrm{c}}}{l}}, \\ \tilde{D}_{\text{TH}} &= \zeta \left\langle \frac{\psi_{\mathrm{e}}^{+}}{\psi_{\mathrm{c}}} + \frac{\psi_{\mathrm{p}}}{\psi_{\mathrm{c}}} - 1 \right\rangle_{+}. \end{aligned} \tag{2.37}$$

In this work, plasticity models employing the von Mises yield criterion are used with (non-) linear isotropic hardening and the combined nonlinear isotropic and kinematic hardening. These models are well suited for most metals. The derivation of the plasticity model with combined isotropic-kinematic hardening will be shown here, as the model with (non-)linear isotropic hardening can be then considered a special case.

The plastic energy dissipation potential can be written as

$$\psi^{\mathrm{p}}\left(\boldsymbol{\varepsilon}^{\mathrm{p}}\right) = \int_0^t \left(\operatorname{dev}\left[\boldsymbol{\sigma}^{*}\right] - \boldsymbol{\alpha}\right) : \dot{\boldsymbol{\varepsilon}}^{\mathrm{p}} \mathrm{d}t, \tag{2.38}$$

where $\boldsymbol{\sigma}^{*}$ is the effective (non-degraded) Cauchy stress tensor and $\boldsymbol{\alpha}$ is the backstress tensor accounting for the shift of the yield surface. Note that the equations are derived in the effective stress space, meaning that the plastic material response is not affected by the evolution of phase-field parameter. The effective plastic energy dissipation potential ψ^{p} is convex and positive satisfying $\psi^{\mathrm{p}}\left(0\right) = 0$.

The isotropic hardening function controls the size of the yield surface $\sigma_{\mathrm{y}}\left(\varepsilon_{\mathrm{eqv}}^{\mathrm{p}}\right)$. A few different options of yield surface function $\sigma_{\mathrm{y}}\left(\varepsilon_{\mathrm{eqv}}^{\mathrm{p}}\right)$ are used in this thesis and presented where appropriate. $\dot{\varepsilon}_{\mathrm{eqv}}^{\mathrm{p}}$ is the equivalent plastic strain rate whose evolution is defined as

$$\dot{\varepsilon}_{\mathrm{eqv}}^{\mathrm{p}} = \sqrt{\tfrac{2}{3}\dot{\boldsymbol{\varepsilon}}^{\mathrm{p}} : \dot{\boldsymbol{\varepsilon}}^{\mathrm{p}}}. \tag{2.39}$$

The von Mises plasticity criterion postulates that the plastic flow does not affect the change of volume. Therefore, only the deviatoric part of the stress tensor, which is a work-conjugate to the deviatoric strain describing the shape change, is used to construct the pressure-independent yield function

$$F = \left\| \mathrm{dev}\left[\boldsymbol{\sigma}^{*}\right] - \boldsymbol{\alpha} \right\| - \sqrt{\tfrac{2}{3}}\sigma_{\mathrm{y}}\left(\varepsilon_{\mathrm{eqv}}^{\mathrm{p}}\right) \leq 0, \tag{2.40}$$

where $\|\bullet\|$ is a second vector norm. The associated plastic flow is assumed as

$$\dot{\boldsymbol{\varepsilon}}^{\mathrm{p}} = \gamma \frac{\partial F}{\partial \boldsymbol{\sigma}^{*}}, \tag{2.41}$$

where γ is the plastic multiplicator obtained by the return-mapping algorithm. The nonlinear kinematic hardening evolution law is defined according to Chaboche [163] multicomponent model as

$$\dot{\boldsymbol{\alpha}}_{k} = C_{k} \frac{1}{\sigma_{y}\left(\varepsilon_{\mathrm{eqv}}^{\mathrm{p}}\right)} \left(\mathrm{dev}\left[\boldsymbol{\sigma}^{*}\right] - \boldsymbol{\alpha}\right) \dot{\varepsilon}_{\mathrm{eqv}}^{\mathrm{p}} - \gamma_{k} \boldsymbol{\alpha}_{i} \dot{\varepsilon}_{\mathrm{eqv}}^{\mathrm{p}}. \tag{2.42}$$

Each backstress component $\boldsymbol{\alpha}_{k}$ is defined by the material parameters C_{k} and γ_{k} determining the initial kinematic hardening modulus and the rate of its decrease with increasing plastic deformation, respectively. The addition of the nonlinear term thus limits the translation of the yield surface in principal stress space. Total backstress tensor is then obtained as

$$\boldsymbol{\alpha} = \sum_{k} \boldsymbol{\alpha}_{k}. \tag{2.43}$$

When kinematic material parameters C_{k} and γ_{k} are set to zero, the model reduces to an isotropic hardening model. Moreover, when only γ_{k} is set to zero, the linear Ziegler hardening

law is recovered, removing the limiting surface. The isotropic and kinematic hardening phenomena are schematically represented in Fig. 2.4 in the deviatoric stress space.

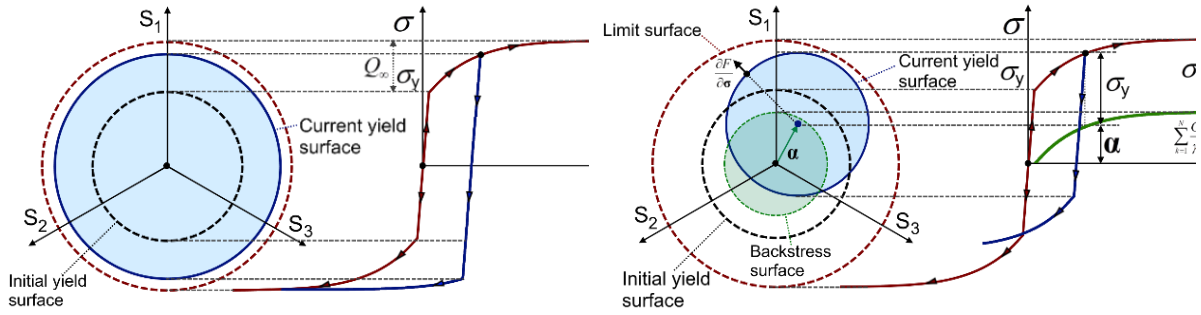

Fig. 2.4. Schematic representation of a) nonlinear Isotropic and b) nonlinear Kinematic hardening

The combined isotropic-kinematic model features allow modelling of inelastic deformation in metals subjected to the cyclic loads and resulting in low-cycle fatigue failure. Such models are able to reproduce the characteristic cyclic phenomena as Bauschinger effect causing a reduced yield stress upon load reversal; plastic shakedown characteristic of symmetric stress- or strain-controlled experiments where soft or annealed metals tend to harden toward a stable limit, and initially hardened metals tend to soften; progressive “ratcheting” or “creep” in the direction of the mean stress related to the unsymmetrical stress cycles between prescribed limits; or the relaxation of the mean stress observed in an unsymmetrical strain-controlled experiment.

2.3. Extension to fatigue fracture

Material fatigue is a material weakening phenomenon caused by the cyclic loading whose maximum value is below the monotonic strength of the material. It can result in a progressive structural damage and crack growth. Although fatigue has traditionally been associated with metal components, most materials seem to experience some sort of fatigue-related failure. Once initiated, a fatigue crack will steadily grow until it reaches the critical size producing rapid crack propagation following a complete structural failure. Fig. 2.5.a) shows the crack growth rate curve, usually obtained in fatigue fracture experiments, approximated by Paris Law [4], or its often used extension - the NASGRO equation [164]. The material fatigue life cycle is generally divided into low- and high-cyclic fatigue regimes, as presented by strain-life, $\varepsilon - N$ curve in Fig. 2.5. b), where the low-cyclic fatigue is usually accompanied by the occurrence of plastic deformation. Such strain-life approach is suitable for materials exhibiting plastic

behaviour. The stress-life portrayed through the Wöhler curve is usually reserved for high-cyclic fatigue regime, where the underlaying material behaviour is elastic.

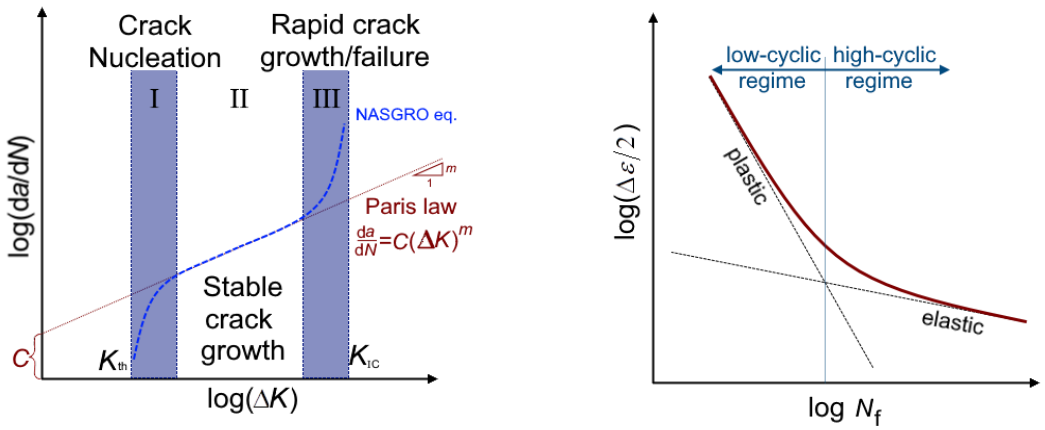

a) b)

Fig. 2.5 a) Crack growth curve approximated by Paris law where *a* is the crack length, *N* presents number of cycles, *K* is stress intensity factor, while *C* and *m* are material properties, b) Strain-life curve where $\Delta\varepsilon$ is the load amplitude and N_f is the number of cycles to failure

The previously shown phase-field ductile fracture model is actually capable of producing some features of the low-cyclic fatigue regime. The plastic potential (2.38) is monotonic and irreversible, by definition, causing the crack driving function (2.37) to increase during the loading cycles, eventually leading to the onset of fracture. On the other hand, it is not able to reproduce the crack initiation, nor the crack growth, when the applied cyclic loads are below the plasticity limit in ductile materials, or the fracture limit in brittle materials, corresponding to the high-cyclic fatigue regime.

In this subsection, the presented phase-field models for brittle and ductile fracture are extended to account for the fatigue phenomena. The presented extension contains only one additional material parameter ($\bar{\psi}_\infty$, explained later), enabling it to reproduce the main material fatigue features. The goal is then to produce a generalized phase-field framework which can, depending on the type of loading, recover brittle/ductile fracture in monotonic as well as low- and high-cycle fatigue regime, including the transition between the fatigue regimes. The general idea is to introduce the fracture energy degradation due to the repeated externally applied loads. Physically, it would mean the decline of material fracture properties during the cyclic loading, which eventually causes the crack initiation and propagation occurrence. In a way, material "mileage" would be introduced. To that end, a local energy density accumulation variable $\bar{\psi}(t)$ is introduced accounting for the changes in strain energy density $\psi(\boldsymbol{\varepsilon})$ during

the loading cycles, thus taking the structural loading history into account. A fatigue degradation function $\hat{F}(\bar{\psi})$ is introduced affecting the fracture energy term as discussed. The generalised internal energy potential can be now written as

$$\Psi\left(\boldsymbol{\varepsilon}^{\mathrm{e}},\boldsymbol{\varepsilon}^{\mathrm{p}},\phi,\bar{\psi}\right)=\int_{\Omega}\left\{g(\phi)\left[\psi_{\mathrm{e}}^{+}\left(\boldsymbol{\varepsilon}^{\mathrm{e}}\right)+\psi_{\mathrm{p}}\left(\boldsymbol{\varepsilon}^{\mathrm{p}}\right)\right]+\psi_{e}^{-}\left(\boldsymbol{\varepsilon}^{\mathrm{e}}\right)\right\}\mathrm{d}\Omega+\hat{F}(\bar{\psi})G_{\mathrm{c}}\int_{\Omega}\gamma(\phi,\nabla\phi)\mathrm{d}\Omega. \tag{2.44}$$

It is similar to the phase-field fatigue fracture formulation for the brittle materials, proposed in Carrara et al. [120] and Alessi et al. [119]. After the derivation of the model, it is obvious that such a fatigue extension only changes the crack driving state function $\tilde{D}$ as follows

$$\begin{aligned}\tilde{D}_{\text{AT-2}}&=\frac{\psi_{\mathrm{e}}^{+}}{\hat{F}(\bar{\psi})\frac{1}{2}\frac{G_{\mathrm{c}}}{l}}+\frac{\psi_{\mathrm{p}}}{\hat{F}(\bar{\psi})\frac{1}{2}\frac{G_{\mathrm{c}}}{l}}.\\ \tilde{D}_{\text{TH}}&=\zeta\left\langle\frac{\psi_{\mathrm{e}}^{+}}{\hat{F}(\bar{\psi})\psi_{\mathrm{c}}}+\frac{\psi_{\mathrm{p}}}{\hat{F}(\bar{\psi})\psi_{\mathrm{c}}}-1\right\rangle_{+}.\end{aligned} \tag{2.45}$$

In this section, only TH phase-field formulation model will be used to account for the linear elastic material behaviour prior to fracture or plastic yielding.

2.3.1. Local energy density accumulation variable $\bar{\psi}(t)$

This variable is conceived as a local measure of repeated strain energy changes during the loading history. It is a major feature of the novel generalized phase-field fatigue formulation. To fully fit into this framework, it should not affect the proportional (monotonic) loading case. To satisfy this condition, in this work, the variable is introduced as the sum of *negative* differences of the total strain energy density during the cyclic loading. That way, the variable value increases only during the unloading part of the cycle, consequently degrading the fracture material properties. Note that the plastic energy density $\psi_{\mathrm{p}}(t)$ is dissipative, and therefore never decreasing. The degradation of fracture properties due to fatigue is then, in fact, only influenced by the repetitive changes in elastic strain energy density $\psi_{\mathrm{e}}\left(\boldsymbol{\varepsilon}^{\mathrm{e}}\right)$.

The basic idea is explained schematically on the example of 1D bar subjected to the sinusoidal displacement with load ratio $R = 0$ and three different amplitudes A1 < A2 < A3. Unlike the amplitudes A2 and A3, the loading amplitude A1 is below the material plastic limit,

characteristic to the high-cycle fatigue regime. The evolution of total energy $\left(\psi_{\mathrm{e}}+\psi_{\mathrm{p}}\right)$ and energy accumulation variable $\bar{\psi}(t)$ is shown in Fig. 2.6.

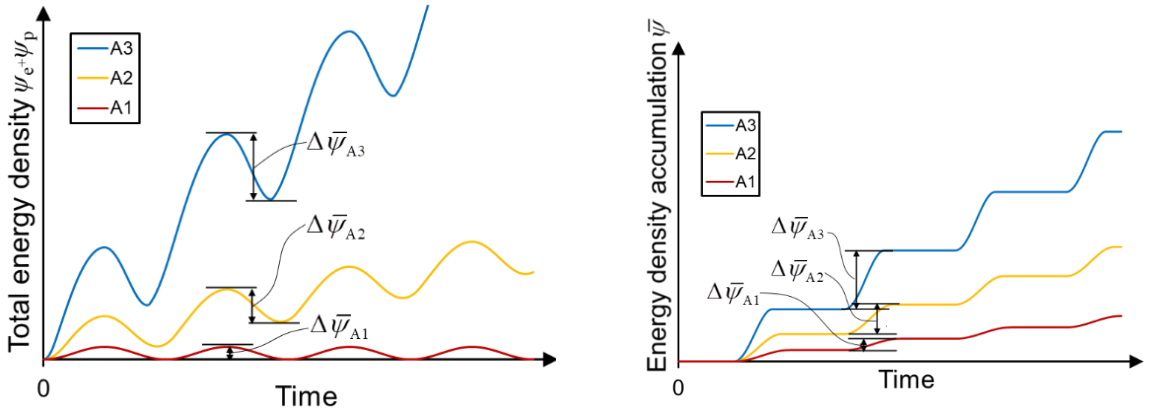

a) b)

Fig. 2.6. a) Total strain energy density and b) Energy density accumulation variable of 1D bar subjected to sinusoidal displacement-controlled loading

The maximum strain energy value of the curve corresponding to the amplitude A1 does not increase through the course of cycles. On the other hand, the increase of the maximum total strain energy due to the increase of plastic dissipation $\psi_{\mathrm{p}}(t)$ over the cycles can be clearly seen for curves corresponding to amplitudes A2 and A3. Furthermore, a clear peak shift to the left caused by the kinematic hardening plasticity is observed.

The only difference distinguishing between the high- and low-cycle fatigue regime is the influence of plastic energy $\psi_{\mathrm{p}}(t)$ on the crack driving state function $\tilde{D}$ in the low-cycle fatigue regime. The competition is thus introduced between the total strain energy $\left(\psi_{\mathrm{e}}+\psi_{\mathrm{p}}\right)$ (whose maximal value is constant for the case of high-cyclic fatigue regime, and increasing in low-cyclic for the case of constant load amplitudes), and the fracture resistance decrease due to the repetitive change in elastic energy, i.e., fatigue.

The local energy density accumulation function can be then formulated in the integral form as

$$\bar{\psi}(t)=\int_0^t \psi_{\mathrm{e}}(t)\,H\left(-\dot{\psi}_{\mathrm{e}}\right)\mathrm{d}t, \tag{2.46}$$

where $H\left(-\dot{\psi}_{\mathrm{e}}\right)$ is the Heaviside function taking the value of 1 when $\dot{\psi}_{\mathrm{e}}>0$ and the value of 0 when $\dot{\psi}_{\mathrm{e}}\le 0$. The incremental form can be written as

$$\bar{\psi}_N = \bar{\psi}_{N-1} - \langle \psi_N - \psi_{N-1} \rangle_- , \tag{2.47}$$

where N is the cycle number.

The energy density accumulation variable increases only during the unloading, thus not affecting the proportional loading cases, as clearly seen during the first cycle in Fig. 2.6. b).

Mean load effect

The energy density accumulation variable description implicitly includes the mean load effect often expressed by a load ratio $R = \frac{\sigma_{\min}}{\sigma_{\max}} = \frac{F_{\min}}{F_{\max}}$ in experimental measurements. For the shown case of strain-control loaded bar, the load ratio can be expressed as $R = \frac{\varepsilon_{\min}}{\varepsilon_{\max}}$, with $\varepsilon_{\mathrm{M}} = \frac{\varepsilon_{\max} + \varepsilon_{\min}}{2}$ being the mean strain imposed to the bar. The strain energy density amplitude can then be written as $\Delta\psi_{\mathrm{e}} = \frac{1}{2} E \left(\varepsilon_{\max}^2 - \varepsilon_{\min}^2 \right) = 2E\varepsilon_{\mathrm{M}}^2 \frac{1+R^2}{(1+R)^2}$, for the case where maximum load value does not reach the plastic yield limit, and $R \geq 0$. This clearly proves the mean load and the load ratio influence is considered. It is further explained on the example of 1D bar loaded with sinusoidal displacements B1 and B2 of same amplitudes, but different mean values, as presented in Fig. 2.7.

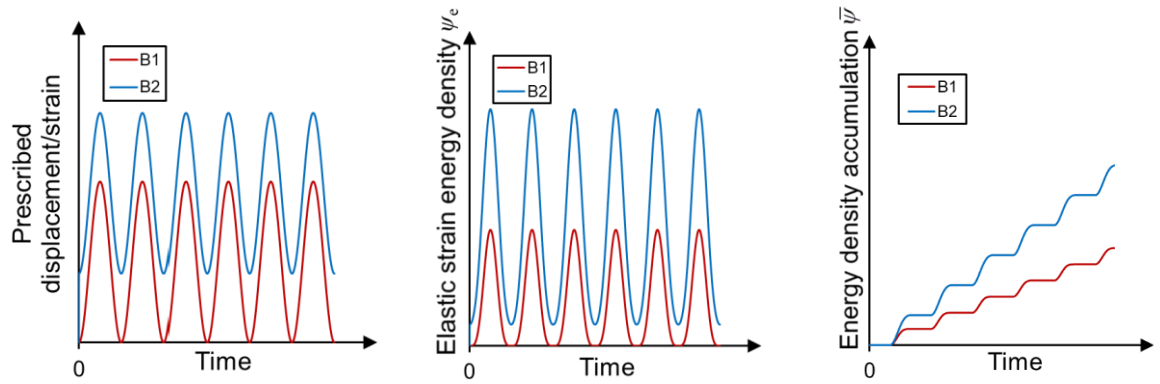

Fig. 2.7. a) Prescribed load, b) resulting elastic strain energy and c) energy accumulation variable of 1D bar subjected to sinusoidal displacement-controlled loading with different mean values

The loads with the equal displacement amplitudes, or strain therefore, with different mean values, produce much different strain energy values. Consequently, the accumulated energy density variable obtained by the higher mean load case (B2 in Fig. 2.7) increases much faster than in the lower mean load case (B1), as predicted.

2.3.2. Fatigue degradation function $\hat{F}(\bar{\psi})$

Following the proper definition of the energy density accumulation variable $\bar{\psi}(t)$, the degradation of the fracture energy has to be defined. Herein, the fatigue degradation function $\hat{F}(\bar{\psi}) \in [0,1]$ is introduced. It should be continuous and piecewise differentiable with the following properties

$$\begin{aligned} \hat{F}(\bar{\psi}=0) &= 1, \\ \hat{F}(\bar{\psi}\to\infty) &= 0, \\ \frac{\mathrm{d}\hat{F}}{\mathrm{d}t}(0<\bar{\psi}<\infty) &\le 0. \end{aligned} \tag{2.48}$$

Similar degradation function properties have been used in [119, 120]. In this thesis, three functions are presented fitting the given description. Their respective semi-logarithmic graphs are shown in Fig. 2.8 and Fig. 2.9.

$$\begin{aligned} \hat{F}_1 &= \left(1-\frac{\bar{\psi}}{\bar{\psi}+\bar{\psi}_\infty}\right)^2 \quad \text{for} \quad \bar{\psi}\in[0,+\infty], \\ \hat{F}_2 &= \left(1-\frac{\bar{\psi}}{\bar{\psi}_\infty}\right)^2 \quad \text{for} \quad \bar{\psi}\in[0,\bar{\psi}_\infty], \\ \hat{F}_3 &= \left(\xi\log\frac{\bar{\psi}_\infty}{\bar{\psi}}\right)^2 \quad \text{for} \quad \bar{\psi}\in\left[\bar{\psi}_\infty, 10^{\frac{1}{\xi}}\cdot\bar{\psi}_\infty\right]. \end{aligned} \tag{2.49}$$

$\bar{\psi}_\infty$ is the newly introduced parameter needed to bound the functions between 0 and 1 and is therefore included in every function. It can be seen as a fatigue material parameter whose physical interpretation will be provided through the next simple examples, as well as the numerical examples in Chapter 4 and Chapter 5. The parameter ξ embedded into $\hat{F}_3$ is introduced to allow for better fine-tuning, similar to the parameter ζ in (2.29).

The following figures present the proposed fatigue degradation functions in terms of number of cycles *N* for the cyclically loaded 1D bar. Pure elastic material behaviour is assumed, leading to a constant change of the elastic strain energy density $\Delta\psi$ during each cycle. A clear link between the number of cycles *N* and energy density accumulation variable $\bar{\psi}$ can be then constructed as $\bar{\psi}=\Delta\psi\cdot N$. Fig. 2.8 shows the influence of the parameter $\bar{\psi}_\infty$ in each function

expressed as the multiples of elastic strain energy density change $\Delta\psi$ during a cycle. The influence of the loading amplitude, expressed as $\frac{\Delta\psi}{\psi_c}$, is presented in Fig. 2.9.

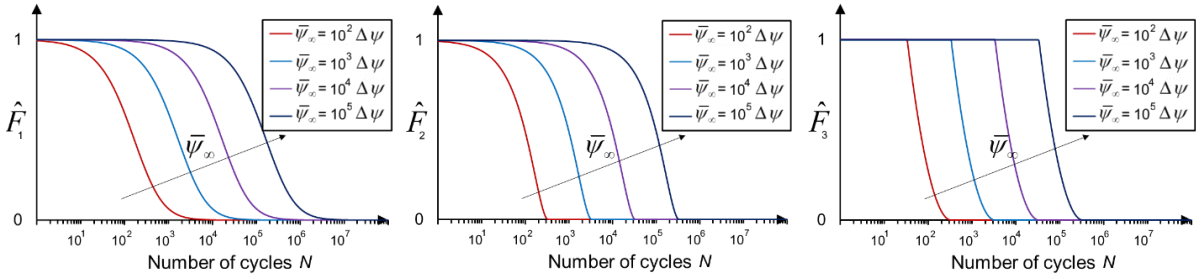

a) b) c)

Fig. 2.8. Influence of parameter $\bar{\psi}_\infty$ for three different fatigue degradation functions a) $\hat{F}_1$, b) $\hat{F}_2$, c) $\hat{F}_3$

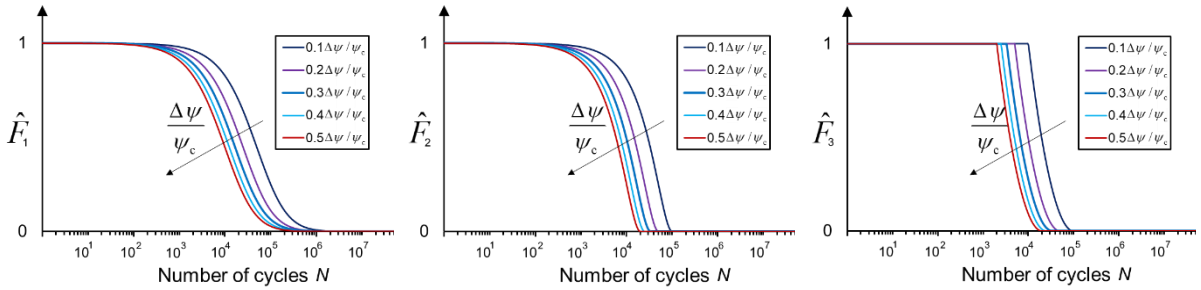

a) b) c)

Fig. 2.9. Influence of loading amplitude expressed as $\frac{\Delta\psi}{\psi_c}$ for three different fatigue degradation functions a) $\hat{F}_1$, b) $\hat{F}_2$, c) $\hat{F}_3$

The parameter $\bar{\psi}_\infty$ obviously affects the cycle number at which the fatigue degradation takes off, with all other parameters being equal. The physical interpretation of this parameter will be explored through the parametric study conducted in Section 4.3.3.2. On the other hand, the increase in the loading amplitude would cause earlier onset of fatigue degradation. Lastly, the influence of the tuning parameter ξ is observed in Fig. 2.10.

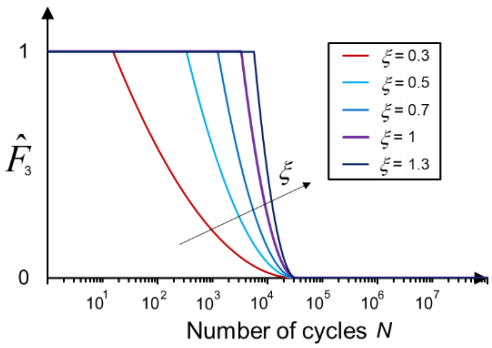

Fig. 2.10. Influence of parameter ξ in the fatigue degradation function $\hat{F}_3$

Chapter 3

Numerical implementation

Summary

This chapter presents the numerical implementation of the generalized phase-field fracture model. First, a general FE equation system is derived together with the explanation of staggered solution scheme basics. The single iteration staggered scheme and iterative staggered scheme with residual control-based stopping criterion are shown. The implementation of the staggered algorithm with residual control within the commercial FE software ABAQUS is then explained in detail. Major advantages and features of such implementation are discussed together with additional options including, different solvers, automatic incrementation, element deletion, coupled contact analysis, and thread parallelization, also employed in this thesis. Finally, the implementation of a cycle skipping technique for the analysis of high-cycle fatigue fracture is presented and detailly explained. The complete implementation files (the source code and input files), containing numerical examples shown later, as well as detailed explanations and instructions for users are made openly accessible on Mendeley repository [133].

3.1. Finite element model

3.1.1. Discretization

To implement the presented phase-field fracture models, the domain Ω is discretized by finite elements containing the displacement $\mathbf{v}_i^{\mathrm{T}} = \begin{bmatrix} u_i & v_i & w_i \end{bmatrix}$ and phase-field ϕ_i degrees of freedom (DOFs). The subscript "*i*" represents the node number while *u*, *v* and *w* represent the displacements in *x*, *y* and *z* directions of local coordinate system, respectively. The same shape functions N_i interpolate both the displacement and the phase-field variable

$$\begin{aligned} \mathbf{u} &= \textstyle\sum_i^{\mathrm{n}} \mathbf{N}_i^{\mathbf{v}} \mathbf{v}_i, \qquad & \boldsymbol{\varepsilon} &= \textstyle\sum_i^{\mathrm{n}} \mathbf{B}_i^{\mathbf{v}} \mathbf{v}_i, \\ \phi &= \textstyle\sum_i^{\mathrm{n}} \mathrm{N}_i \phi_i, & \nabla\phi &= \textstyle\sum_i^{\mathrm{n}} \mathbf{B}_i^{\phi} \phi_i, \end{aligned} \tag{3.1}$$

where n is the total number of nodes in the element. The general form of the shape function matrix **N** and the spatial derivative matrix **B** is given here for the 3D case

$$\mathbf{N}_i^{\mathbf{v}} = \begin{bmatrix} \mathrm{N}_i & 0 & 0 \\ 0 & \mathrm{N}_i & 0 \\ 0 & 0 & \mathrm{N}_i \end{bmatrix}, \qquad \mathbf{B}_i^{\phi} = \begin{bmatrix} \mathrm{N}_{i,x} \\ \mathrm{N}_{i,y} \\ \mathrm{N}_{i,z} \end{bmatrix}, \qquad \mathbf{B}_i^{\mathbf{v}} = \begin{bmatrix} \mathrm{N}_{i,x} & 0 & 0 \\ 0 & \mathrm{N}_{i,y} & 0 \\ 0 & 0 & \mathrm{N}_{i,z} \\ 0 & \mathrm{N}_{i,z} & \mathrm{N}_{i,y} \\ \mathrm{N}_{i,z} & 0 & \mathrm{N}_{i,x} \\ \mathrm{N}_{i,y} & \mathrm{N}_{i,x} & 0 \end{bmatrix}. \tag{3.2}$$

Thus, a general framework for FE implementation is provided. The choice of the underlaying element type is introduced via the corresponding **N** and **B** matrices and the displacement vector $\mathbf{v}_i$. This form can be easily employed to a number of different element types using the Voigt notation by choosing the appropriate shape N functions or reducing/reshaping $\mathbf{N}_i^{\mathbf{v}}$ and $\mathbf{B}_i^{\phi}$ matrices.

3.1.2. Virtual work principle

The finite element model is based on the weak form equations of the internal energy potential which can now be written as

$$\delta\Psi = \int_\Omega \boldsymbol{\sigma}\,\delta\boldsymbol{\varepsilon}\,\mathrm{d}\Omega + \int_\Omega \left\{ \frac{\mathrm{d}g(\phi)}{\mathrm{d}\phi}\left(\psi_{\mathrm{e}}^{+} + \psi_{\mathrm{p}}\right) + \hat{F}\left(\bar{\psi}\right) G_{\mathrm{c}} \frac{\partial\gamma(\phi,\nabla\phi)}{\partial\phi} \right\} \delta\phi\,\mathrm{d}\Omega = \delta W^{\mathrm{int}}, \tag{3.3}$$

for the generalized phase-field fracture model. Therein, $\boldsymbol{\sigma}$ represents the degraded Cauchy stress. After the inclusion of appropriate functions $g(\phi)$ and $\gamma(\phi,\nabla\phi)$ for each model, the virtual work principle $\delta W^{\text{ext}} - \delta W^{\text{int}} = 0$ can be then discretized as

$$\left(\mathbf{F}^{\mathbf{v}}_{\text{ext}} - \mathbf{F}^{\mathbf{v}}_{\text{int}}\right)\delta\mathbf{v} + \left(\mathbf{F}^{\phi}_{\text{ext}} - \mathbf{F}^{\phi}_{\text{int}}\right)\delta\phi = 0, \tag{3.4}$$

where

$$\begin{aligned} \mathbf{F}^{\mathbf{v}}_{\text{ext}} &= \int_{\Omega} \mathbf{N}^{\mathbf{v}}\bar{\mathbf{b}}\,\mathrm{d}\Omega + \int_{\partial\Omega_{\bar{\mathbf{t}}}} \mathbf{N}^{\mathbf{v}}\bar{\mathbf{t}}\,\mathrm{d}\partial\Omega, \\ \mathbf{F}^{\phi}_{\text{ext}} &= 0, \end{aligned} \tag{3.5}$$

are the external force vectors. $\mathbf{F}^{\mathbf{v}}_{\text{int}}$ and $\mathbf{F}^{\phi}_{\text{int}}$ correspond to the internal force vectors associated with the discretized displacements and phase-field, respectively, as follows

$$\begin{aligned} \mathbf{F}^{\mathbf{v}}_{\text{int}} &= \int_{\Omega} \mathbf{B}^{\mathbf{v}^{\mathrm{T}}}\boldsymbol{\sigma}\,\mathrm{d}\Omega, \\ \mathbf{F}^{\phi}_{\text{int}} &= \int_{\Omega} \left\{ l^2\mathbf{B}^{\phi^{\mathrm{T}}}\mathbf{B}^{\phi}\,\boldsymbol{\phi} + \left(\left[1+\mathcal{H}\right]\mathbf{N}^{\phi}\boldsymbol{\phi} - \mathcal{H}\right)\mathbf{N}^{\phi} \right\} \mathrm{d}\Omega, \end{aligned} \tag{3.6}$$

where $\boldsymbol{\phi}$ is the vector containing phase-field DOFs ϕ_i. The difference between the AT-2 and TH formulations is embedded in the history field $\mathcal{H}$ (2.34), and includes all the important features for resolving brittle/ductile fracture in monotonic loading and fatigue fracture in cyclic loading.

3.1.3. Residual vectors and stiffness matrices

Residual vectors can be now obtained as $\mathbf{R} = \mathbf{F}_{\text{ext}} - \mathbf{F}_{\text{int}}$ leading to

$$\begin{aligned} \mathbf{R}^{\mathbf{v}} &= \int_{\Omega} \mathbf{N}^{\mathbf{v}}\bar{\mathbf{b}}\,\mathrm{d}\Omega + \int_{\partial\Omega_{\bar{\mathbf{t}}}} \mathbf{N}^{\mathbf{v}}\bar{\mathbf{t}}\,\mathrm{d}\partial\Omega - \int_{\Omega} \mathbf{B}^{\mathbf{v}^{\mathrm{T}}}\boldsymbol{\sigma}\,\mathrm{d}\Omega \\ \mathbf{R}^{\phi} &= -\int_{\Omega} \left\{ l^2\mathbf{B}^{\phi^{\mathrm{T}}}\mathbf{B}^{\phi}\,\boldsymbol{\phi} + \left(\left[1+\mathcal{H}\right]\mathbf{N}^{\phi}\boldsymbol{\phi} - \mathcal{H}\right)\mathbf{N}^{\phi} \right\} \mathrm{d}\Omega. \end{aligned} \tag{3.7}$$

Correspondingly, the stiffness matrices are obtained as

$$\begin{aligned} \mathbf{K}^{\mathbf{vv}} &= -\frac{\partial\mathbf{R}^{\mathbf{v}}}{\partial\mathbf{v}} = \int_{\Omega} \mathbf{B}^{\mathbf{v}^{\mathrm{T}}}\mathbf{C}\mathbf{B}^{\mathbf{v}}\,\mathrm{d}\Omega, \\ \mathbf{K}^{\phi\phi} &= -\frac{\partial\mathbf{R}^{\phi}}{\partial\boldsymbol{\phi}} = \int_{\Omega} \left\{ l^2\mathbf{B}^{\phi^{\mathrm{T}}}\mathbf{B}^{\phi} + \left[1+\mathcal{H}\right]\mathbf{N}^{\phi}\mathbf{N}^{\phi} \right\} \mathrm{d}\Omega, \end{aligned} \tag{3.8}$$

where **C** is the degraded tangent material matrix.

3.1.4. Staggered solution scheme

The finite element model can be then written as follows

$$\begin{bmatrix} \mathbf{v} \\ \boldsymbol{\phi} \end{bmatrix}_n = \begin{bmatrix} \mathbf{v} \\ \boldsymbol{\phi} \end{bmatrix}_{n-1} + \begin{bmatrix} \mathbf{K}^{\mathbf{vv}} & 0 \\ 0 & \mathbf{K}^{\phi\phi} \end{bmatrix}^{-1} \cdot \begin{bmatrix} \mathbf{R}^{\mathbf{v}} \\ \mathbf{R}^{\phi} \end{bmatrix}. \tag{3.9}$$

Note that the decoupled equation system (3.9) corresponds to the staggered algorithmic approach, also known as alternative minimization approach. The monolithic approach [71] could be introduced by including non-zero matrices $\mathbf{K}^{\mathbf{v}\phi} = -\frac{\partial \mathbf{R}^{\mathbf{v}}}{\partial \boldsymbol{\phi}}$ and $\mathbf{K}^{\phi\mathbf{v}} = -\frac{\partial \mathbf{R}^{\phi}}{\partial \mathbf{v}}$ to the off diagonal elements in (3.9), which would require simultaneous calculation of both $\mathbf{v}$ and $\boldsymbol{\phi}$ fields. However, as previously mentioned in the Introduction, such numerical treatment of this problem leads to the numerical instabilities and is therefore not used in this thesis.

The general idea is to iteratively solve the decoupled system at time t_n and the iteration *kk* by first calculating one field using the other field solution computed at the iteration $kk-1$. Then, the obtained estimated solution is used to solve the other field at the iteration *kk*. The solution sequence is arbitrary. Box 3.1 schematically presents the staggered approach where the field $\boldsymbol{\phi}$ is set to be calculated first.

Box 3.1. General staggered solution scheme

```
while φ_n^kk ≉ φ_n^kk-1  and  v_n^kk ≉ v_n^kk-1 :
      solve  φ_n^kk  with  v_n^kk-1
      solve  v_n^kk  with  φ_n^kk
```

The efficiency and convergence rate of such staggered system depends on the stopping criterion, which usually differs between the implementations as discussed in Introduction. Herein, the residual norm-based stopping criterion is presented. It governs the iterative process by controlling the residuals corresponding to the fields $\mathbf{v}$ and $\boldsymbol{\phi}$, as presented in Box 3.2. where "**tol**" is a required user-defined tolerance.

Box 3.2. Residual control (RCTRL) staggered solution scheme

enter iteration kk at time t_n

(with $\boldsymbol{\phi}_n^{kk-1}$ and $\mathbf{v}_n^{kk-1}$ from iteration $kk-1$):

solve $\boldsymbol{\phi}_n^{kk}$ with $\mathbf{v}_n^{kk-1}$

solve $\mathbf{v}_n^{kk}$ with $\boldsymbol{\phi}_n^{kk}$

if $\left\| \begin{matrix} \mathbf{R}^{\mathrm{v}}\left(\boldsymbol{\phi}_n^{kk}, \mathbf{v}_n^{kk}\right) \\ \mathbf{R}^{\phi}\left(\boldsymbol{\phi}_n^{kk}, \mathbf{v}_n^{kk}\right) \end{matrix} \right\| \leq \mathrm{tol}$ continue to t_{n+1}

On the other hand, the single iteration (SI) staggered algorithm, proposed in Miehe et al. [72] solves one field at time t_n with the quantities corresponding to other field calculated at time t_{n-1}. The other field is then updated with the obtained solution. Therefore, it does not contain a stopping criterion and is widely used due to its implementation simplicity and stability advantage over monolithic algorithms.

This SI algorithm is shown in Box 3.3.

Box 3.3. Single iteration (SI) staggered solution scheme

enter at time t_n

(with $\boldsymbol{\phi}_{n-1}$ and $\mathbf{v}_{n-1}$ known):

solve $\boldsymbol{\phi}_n$ with $\mathbf{v}_{n-1}$

solve $\mathbf{v}_n$ with $\boldsymbol{\phi}_n$

continue to t_{n+1}

It is obvious that small time increments Δt are needed for accurate solution in SI algorithm. In this work, SI and RCTRL algorithms are implemented in ABAQUS software.

3.2. ABAQUS implementation

Until the implementation of the RCTRL algorithm presented in author's work [132], no ABAQUS implementation of phase-field fracture model had a stopping criterion which would allow the solver to iterate within the current time increment. Then-existing implementations were based either on the SI staggered [127, 128] or even plain monolithic solution scheme [146]. Thus, the implementation of such algorithm bore an implementation novelty also emphasizing the importance of stopping criterion use.

To implement RCTRL scheme (Box 3.2) into the ABAQUS software, a three-layered system was used combining user elements and appropriate ABAQUS/standard finite elements through UEL and UMAT user subroutines. Moreover, a system of even-odd iterations was employed to correctly impose the equation system decoupling. In this thesis, 1D truss, 2D linear quadrilateral and 3D linear brick elements with full integration are used, corresponding to the ABAQUS element names T3D2, CPE4 and C3D8, respectively. As mentioned above, the incorporation of different elements, e.g., triangular or tetrahedral, is simple and straightforward by substituting the corresponding **N** and **B** matrices.

All information required for the analysis is contained within two files; a .for file containing the FORTRAN code of the algorithm in terms of UEL and UMAT subroutines, and the .inp file which contains the model geometry, nodal connectivity, boundary conditions, material parameters and other analysis options.

3.2.1. Even-odd iteration split

The theoretical RCTRL algorithm shown in Box 3.2 with the iteration *kk* is split into two iterations, $k-1$ and *k*, where *k* is an odd numbered iteration. Such even-odd iteration split allows the calculation of one field per each iteration, with the other one held constant, i.e. $\Delta\mathbf{v}_n^k = 0$ and $\Delta\boldsymbol{\phi}_n^{k-1} = 0$, by setting the phase-field residual $\left(\mathbf{R}^{\phi}\right)^{k-2} = 0$ in the odd iteration. The estimated solution of the previous iteration is obtained at the start of the next iteration, or at the start of the next increment if the solution has converged. The iteration count starts with zero so the first iteration in every increment is always even numbered $(k-1)$. The residual check is always done on the odd iteration number (k). The sequence of field solutions follows Box 3.2, i.e., first the phase-field $\boldsymbol{\phi}_n^k \neq \boldsymbol{\phi}_n^{k-1}$ is obtained after an even $(k-1)$ iteration as

$$\boldsymbol{\phi}_n^k = \boldsymbol{\phi}_n^{k-1} + \Delta\boldsymbol{\phi}_n^k = \boldsymbol{\phi}_n^{k-1} + \mathbf{K}^{\phi\phi}\left(\mathbf{v}_n^{k-2}, \boldsymbol{\phi}_n^{k-1}\right)^{-1} \cdot \mathbf{R}^{\phi}\left(\mathbf{v}_n^{k-2}, \boldsymbol{\phi}_n^{k-1}\right), \tag{3.10}$$

where $\boldsymbol{\phi}_n^{k-1} = \boldsymbol{\phi}_n^{k-2} + \Delta\boldsymbol{\phi}_n^{k-1} = \boldsymbol{\phi}_n^{k-2}$ because phase-field residual in previous odd iteration was set to zero, i.e., $\left(\mathbf{R}^{\phi}\right)^{k-2} = 0$.*

* $\mathbf{R}^{\phi}\left(\mathbf{v}_n^{k-2}, \boldsymbol{\phi}_n^{k-1}\right)$ is not the same as $\left(\mathbf{R}^{\phi}\right)^{k-2}$ because the solution $\mathbf{v}_n^{k-2}$ is not available to the first layer elements at iteration $(k-2)$.

It is then followed by the displacement field $\mathbf{v}_n^{k+1}$ obtained after the calculation in odd iteration (k) as

$$\mathbf{v}_n^{k+1} = \mathbf{v}_n^k + \Delta\mathbf{v}_n^{k+1} = \mathbf{v}_n^k + \mathbf{K}^{\mathrm{vv}}\left(\mathbf{v}_n^k, \boldsymbol{\phi}_n^k\right)^{-1} \cdot \mathbf{R}^{\mathrm{v}}\left(\mathbf{v}_n^k, \boldsymbol{\phi}_n^k\right), \tag{3.11}$$

where $\mathbf{v}_n^k = \mathbf{v}_n^{k-1} + \Delta\mathbf{v}_n^k = \mathbf{v}_n^{k-1}$. At the odd iteration ($k$) the convergence criterion $\left\|\mathbf{R}^{\mathrm{total}}\left(\mathbf{v}_n^k, \boldsymbol{\phi}_n^k\right)\right\| < \mathrm{tol}$ is checked, where $\left\|\mathbf{R}^{\mathrm{total}}\left(\mathbf{v}_n^k, \boldsymbol{\phi}_n^k\right)\right\|$ is the total residual norm obtained as

$$\left\|\mathbf{R}^{\mathrm{total}}\left(\mathbf{v}_n^k, \boldsymbol{\phi}_n^k\right)\right\| = \left\|\mathbf{R}^{\mathrm{v}}\left(\mathbf{v}_n^k, \boldsymbol{\phi}_n^k\right)\right\| + \left\|\mathbf{R}^{\phi}\left(\mathbf{v}_n^k, \boldsymbol{\phi}_n^k\right)\right\| \tag{3.12}$$

If the convergence of each field with the last solution estimates $\left(\mathbf{v}_n^k, \boldsymbol{\phi}_n^k\right)$ is satisfied, a new increment $n+1$ can start with $\boldsymbol{\phi}_{n+1}^0 = \boldsymbol{\phi}_n^k$ and $\mathbf{v}_{n+1}^0 = \mathbf{v}_n^{k+1}$. Note that in order for (3.12) to satisfy convergence criterion, residual vectors corresponding to each field have to satisfy the convergence criterion. Therefore, when $\mathbf{R}^{\mathrm{v}}\left(\mathbf{v}_n^k, \boldsymbol{\phi}_n^k\right) < \mathrm{tol}$, equation (3.11) states that $\mathbf{v}_n^{k+1} \simeq \mathbf{v}_n^k$, and instead of the new odd iteration $(k+1)$, the new increment is started if $\mathbf{R}^{\phi}\left(\mathbf{v}_n^k, \boldsymbol{\phi}_n^k\right) < \mathrm{tol}$. The algorithm is schematically shown in the flowchart in Fig. 3.1.

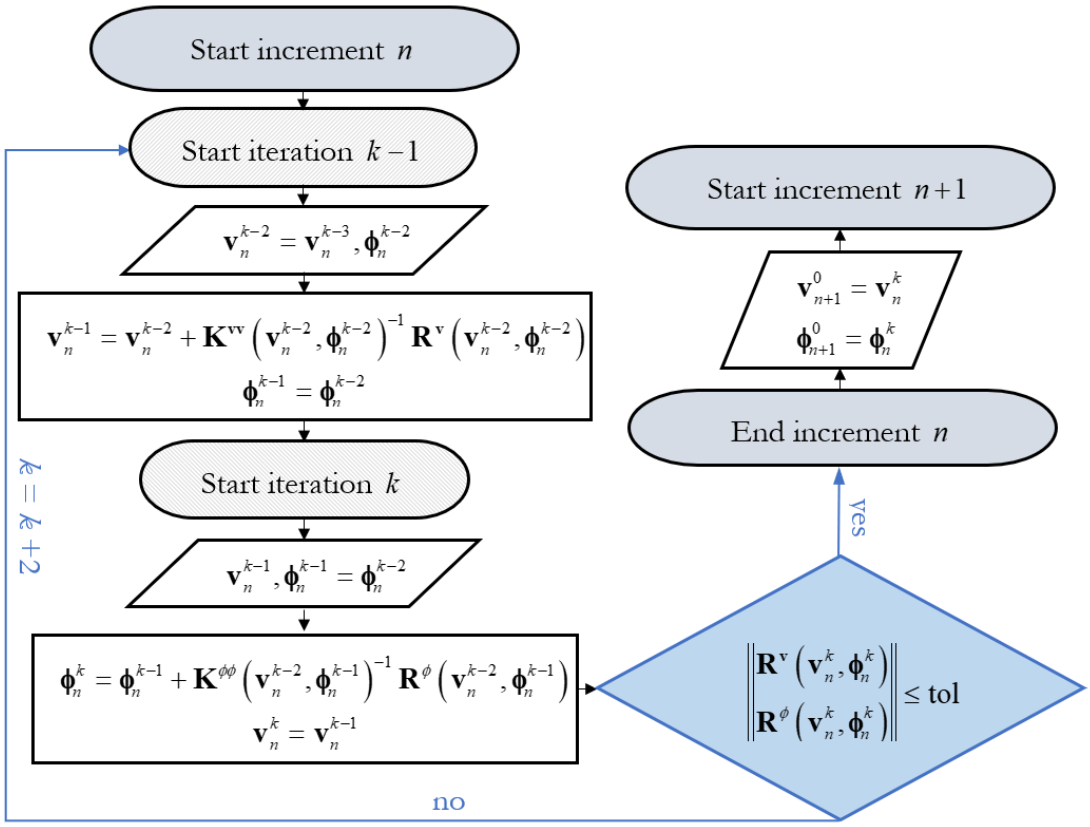

Fig. 3.1. Flowchart of RCTRL algorithm with the even-odd iteration split

3.2.2. Three-layered system

The main equation system calculations, (3.10) and (3.11), are done in a two-layered manner. The layered system means that the FE mesh discretizing the numerical model is made out of multiple FE mesh layers. The finite elements are stacked on top of each other, thus retaining the same nodal connectivity. The FE calculations are then completely decoupled. The phase-field evolution calculation is set at the first layer level and is facilitated by a user element created via the UEL subroutine. There is no calculation of residual vector $\mathbf{R}^{\phi}$ nor stiffness matrix $\mathbf{K}^{\phi\phi}$ at the odd iteration (*k*). The residual vector $\mathbf{R}^{\phi}$ at the odd iteration (*k*) is set to zero while stiffness matrix $\mathbf{K}^{\phi\phi}$ is a diagonal identity matrix, thus speeding up the calculations. The displacement field calculation is placed at the second layer level and imposed via the UMAT subroutine. The ABAQUS/Standard finite elements are used at this level. They are generally well optimized and allow very simple utilization of many additional options typically found in commercial FE software. Moreover, it efficiently utilizes ABAQUS postprocessing module allowing quick visualisation of the obtained results, making it very user friendly.

Note that the residual $\mathbf{R}^{\mathbf{v}}\left(\mathbf{v}_n^k, \boldsymbol{\phi}_n^k\right)$ is being calculated at the second layer level, while $\mathbf{R}^{\phi}\left(\mathbf{v}_n^{k-2}, \boldsymbol{\phi}_n^k\right)$ is calculated at the first layer level, since the first layer elements cannot get the updated displacement solution estimate for the current iteration. Therefore, the residual calculation $\mathbf{R}^{\phi}\left(\mathbf{v}_n^k, \boldsymbol{\phi}_n^k\right)$ is added to the third layer at the odd iteration $\left(k\right)$. The addition of the third layer is thus is necessary to implement the residual check. The algorithm convergence after the even iteration $\left(k-1\right)$ is restricted by setting $\mathbf{R}^{\phi} = \text{const} \gg \text{tol}$ at the third layer level, while the history field $\mathcal{H}\left(\mathbf{v}_n^k\right)$ is calculated at odd iteration (*k*). The stiffness matrix at the third layer is not calculated, greatly saving the CPU time. The three-layered system is schematically presented in Fig. 3.2.

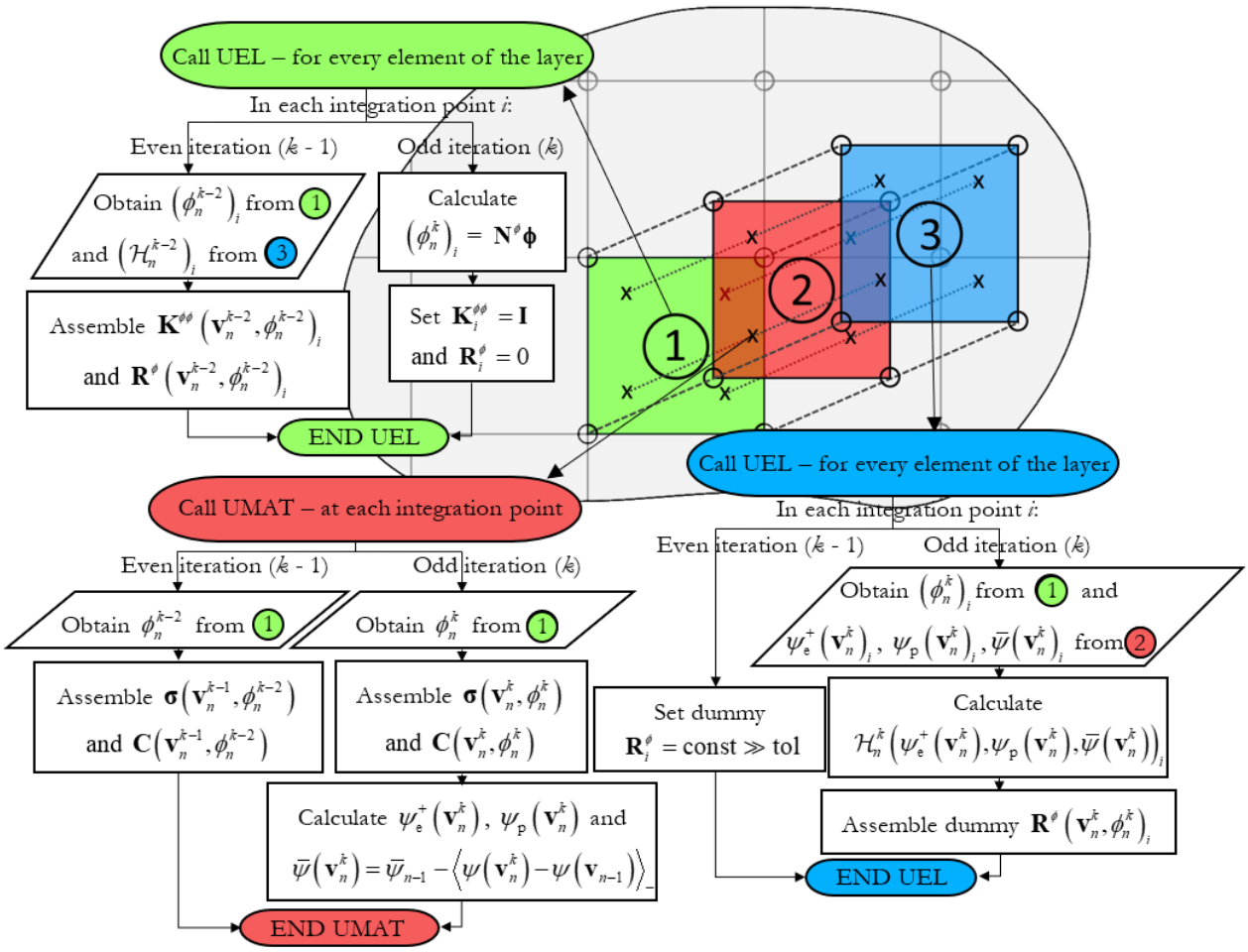

Fig. 3.2. ABAQUS implementation of the three-layered system

3.2.3. Residual vector normalization and DOF convention

The residual vectors corresponding to the phase-field and displacement field are completely separated using proper ABAQUS's DOF convention. The first- and third-layer calculations, corresponding to the phase-field evolution, are performed on rotational DOFs not used by the second-layer elements. That way, the residual vectors can be normed separately. This is highly important as the displacements can have very different magnitudes while the phase-field is bounded, $\phi \in [0,1]$. Moreover, the DOFs of first and third layer are further separated so the calculation of $\mathbf{R}^{\phi}$ in the third layer cannot affect the real solution estimate at the first layer. The employed DOFs following the ABAQUS DOF convention are shown in Table 3.1.

Table 3.1. Degrees of freedom used in the three-layered system

Physical degrees of freedom	ABAQUS DOF convention
u, *v*, *w* (displacements in *x*,*y*,*z* direction)	1, 2, 3 (displacements in *x*,*y*,*z* direction)
ϕ (phase-field parameter)	4 (*x*-axis rotation)
dummy DOF	5 (*y*-axis rotation)

Furthermore, such DOF separation together with the even-odd iteration split allows the efficient utilization of ABAQUS advanced convergence control. The convergence tolerance "**tol**" is used as default ABAQUS tolerance which controls the ratio of the largest local residual to the corresponding field-averaged residual value. By default, this ratio is set to 5×10^{-3} which is, as mentioned in the ABAQUS documentation [145], "rather strict by engineering standards but in all but exceptional cases will guarantee an accurate solution to complex nonlinear problems". This criterion could also be relaxed to increase the computational speed. Moreover, the convergence criterion can be set to some fixed value to which the largest residual is then compared (e.g. $\mathbf{tol} = 1\times10^{-5}$ was used in author's work [132]).

3.2.4. Visualization and layer intercommunication

As presented in Fig. 3.2, elements exchange variable values between the layers. For example, the variable ϕ has to be sent from an integration point of an element in the first layer to the corresponding integration points of the elements belonging to the second and third layer. Similarly, energetic variables ψ_{e}^{+}, ψ_{p} and $\bar{\psi}$ have to be sent to the corresponding integration point in the third layer, etc. This is done via ABAQUS COMMON BLOCK array, allowing the variable transfer between the user subroutines.

The visualization is conveniently done using the ABAQUS/Standard elements contained in the second layer. The stresses, strains, reaction forces, displacements and energy densities can be visualized in the same way as in the standard ABAQUS analyses, which makes this implementation exceptionally user-friendly. Energy densities ψ_{e}^{+} and ψ_{p} are efficiently contained in the ABAQUS preset arrays, SENER and PENER. Other variables, such as ϕ, $\varepsilon_{\mathrm{eqv}}^{\mathrm{p}}$, $\boldsymbol{\varepsilon}^{\mathrm{p}}$, $\boldsymbol{\alpha}_k$, or STATUS variable required in element deletion option, are visualized through

the SDV (solution dependent variable) array. As can be seen from Fig. 3.1 and Fig. 3.2, the second-layer elements have the access to the current iteration solution estimates $\mathbf{v}_n^k$ and $\boldsymbol{\phi}_n^k$ at the odd iteration (*k*), thus allowing the visualization of correct values upon increment convergence. The number of SDVs is regulated within .inp file by *DEPVAR keyword.

3.3. Additional options

Some useful additional options available within this implementation are explored here, showing the great advantages of commercial FE software implementation.

3.3.1. Automatic incrementation

ABAQUS automatic loading incrementation can be easily introduced via *CONTROLS, PARAMETERS=TIME INCREMENTATION keyword. If the iteration number needed for the solution convergence in the current increment exceeds some user set iteration count value I_{L}, the size of the following increment is reduced by the user set cut-back factor $\delta_{\mathrm{B}} \in [0,1]$. Analogously, if the number of iterations in two consecutive increments is lower than the user set value I_{G}, the next increment size will be increased by the factor $\delta_{\mathrm{D}} \in [1,\infty]$. The detailed explanation with exemplary parameters is given in [133].

3.3.2. Element deletion

Element deletion is an option which removes integration points from calculation upon the satisfaction of some condition. Consequently, whole elements can be deleted upon removal of all integration points corresponding to the element. This provides an attractive visualization of fracture, but also speeds up the simulation after the initial fracture. The reason is obvious – the total number of integration point calculations is reduced, combined with the fact that fractured elements tend to have a slower convergence rate than the rest of the domain due to their non-linear behaviour.

The option is easily activated via the keyword *DEPVAR, DELETE = number, where the number corresponds to the SDV array element at which the STATUS variable is saved. The variable is calculated within the UMAT subroutine, and takes value 0 or 1, where 0 activates the element deletion.

3.3.3. Thread parallelization

The presented implementation can be partially parallelized allowing the simulation to be run on multiple processors. It is only partial because the sequence of element level calculations has to remain unchanged. At this moment, this is achievable by using a single thread to run through all the elements and create respective **R** and **K** arrays. The array assembly and the consequent equation system calculation can then be run on multiple processors, thus significantly accelerating the simulation.

The option is enabled upon the analysis execution by including the keywords `standard_parallel=solver` and `CPUS=`*`n`*, where *n* is the number of processor threads to be used.

3.3.4. Contact

Since the second layer containing the displacement DOFs uses ABAQUS/standard elements, the complete ABAQUS capability to model contact between the two bodies can be easily utilized. The examples containing contact between multiple bodies in phase-field fracture analysis are presented in Chapter 5.

3.3.5. Different solvers

As explained, the presented implementation is accomplished only via the displacement and rotation DOFs. This allows the use of *STATIC, GENERAL ABAQUS step option employing the Newton-Raphson solver, as well as *STATIC, RIKS allowing the use of arc-length method, thus enabling the use of both displacement- and force-controlled loads as boundary conditions.

3.3.6. Restart analyses

The restart option can be very useful for long duration analyses. The files required to restart the analysis are written after the user-defined number of increments or at user-defined time frequency. The analysis interrupted due to various reasons, such as a computer malfunction, could be restarted, or the completed analysis could be continued appending the load history with new steps. Moreover, the analysis could be restarted from an intermediate point with a somewhat modified remaining load history data.

3.3.7. Finite elements with incompatible modes or hybrid elements for incompressible material behaviour

If required, special finite elements can be used without interference at the second layer level.

3.3.8. Additional extensions – finite strain settings

The presented implementation framework is also suitable for an extension to finite strains settings. The displacement layer (second layer) is already coded in the manner appropriate to these settings, taking the full advantage of ABAQUS arrays and auxiliary routines. It can be included by setting the keyword *NLGEOM=YES in the *STEP definition. Coding changes have to be done only on Layer 1 and 3 to correctly calculate the updated Jacobian matrix. However, this extension is out of the scope of this thesis and has been left for the future research.

3.4. Cycle skipping option for high-cyclic fatigue analysis

The phase-field fracture model with the extension to fatigue, as presented in Section 2.3, is based on the time evolving properties. To properly calculate the fracture nucleation, stabilised propagation and final rapid growth, one should precisely compute every cycle in the analysis. However, such approach is exceedingly time-consuming for the analysis of high-cycle fatigue regime even for medium size problems.

However, this type of analysis can be firstly accelerated by noting that the presented generalized phase-field framework is derived on the basis of TH phase-field model, which recovers linear material behaviour stage at the start of high-cyclic fatigue analysis. In that case, the elastic energy density amplitude $\Delta\psi_{\mathrm{e}}^{+}$ is constant. The energy density accumulation variable $\bar{\psi}$ then grows linearly until fatigue degradation function $\hat{F}\left(\bar{\psi}\right)$ reaches the point where $\hat{F}\left(\bar{\psi}\right)\cdot\psi_{\mathrm{c}} < \psi_{\mathrm{e}}^{+}$, thus triggering the onset of damage $\mathcal{H} > 0$. This linear part can thus be accurately skipped by calculating the cycle at which that will happen.

The subsequent non-linear part of the analysis can be further accelerated the utilization of the cycle skipping technique, based on the idea proposed by Cojocaru and Karlsson [165] for the FE simulations of structures subjected to cyclic loading. It will be explained here in short. The cycle skipping technique [165] is based on performing a complete FE analysis for a set of

cycles establishing a trend line, extrapolating the solution variables over a controlled number of cycles, and using the extrapolated state as an initial state for FE analysis of next set of cycles as presented in Fig. 3.3. The extrapolation is done on the set of selected variables $\mathbf{y} = \mathbf{y}(t, ip)$, where *ip* represents the integration point. At least three consecutive cycle data values have to be defined by points $\mathrm{P}_1(t_1, y_1), \mathrm{P}_2(t_2, y_2)$ and $\mathrm{P}_3(t_3, y_3)$. The cycle skipping technique is schematically presented in Fig. 3.3., where s_{12} and s_{23} represent the discrete slopes of function $y(t)$.

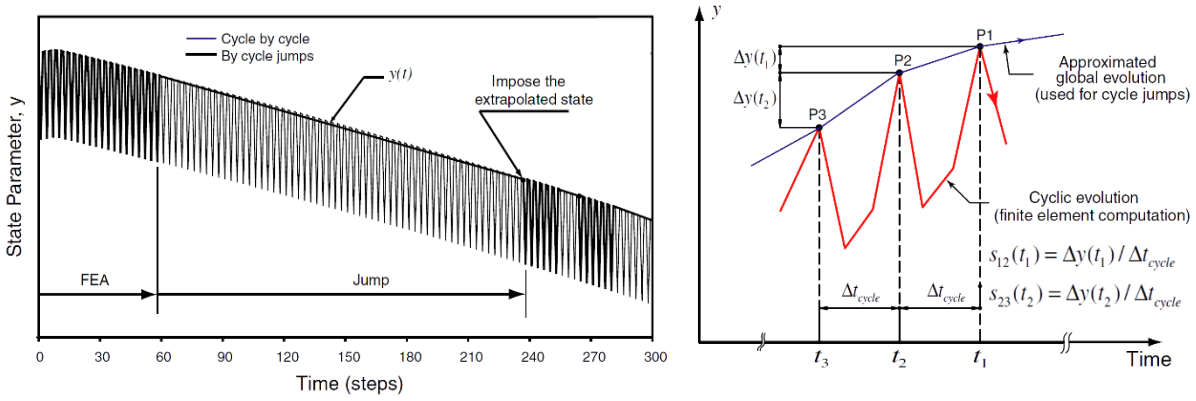

Fig. 3.3. Schematic representation cycle skipping technique [165]

The number of cycles to skip Δt_{jump} is determined through a control function based on the user-input allowed relative error q_{y} as

$$\frac{\left|s_{\mathrm{p}}\left(t_1 + \Delta t^{ip}_{y,\mathrm{jump}}\right) - s_{12}\left(t_1\right)\right|}{\left|s_{12}\left(t_1\right)\right|} \le q_{\mathrm{y}}, \tag{3.13}$$

where $s_{\mathrm{p}}\left(t_1 + \Delta t^{ip}_{y,\mathrm{jump}}\right)$ is the predicted, linearly extrapolated slope moment after the jump obtained as

$$s_{\mathrm{p}}\left(t_1 + \Delta t^{ip}_{y,\mathrm{jump}}\right) = s_{12}\left(t_1\right) + \frac{s_{12}\left(t_1\right) - s_{23}\left(t_2\right)}{\Delta t_{\mathrm{cycle}}} \Delta t^{ip}_{y,\mathrm{jump}}. \tag{3.14}$$

The allowed jump value for each variable is then computed as

$$\Delta t^{ip}_{y,\mathrm{jump}} = q_{\mathrm{y}} \Delta t_{\mathrm{cycle}} \frac{\left|s_{12}\left(t_1\right)\right|}{\left|s_{12}\left(t_1\right) - s_{23}\left(t_2\right)\right|}, \tag{3.15}$$

while the final cycle jump is computed as the minimum allowed jump for all variables

$$\Delta t_{\text{jump}} = \Delta t_{\text{cycle}} \left[\min \left\{ \Delta t_{y,\text{jump}}^{ip} \right\} \Big/ \Delta t_{\text{cycle}} \right]. \tag{3.16}$$

Finally, the value of the extrapolated function $y\left(t_1 + \Delta t_{\text{jump}}\right)$ after the jump is calculated as

$$y\left(t_1 + \Delta t_{\text{jump}}\right) = y\left(t_1\right) + \mathrm{s}_{12}\left(t_1\right)\Delta t_{\text{jump}} + \left[\mathrm{s}_{12}\left(t_1\right) - \mathrm{s}_{23}\left(t_2\right)\right]\frac{\left(\Delta t_{\text{jump}}\right)^2}{2\Delta t_{\text{cycle}}}. \tag{3.17}$$

The extrapolation method is usually most suited for quasi-linearly evolving systems. However, the employment of control function enables it to accurately solve the highly non-linear time evolving behaviour by automatically calculating lower number of cycles to skip or no cycle skip at all.

3.4.1. Cycle skip implementation

The initial cycle skip and the presented cycle skipping technique are implemented through UEXTERNALDB user subroutine which is called after each successful increment. For the initial cycle skip, the integration point with highest $\Delta\psi_{\mathrm{e}}^{+}$ value after the first cycle is found and used to calculate the first cycle number at which $\mathcal{H} > 0$ occurs. The energy density accumulation variable $\bar{\psi}$ is then linearly extrapolated at the start of the next cycle thus effectively skipping the calculation of the linear stage.

For the subsequent stage, the energy density accumulation variable $\bar{\psi}$ is selected for the considered set **y**. Its value in each integration point of the model is accessed by the UEXTERNALDB user subroutine via the already existing COMMON BLOCK array, at the end of each cycle for three consecutive cycles. The cycle jump Δt_{jump} is then automatically calculated by expression (3.16). Note that for the highly non-linear part of the simulation, there might be no cycle skipping and the analysis advances as usual. At the beginning of next computed cycle, the extrapolated energy density accumulation variable is then easily calculated following (3.17). The cycle time length Δt_{cycle} is held constant, thus simplifying the equations above.

Chapter 4

Homogeneous material numerical examples

Summary

In this chapter, the proposed generalized phase-field fracture model implementation within FE ABAQUS software, based on the RCTRL algorithm, is tested on different numerical examples under the assumption of homogeneous material behaviour. The chapter is divided into three subsections according to the underlaying material behaviour and loading conditions, as schematically presented in Fig. 4.1.

The first subsection closely follows the examples published in author's previous work [132]. The algorithm performance is tested on standard numerical benchmark tests and compared to the widely used SI algorithm in terms of accuracy and computational speed. The SI algorithm has also been implemented in ABAQUS for the direct comparison. Brittle material behaviour with monotonic loading is assumed in this section. Energy decompositions presented in Section 2.1.4. are thoroughly tested as well. The standard AT-2 framework (2.14) is used throughout

this subsection, unless stated otherwise. The algorithm version has been updated since the publishing of [132] and some results are thus revised and expanded. The proposed implementation in combination with the arc-length solver is tested on the force-controlled problems, while the Newton-Raphson solver is standardly used in displacement-controlled problems. The thread parallelization option is thoroughly tested. The testing of the phase field fracture algorithm on brittle material behaviour examples is concluded with qualitative validation tests comparing the crack paths with the numerical and experimental data available in literature. The importance of stopping criterion within the staggered phase-field algorithm is emphasised on the example of arbitrary porous steel microstructure.

Following the extensions presented in Chapter 2, the implementation's ability to model ductile material behaviour is tested on different numerical examples in comparison with numerical results and experimental measurements from literature. The element deletion option is presented here. The algorithm performance is also tested on 3D examples and the round-robin Sandia Lab Challenge series. To completely recover linear elastic behaviour stage, the proposed generalized phase-field fracture framework with the TH model is used throughout this subsection. The parameter ζ is set to 1, unless stated otherwise.

Finally, the proposed generalized phase-field fracture model is tested on the cyclically loaded examples. The ability of the novel generalized phase-field fracture framework to retrieve well-known features of material fatigue is presented. The $\varepsilon - N$ curve, i.e., the amplitude magnitude versus cycles-to-failure, and its transition from the low- to high-cyclic regime is clearly presented on simple homogeneous example. The ability to compute the crack nucleation, stable evolution and rapid propagation stages are tested on the Compact Tension (CT) specimens in comparison with experimental measurements. Moreover, effect of different material properties on the Paris law and the $\varepsilon - N$ curves has been studied parametrically on an academic elastic material in the high-cyclic fatigue regime. The TH model is used throughout this subsection as well.

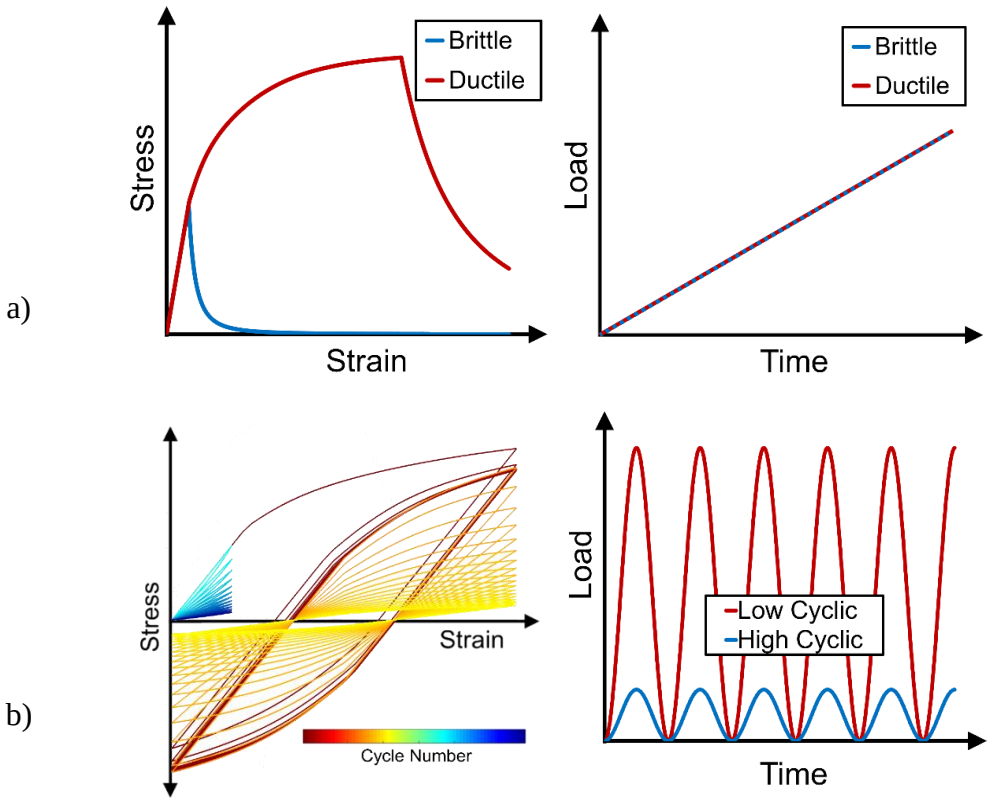

Fig. 4.1. Schematic representation of material response obtainable by generalized phase-field fracture model for a) monotonic (proportional) loading, b) cyclic loading

The detailed discussion on the accuracy and efficiency of the implemented algorithm is given throughout this chapter. The length scale parameter l is always chosen to be at least twice the characteristic size of the finite elements used in the vicinity of expected crack, in accordance with Miehe et al. [71]. The standard Newton-Raphson solver is used throughout this chapter in both monotonic and cyclic loading cases, unless stated otherwise. All numerical simulations are performed on an Intel® Xeon® CPU E5-1620 v3 @ 3.50 GHz with 24 GB RAM memory. The CPU time comparisons are performed with single-thread computations. The default ABAQUS convergence criterion is used.

4.1. Monotonic loading - Brittle material behaviour examples

4.1.1. Homogeneous Example

To first assess the accuracy of RCTRL algorithm, a 2D homogeneous plate with dimensions 1×1 mm is considered. The plate is discretized by one 2D element, loaded and constrained as shown in Fig. 4.2. The analytical solution for the setup is known, as presented in (2.31). SI algorithm is used for comparison. The following material properties are chosen: the Young's

modulus $E = 210$ GPa, the Poisson's ratio $\nu = 0.3$ and the critical fracture energy density $G_c = 2.7 \times 10^{-3}$ kN/mm. The length scale parameter is set to $l = 2$ mm.

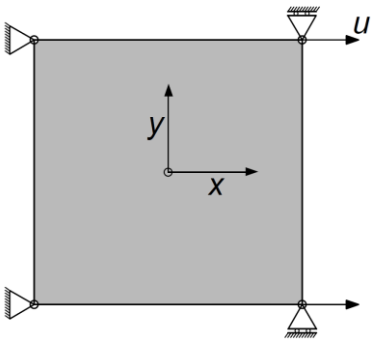

Fig. 4.2. Geometry and boundary conditions of the homogeneous plate subjected to tension

The example is solved with 5 different loading increment sizes Δu to reach $u = 0.02$ mm, namely $\Delta u = 1 \times 10^{-3}$ mm, $\Delta u = 5 \times 10^{-4}$ mm, $\Delta u = 1 \times 10^{-4}$ mm, $\Delta u = 5 \times 10^{-5}$ mm and $\Delta u = 1 \times 10^{-5}$ mm. Fig. 4.3. shows the axial stress-strain response comparison of SI and RCTRL algorithms against the analytical solution.

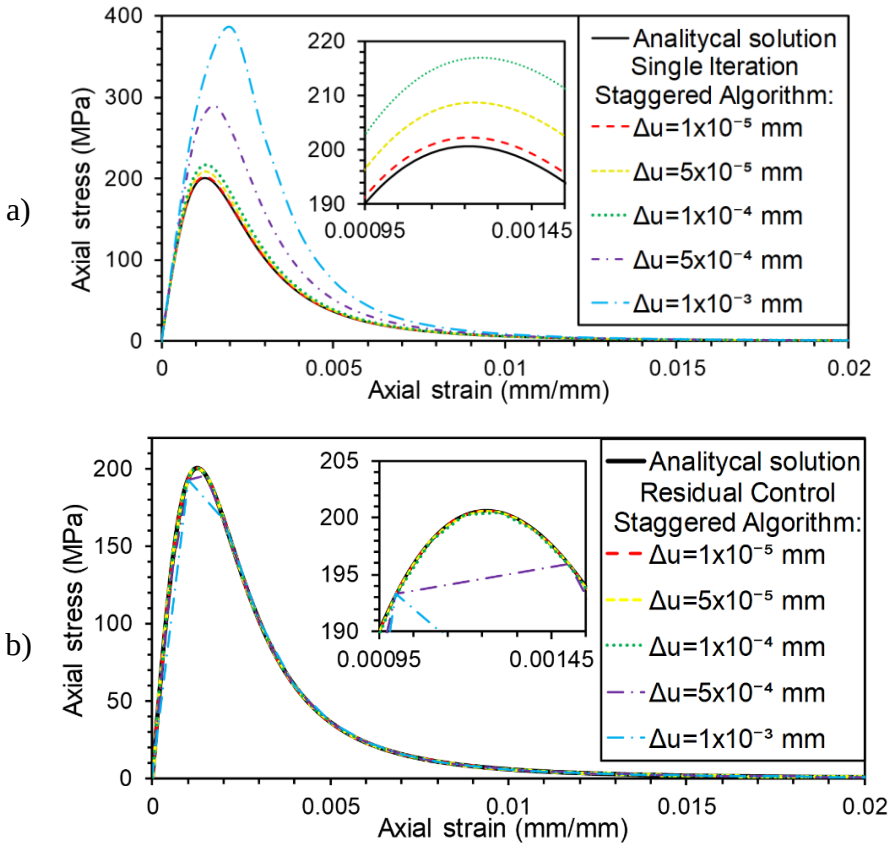

Fig. 4.3. Stress-strain curves obtained by a) SI staggered algorithm and b) RCTRL staggered algorithm in comparison with the analytical solution

Furthermore, the relative stress difference compared to the analytical solution is presented in Fig. 4.4., in the logarithmic scale.

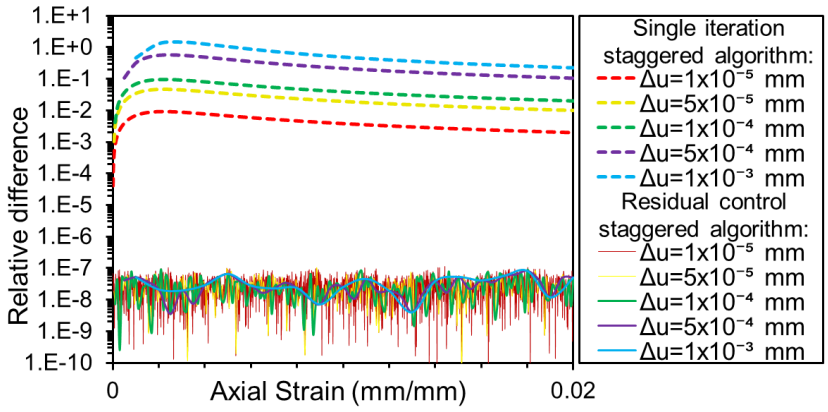

Fig. 4.4. Relative stress difference between SI and RCTRL staggered algorithms in comparison with the analytical solution

The accuracy of SI algorithm is extremely dependent on the size of loading increment as the error increases with the increase in the loading increment. On the other hand, the RCTRL algorithm matches well with the analytical solution even for large loading increments with no increase in relative error. An improvement in the relative error results can be also seen in comparison with the results presented in [132], as the ABAQUS default convergence criterion is obviously more rigorous.

4.1.2. Single edge notched specimen

This is the most common benchmark test used in the verification of the phase-field fracture models. The specimen geometry, shown in Fig. 4.5., and the material properties, $E = 210$ GPa, $\nu = 0.3$ and $G_c = 2.7 \times 10^{-3}$ kN/mm are adopted from Miehe et al. [72]. Length scale parameter $l = 0.0075$ mm is chosen for the direct comparison. Note that the higher value of the parameter l would result in a wider crack band and lower critical force value before the onset of fracture, and vice versa, as studied in [71, 72, 166]. First, the specimen is subjected to tensile loading, where no energy split is required. Afterwards, it is subjected to shear loading, where the proposed algorithm is tested with two strain energy splits presented in Section 2.1.4.

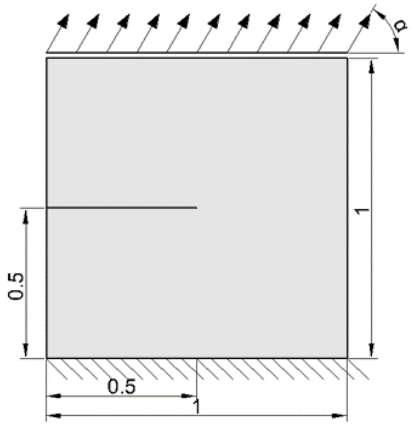

Fig. 4.5. Single edge notched specimen geometry and boundary conditions. α = 90° for tensile test and α = 0° for shear test

4.1.2.1. Tensile test

The prescribed boundary conditions used in this example are shown in Fig. 4.5. with $\alpha = 90°$. The specimen domain is discretized by 18,868 finite elements. The mesh is refined in the region of the expected crack path evolution. The solution is computed by the RCTRL algorithm implementation using $\Delta u = 1\times10^{-5}$ mm loading increment size. In contrast, the SI algorithm solutions are obtained with the loading increment size $\Delta u = 1\times10^{-5}$ mm up to $u = 5\times10^{-3}$ mm, and then 4 different increment sizes up to failure, namely $\Delta u = 1\times10^{-5}$ mm, $\Delta u = 1\times10^{-6}$ mm, $\Delta u = 1\times10^{-7}$ mm and $\Delta u = 1\times10^{-8}$ mm. Fig. 4.6. shows the crack propagation in a single increment, exhibiting pure brittle behaviour. Such behaviour can be obtained with the proposed RCTRL algorithm since no artificial viscosity is added to the model for numerical stabilization, and the crack propagation is not slowed down in any other way, as it is the obvious case in the SI staggered scheme.

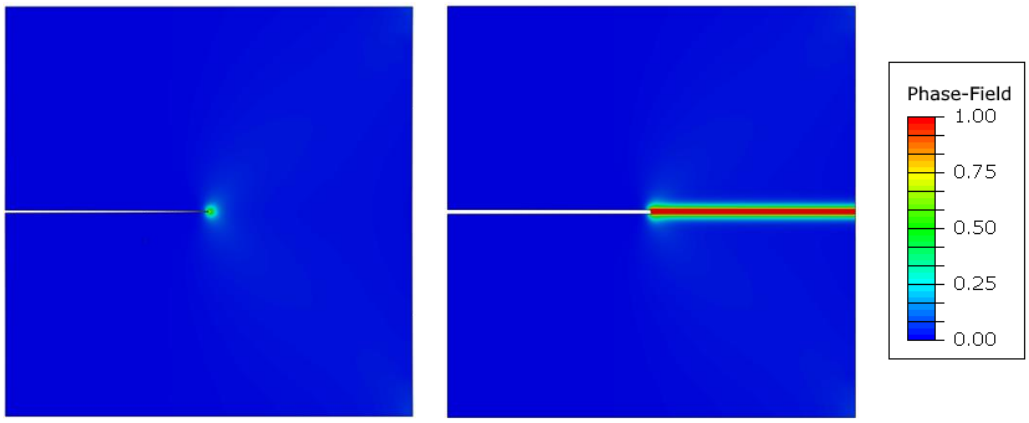

a) b)

Fig. 4.6. Single-edge notched tension test. Crack pattern obtained with the proposed algorithm at displacement a) u = 5.53 × 10^{-3} mm and b) u = 5.54 × 10^{-3} mm

The force-displacement curves in Fig. 4.7. support this claim. Here, the monolithic solution from Miehe et al. [71] is used for the solution verification. The curve of the monolithic solution is not as steep as the proposed algorithm solution because a penalty term, which can be interpreted as an artificial viscous hardening, has been introduced in [71]. The SI algorithm matches the curve of the staggered solution taken from [72] for the same loading increment. Therefore, this proves that SI algorithm used here is, in fact, the algorithm presented in Miehe et al. [72].

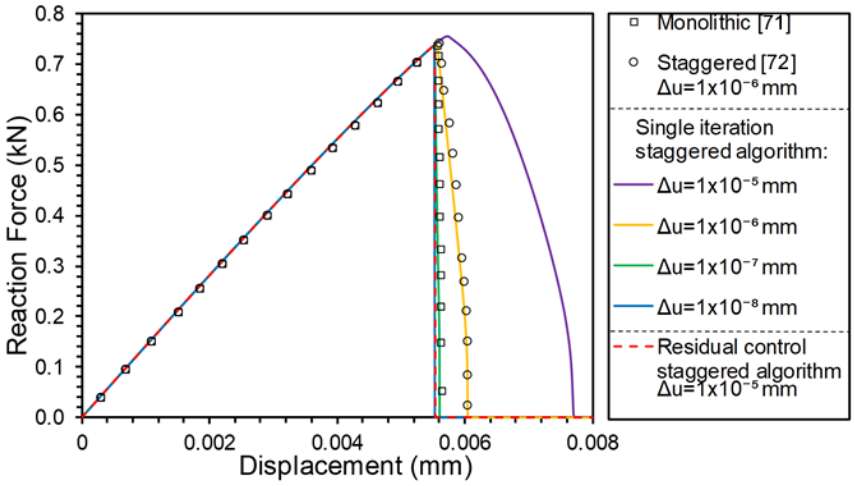

Fig. 4.7. Single-edge notched tension test. Force-displacement curves

Similarly to the homogeneous case, the SI curves converge to the RCTRL algorithm solution with the decrease in loading increment size. However, such precision comes at a cost even that is more pronounced on finer meshes. Table 4.1. presents the CPU time used. The SI staggered algorithm takes much more computational time to solve the problem with similar accuracy, as presented in Fig. 4.7. Note again that all simulations have been run with the same loading step size up to $u = 5\times10^{-3}$. Otherwise, the CPU time difference would be even more pronounced. The CPU time comparison is taken from author's work [132], where slightly more lenient convergence criteria has been used compared to the ABAQUS default convergence criteria used here.

Table 4.1. Single-edge notched tension test. CPU time consumption

Algorithm	SI staggered algorithm				RCTRL staggered algorithm
Loading increment Δu	1×10^{-5} mm	1×10^{-6} mm	1×10^{-7} mm	1×10^{-8} mm	1×10^{-5} mm
CPU time (s)	3,531	14,907	30,915	291,997	14,062

Fig. 4.8. shows the required number of iterations to solve the problem. Note that the shown iteration number count is doubled since even-odd iteration split is employed in this implementation.

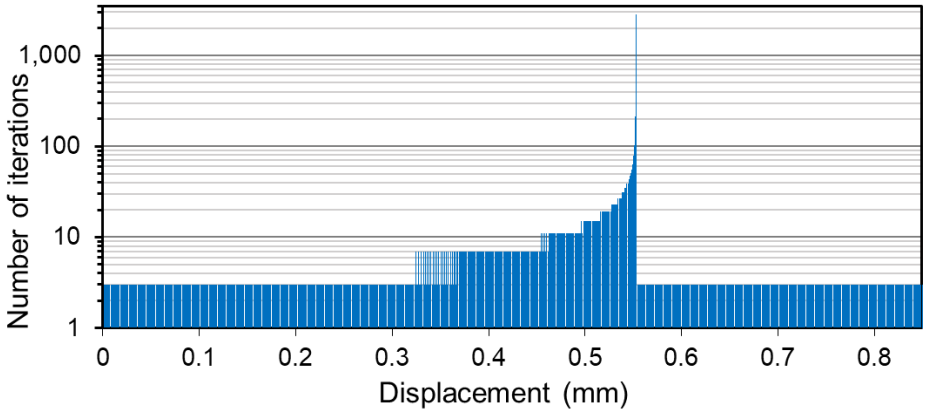

Fig. 4.8. Single-edge notched tension test. Number of iterations used in RCTRL algorithm

Computationally the most demanding increment is the one in which the crack rapidly propagates through the domain. The excessively high iteration count is obtained due to the use of the exaggeratedly large fixed loading increment, for which the SI algorithm obtained inaccurate solution in terms of force-displacement curve. Furthermore, it is also shown that even with such disproportionate settings, the computation is still much faster than SI algorithm using very fine loading increment sizes. In general, the fixed loading incrementation should be avoided for efficiency reasons and replaced with the automatic loading incrementation explained in Section 3.3.1. The reason behind efficiency of the RCTRL algorithm is that the computation of a new iteration is much faster than the computation of a new increment, as done in SI algorithm. The addition of the viscosity term [71] would slow down the crack propagation and ultimately lower the iteration count in the critical increment and the CPU time consumption.

TH (Threshold) Model

Finally, the TH model (2.15) is tested and compared to the previous solutions obtained with standard AT-2 model. Following the homogeneous solution and equation (2.33), the length parameter is increased to $l = 0.0377$ mm. Although the mesh could be much coarser now, for simplicity, it is kept the same. Fig. 4.9. presents the force-displacement curves for the AT-2 and TH models.

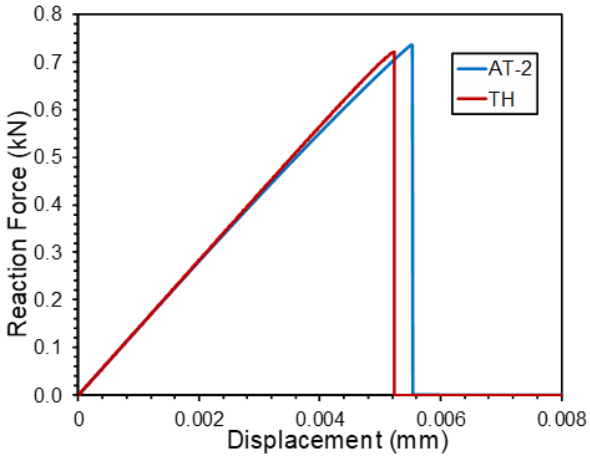

Fig. 4.9. Single-edge notched tension test. Force-displacement curves for TH and AT-2 models

The corresponding curves and maximal load values are very close. It can be seen that the TH model recovers the linear response before the onset of fracture. Moreover, the result obtained with 5 times larger length scale parameter allows the usage of coarse meshes potentially making the simulations much faster.

4.1.2.2. Shear test

Unlike the previous examples, the tensile stress state is not predominant here. Thus, the proper strain energy decomposition is needed to prevent unphysical crack propagation in the compressive stress state. In this example, two energy decompositions described in Chapter 2 are used in combination with the proposed RCTRL algorithm and the SI staggered algorithm with 3 different loading incrementation sizes. The boundary conditions are presented in Fig. 4.5. with $\alpha = 0°$. The mesh consists of 26,914 finite elements and is refined in the expected crack propagation area. Fig. 4.10. shows the crack pattern solution obtained by the proposed algorithm using the spherical-deviatoric and the spectral decomposition.

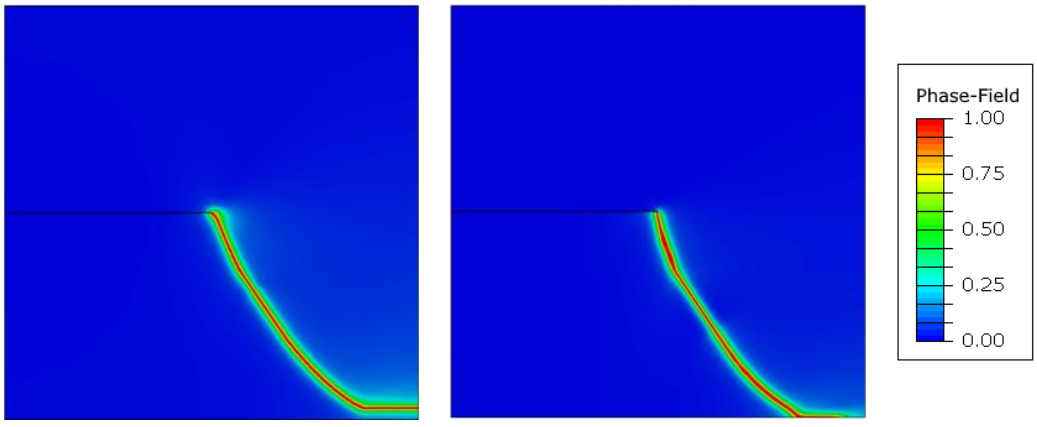

a) b)

Fig. 4.10. Single-edge notched shear test. a) Spherical-deviatoric decomposition, b) spectral decomposition

The force-displacement curves displayed in Fig. 4.11. show the behaviour similar to the previously shown examples, for different loading increment sizes. However, due to the different fracture process, the crack propagation is not so rapid. The difference between the results of the two decompositions is clearly shown.

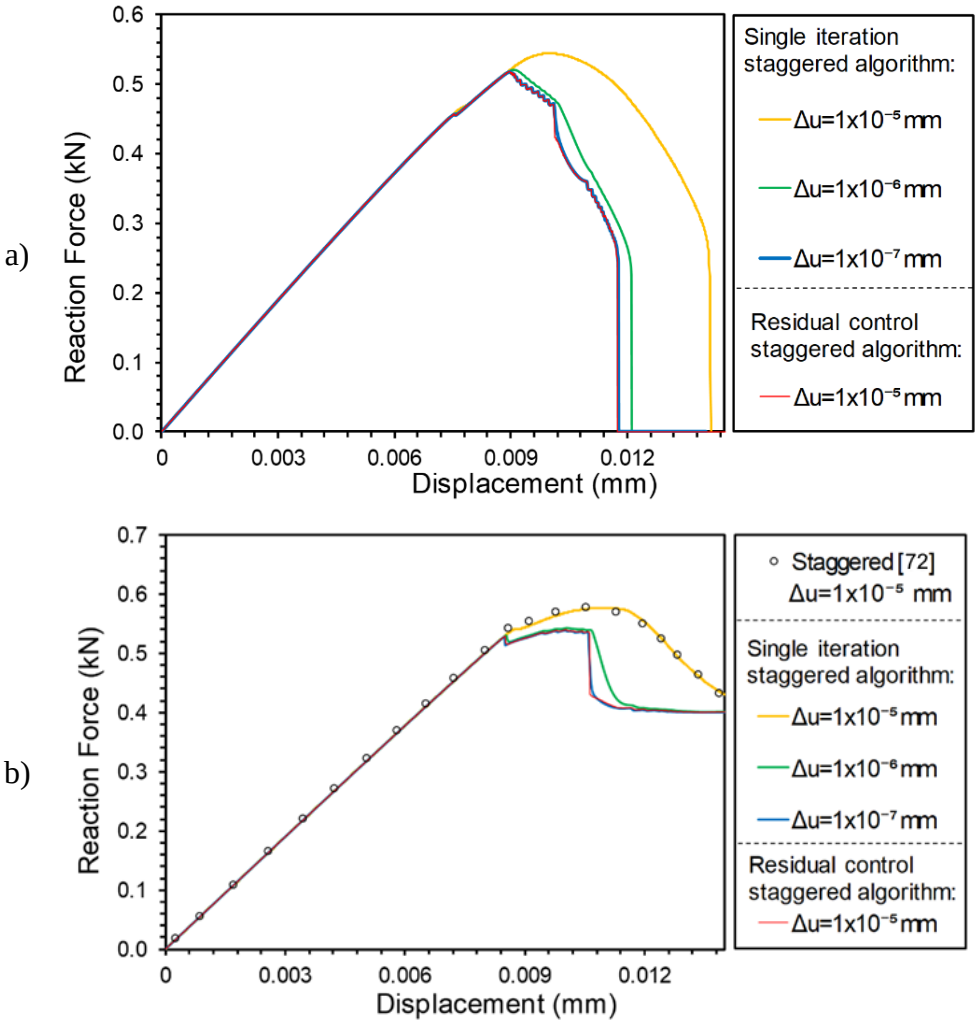

Fig. 4.11. Single-edge notched shear test. Force-displacement curves for a) spherical-deviatoric decomposition, b) spectral decomposition

Unlike the spherical-deviatoric decomposition, the complete force drop is not observed in the results obtained with spectral energy decomposition (Fig. 4.11.b). The reason behind it is the crack propagation to the bottom side of model where displacement boundary condition is set, which does not allow the total separation of model in two parts.

The required CPU time is presented in Table 4.2. The CPU time comparison is again taken from the author's work [132], where more lenient convergence criteria has been used. Note that the spectral decomposition consumes more CPU time than the spherical-deviatoric decomposition, as expected.

Table 4.2. Single notch shear test. CPU time consumption

Algorithm	SI staggered algorithm						RCTRL staggered algorithm	
Loading increment Δu	1×10^{-5} mm		1×10^{-6} mm		1×10^{-7} mm		1×10^{-5} mm	
Decomposition	S-D	Spectr.	S-D	Spectr.	S-D	Spectr.	S-D	Spectr.
CPU time (s)	10,965	14,225	77,446	98,768	751,162	1,239,121	106,258	207,456

The problem with the energy decompositions is the inevitable non-symmetry of the stiffness matrix following the anisotropic system, which significantly slows down the computation. A hybrid formulation proposed in Ambati et al. [79] alleviates that problem by decomposing only the energetic variables, while leaving the stress and stiffness matrix isotropic and thus symmetric.

4.1.3. L-shaped specimen

The crack path evolution is simulated on the concrete L-shaped specimen, experimentally tested in Winkler et al. [167]. The geometry and boundary conditions are displayed in Fig. 4.12. The material properties are taken as $E = 25.85$ GPa, $\nu = 0.18$ and $G_c = 8.9\times10^{-5}$ kN/mm. The length scale parameter is set to $l = 1.1875$ mm according to Ambati et al. [79]. Considerably higher values of the length scale parameter l have been studied in Mesgarnejad et al. [135], leading to a much broader crack path representation, while simultaneously obtaining the force-displacement behaviour comparable to the experimental data. The FE mesh consisting of 62,659 elements is used, with a local refinement in the region of the expected crack propagation.

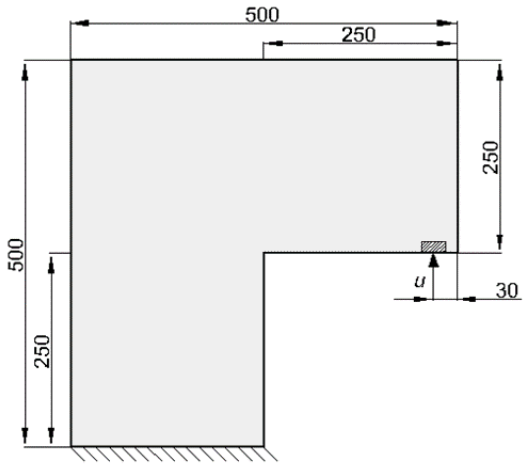

Fig. 4.12. L-shaped specimen. Geometry and boundary conditions

Herein, only the RCTRL staggered algorithm is employed to demonstrate its capabilities on a more complex geometry. Fig. 4.13. and Fig. 4.14. show the crack propagations obtained by the spectral and the spherical-deviatoric decomposition, respectively. The results are compared to the experimental measurements provided in Winkler et al. [167], shown with the white overlay.

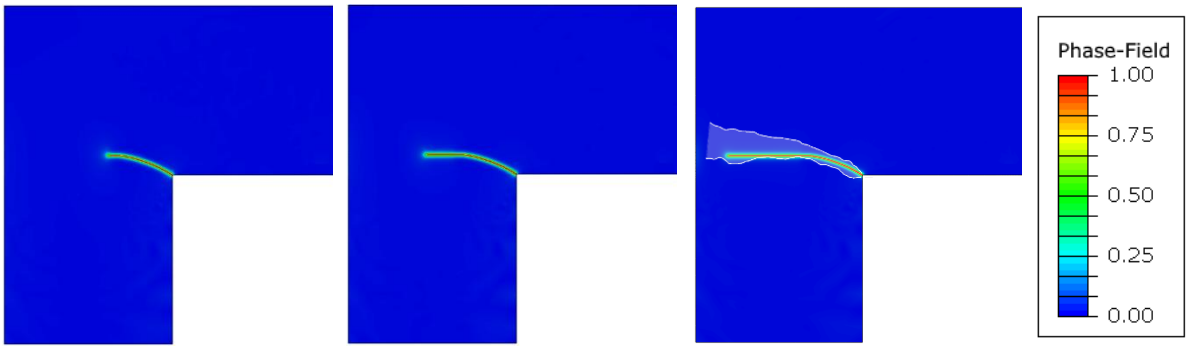

a) b) c)

Fig. 4.13. L-shaped specimen. Crack pattern obtained by the spherical-deviatoric energy decomposition at a) u = 0.265 mm, b) u = 0.3 mm, c) u = 0.5 mm with experimental envelope from [167]

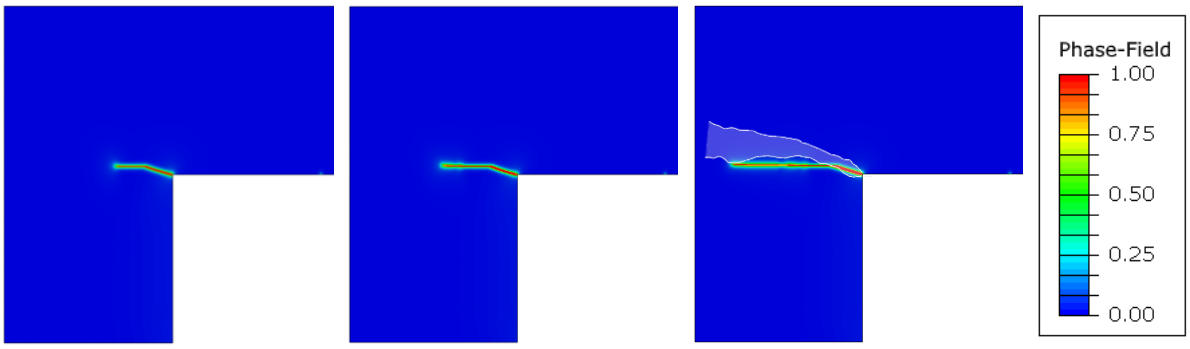

a) b) c)

Fig. 4.14. L-shaped specimen. Crack pattern obtained by the spectral energy decomposition at a) *u* = 0.265 mm, b) *u* = 0.3 mm, c) *u* = 0.5 mm with experimental envelope from [167]

The results computed by the spectral decomposition (Fig. 4.14.) match well with the results presented in Ambati et al. [79]. On the other hand, the results obtained by the spherical-deviatoric decomposition (Fig. 4.13.) show much better agreement with the experimental results as shown in Fig. 4.13.c). It has to be noted that the crack propagation obtained by the spherical-deviatoric decomposition of the strain energy could only be achieved by setting the Dirichlet boundary condition $\phi = 0$ in the vicinity of the loading point (hatched area shown in Fig. 4.12.). With the boundary conditions preventing the cracking in the loading area, the model without any energy decomposition also yields the results very similar to those shown in Fig. 4.13., at a much lower computational cost. Such model has a practical advantage due to the fact that within a staggered approach, the momentum equation is linear as there is no decomposition of the strain tensor, thus leading to a much faster numerical calculation.

4.1.4. Asymmetrically notched perforated three-point bending test specimen

To further validate the proposed algorithm, a well-studied benchmark test concerning an asymmetrically notched beam with three holes, inducing complex curvilinear crack paths, is studied. The experimental testing has been carried out by Ingraffea and Grigoriu [168] on a commercial plexiglas (the cyro acrylic FF plexiglas MC). The geometry and boundary conditions are presented in Fig. 4.15. The material properties $E = 20.8$ GPa, $\nu = 0.3$ and $G_c = 1\times10^{-3}$ kN/mm are adopted from Miehe et al. [72], together with the length scale parameter $l = 0.025$ mm.

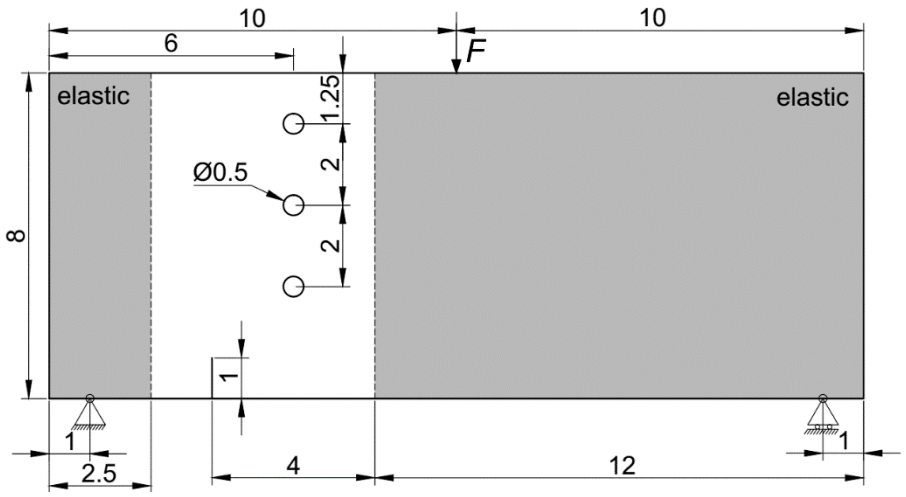

Fig. 4.15. Geometry and boundary conditions of the asymmetric three-point bending test specimen

The specimen is discretized by 321,154 finite elements, 320,601 of which are the proposed 3-layered finite elements employing the full RCTRL staggered algorithm. The remainder of elements contains only the second element layer, which makes them the standard linear elastic finite elements without the phase-field fracture computation. These zones are labelled "elastic" in Fig. 4.15. Similar practice of setting $\phi = 0$ in these zones has been used in [127, 135]. This way, the spurious crack propagation around the loading *point* is avoided. For this setup, the model with no strain energy decomposition can be used to obtain accurate result, thus significantly speeding up the computation. Note that the force-controlled load is applied. As a result, the arc-length (Riks) solver is used, instead of the standardly used Newton-Raphson solver. The resulting crack path, presented in Fig. 4.16, matches well with the experimental measurements spanning from the notch up to the middle hole. In addition, the calculated crack zone remains thin and does not exhibit spurious widening as in the single iteration algorithm implementations [127].

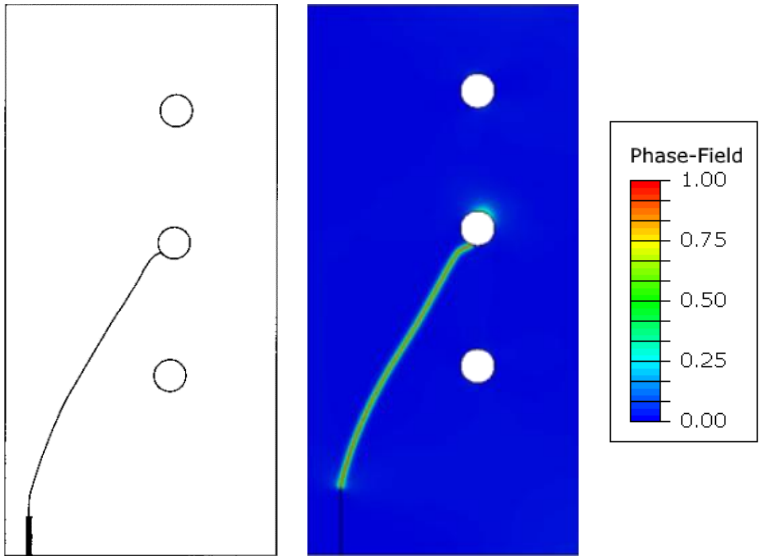

a) b)

Fig. 4.16. Asymmetric three-point bending test crack path. a) experimental results from [169], b) residual control staggered algorithm result

The ability of the phase-field implementation to solve such force-controlled problem with the arc-length (Riks) solver is thus shown.

Thread Parallelization

Following Section 3.3.3., the example is also solved in a parallelized manner with up to 6 CPUs. Total computational time for the stated cases is given in Table 4.3.

Table 4.3. Thread parallelization computational time comparison

Number of threads	1	2	3	4	5	6
Wallclock time (s)	87562	69090	64752	63754	55901	56429

The thread-parallelization option, introduced in this work, is shown to significantly speed up the simulations. Thus, one of the crucial setbacks of phase-field fracture models is alleviated. As explained in Section 3.3.3., due to the complexity of layered system, the element operations are executed with a single thread. The thread-parallelization is only introduced at the global system assembly and calculation level. Therefore, the influence of this option on the computational time saving is more pronounced in examples with large FE mesh sizes, like the one at hand.

4.1.5. Complex porous microstructure geometry

After showing the capabilities of the proposed implementation by solving some benchmark examples where a crack path is known *a priori*, an example of steel microstructure with random porosities is examined. The RCTRL algorithm is tested further, emphasizing the importance of a stopping criterion within the phase-field staggered solution scheme.

The microstructure is presented by a 0.2 × 0.2 mm microstructural specimen consisting of 13% randomly distributed voids with the average radius of 0.043 mm. The assumed material properties are: $E = 210$ GPa, $\nu = 0.3$, $G_c = 2.7\times10^{-3}$ kN/mm. The geometry and boundary conditions are presented in Fig. 4.17. The numerical model is discretized by 31,008 uniformly distributed finite elements with the average characteristic element length $h = 0.001$ mm. The length scale parameter is chosen to be $l = 0.0025$ mm.

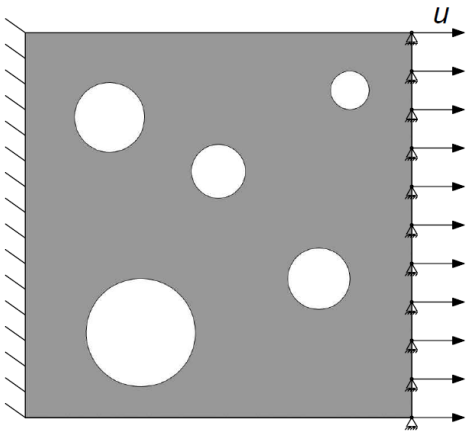

Fig. 4.17. Porous steel microstructural specimen. Geometry and boundary conditions

The solution is obtained by the proposed algorithm utilizing the automatic loading incrementation. To compare the solution accuracy and the CPU time required, the obtained results are compared to the solutions computed by SI staggered algorithm using 5 different loading increment sizes, namely $\Delta u = 1\times10^{-3}$ mm, $\Delta u = 1\times10^{-4}$ mm, $\Delta u = 1\times10^{-5}$ mm, $\Delta u = 1\times10^{-6}$ mm and $\Delta u = 1\times10^{-7}$ mm. The force-displacement curves displayed in Fig. 4.18. show the structural behaviour similar to the previously presented homogeneous case. Again, the results of the SI algorithm match well with the RCTRL algorithm results only for very fine loading increment sizes.

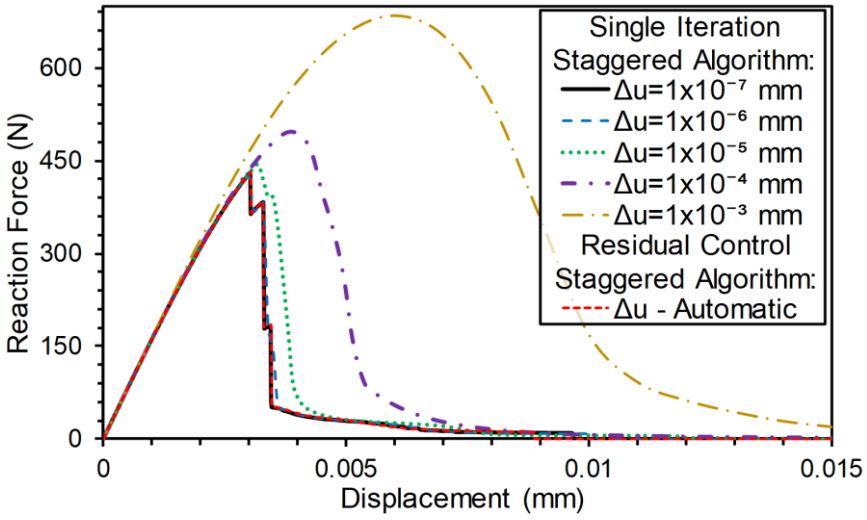

Fig. 4.18. Porous steel microstructural specimen. Force-displacement curves

Interestingly, even the crack paths seem to be dependent on the loading increment size of SI staggered algorithm in this example, as can be seen in Fig. 4.19. This further emphasizes the importance of stopping criterion application within the staggered algorithm.

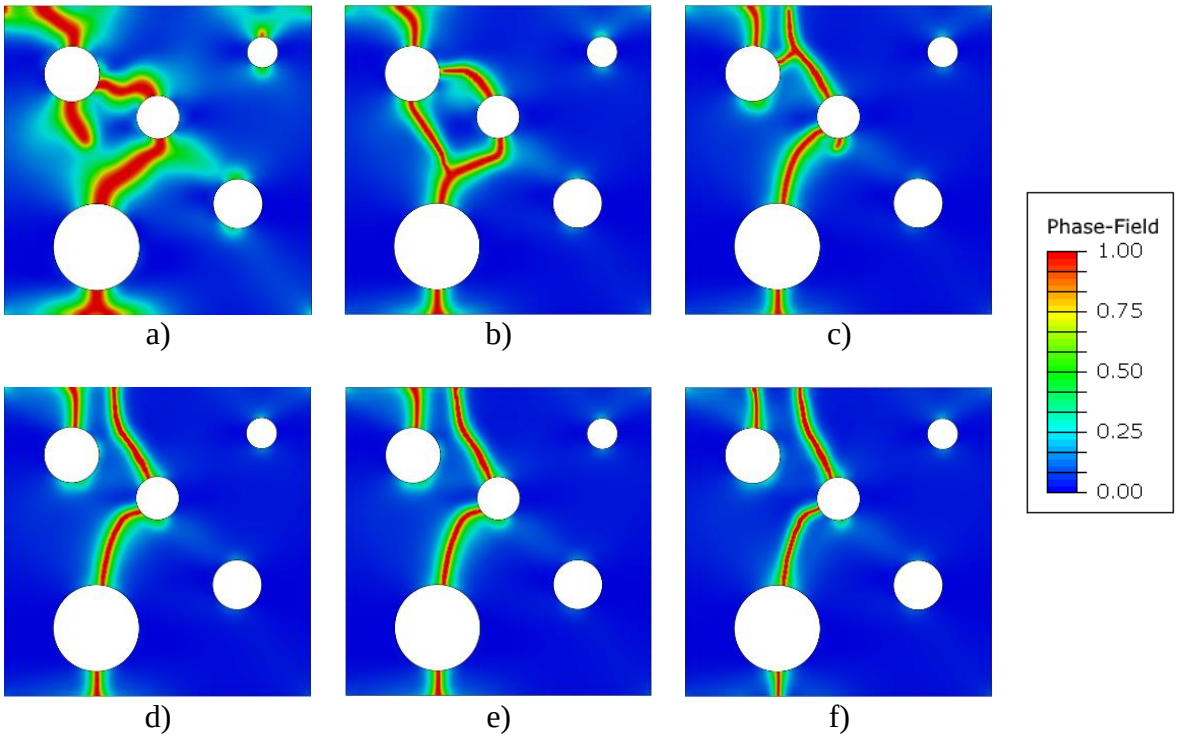

Fig. 4.19. Porous steel microstructural specimen. Crack patterns obtained by SI staggered algorithm with: a) $\Delta u = 1\times10^{-3}$ mm, b) $\Delta u = 1\times10^{-4}$ mm, c) $\Delta u = 1\times10^{-5}$ mm, d) $\Delta u = 1\times10^{-6}$ mm, e) $\Delta u = 1\times10^{-7}$ mm, and f) RCTRL algorithm with automatic loading incrementation

The results obtained by both energy decompositions are nearly identical to the presented results obtained without the energy decompositions, as the tensile stress state is predominant in this setup.

Finally, the CPU time comparison is given in Table 4.4. It is again demonstrated that the proposed RCTRL algorithm is much faster than SI algorithm for the similar accuracy, i.e., for the curves obtained by $\Delta u = 1\times10^{-6}$ mm and $\Delta u = 1\times10^{-7}$ mm. The CPU time comparison results are done in [132].

Table 4.4. Porous steel microstructural specimen. CPU time consumption

Algorithm	SI staggered algorithm					RCTRL staggered algorithm
Loading increment Δu	1×10^{-3} mm	1×10^{-4} mm	1×10^{-5} mm	1×10^{-6} mm	1×10^{-7} mm	Automatic incrementation
CPU time (s)	210	2,231	27,368	297,051	1,556,650	62,107

4.2. Monotonic loading - Ductile material behaviour examples

4.2.1. V-Notch bar

The presented generalized phase-field fracture implementation's ability to solve the ductile material behaviour is first tested on a 2D example presented in Miehe et al. [80]. It follows the experimental validation on Aluminium alloy done by Li et al. [170]. The geometry and boundary conditions of V-notch bar are shown in Fig. 4.20. The FE mesh consists of 46,975 elements and is refined in the region of expected crack propagation.

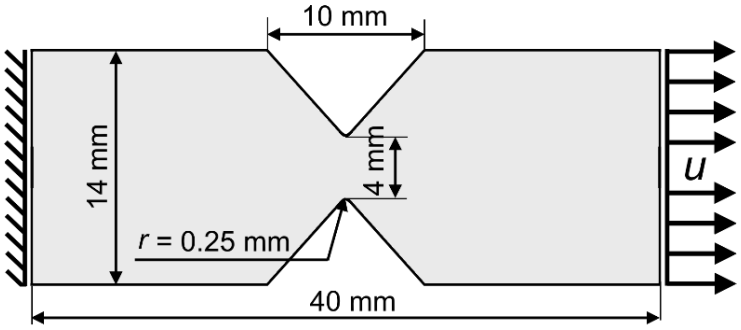

Fig. 4.20. V-notch bar. Geometry and boundary conditions

The material properties of Al-6061 [170] are taken as $E = 68.9$ GPa, $\nu = 0.33$, $h_{\text{iso}} = 561$ MPa and $\sigma_y^0 = 475$ MPa as the initial yield stress. The simple linear isotropic hardening $\sigma_{\text{y}}\left(\varepsilon_{\text{eqv}}^{\text{p}}\right) = \sigma_{\text{y}}^0 + h_{\text{iso}} \cdot \varepsilon_{\text{eqv}}^{\text{p}}$ is used. Furthermore, fracture material properties used with the TH model are chosen as $G_{\text{c}} = 40$ N/mm and $l = 0.15$ mm. Fig. 4.21. presents the obtained crack path solution which matches well with the numerical solutions obtained in [80, 81, 171].

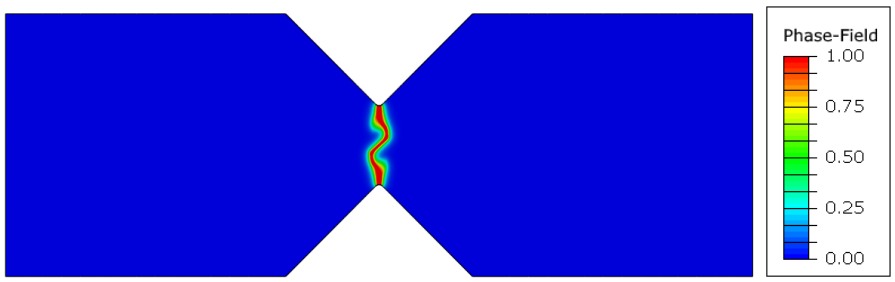

Fig. 4.21. V-Notch bar. Crack path

The force-displacement curves are shown in Fig. 4.22. in comparison with the experimental measurements from Li et al. [170], and the numerical results from Miehe et al. [171] obtained by using the finite strains setting and a gradient-extended plasticity model.

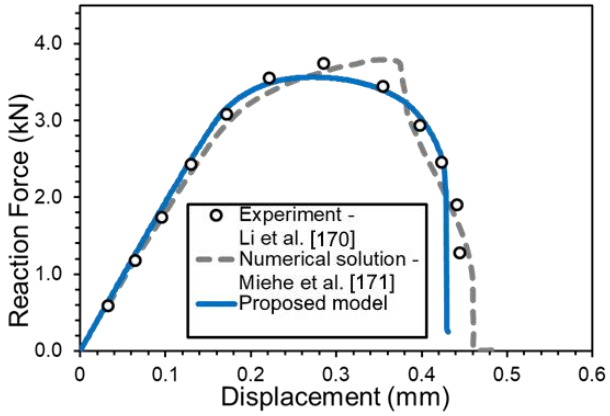

Fig. 4.22. V-Notch bar. Force-displacement curves

The obtained solution matches very well with the experimental measurements. The implementation's stability should be emphasized here allowing the algorithm to easily converge and pose no additional problems moving to generalized elastoplastic formulation. The role of the *consistent* elastoplastic tangent modulus is crucial in achieving the computational stability of such coupled framework.

4.2.2. Asymmetrically Notched Specimen

The model's performance is next tested on a 3D example of an asymmetrically notched specimen. The specimen geometry and loading conditions are illustrated in Fig. 4.23., together with the experimental results given in Ambati et al. [105]. The specimen is 3 mm thick and is made from the aluminium alloy Al-5005. The corresponding material properties are taken from [105]: $E = 70.9$ GPa, $\nu = 0.34$, $\sigma_y^0 = 113$ MPa, $Q_\infty = 22$ MPa, $b = 24.5$ and

$G_c = 254.66$ N/mm. The saturation type isotropic hardening $\sigma_y\left(\varepsilon^{\mathrm{p}}_{\mathrm{eqv}}\right) = \sigma_y^0 + Q_\infty\left(1 - \exp\left[-b\varepsilon^{\mathrm{p}}_{\mathrm{eqv}}\right]\right)$ is used in this example, where σ_y^0 is the initial elasticity limit, Q_∞ and b are the material parameters defining the maximum increase in yield stress due to hardening at saturation (when $\varepsilon^{\mathrm{p}}_{\mathrm{eqv}} \to \infty$), and the rate of saturation, respectively. The length scale parameter $l = 1.5$ mm is used for the TH model, being 5 times larger than the one used in [105] for the AT-2 model, according to equation (2.33). The FE model consists of 16,395 hexahedral finite elements with the refinement in the expected crack propagation region. The model employs symmetry in the thickness direction.

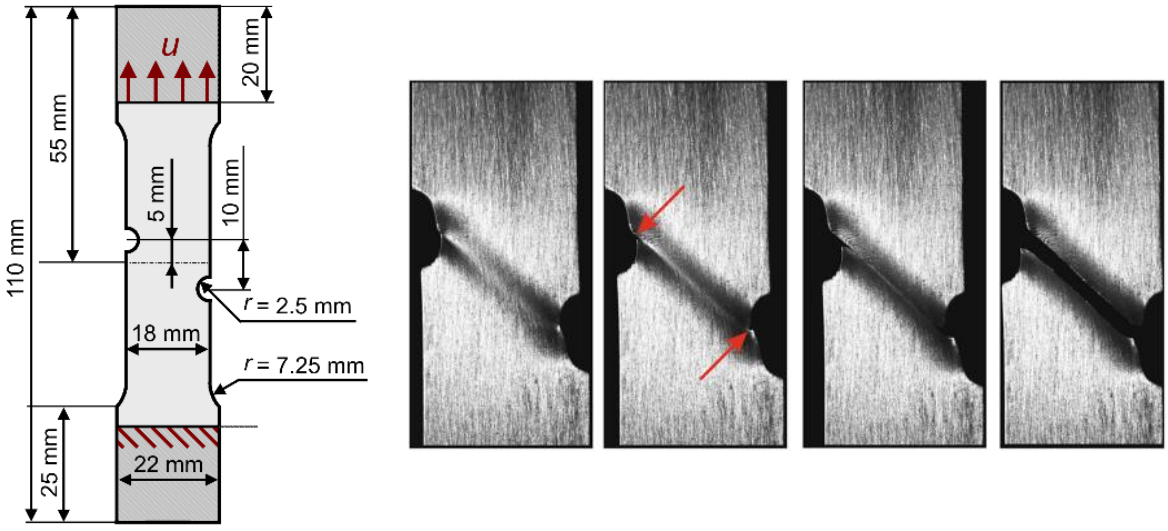

a) b)

Fig. 4.23. Asymmetrically notched specimen. a) Geometry and boundary conditions, b) Experimental results [105]

The parameter ζ (2.29) has been increased to $\zeta = 2.5$ to speed up the post-critical fracture behaviour. The force-displacement curves are given in Fig. 4.24. It should be stressed again that the results are obtained with the small strain setting which might be the reason for the discrepancy between the numerical and experimental results. However, taking that into account, the curve matches experimental measurements well.

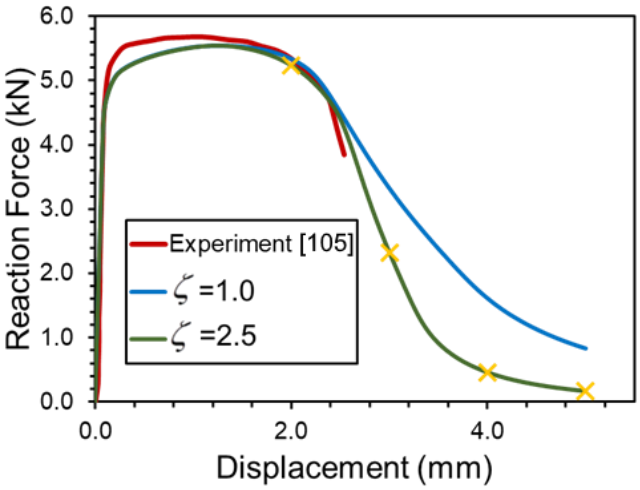

Fig. 4.24. Asymmetrically notched specimen. Force-Displacement curve

The crack phase-field contour plots at different loading stages (marked by yellow symbols in Fig. 4.24.) are shown in Fig. 4.25. The results closely resemble the experimentally observed results. The elements with phase-field value greater than 0.75 are removed from the plot in post-processing for better visualization.

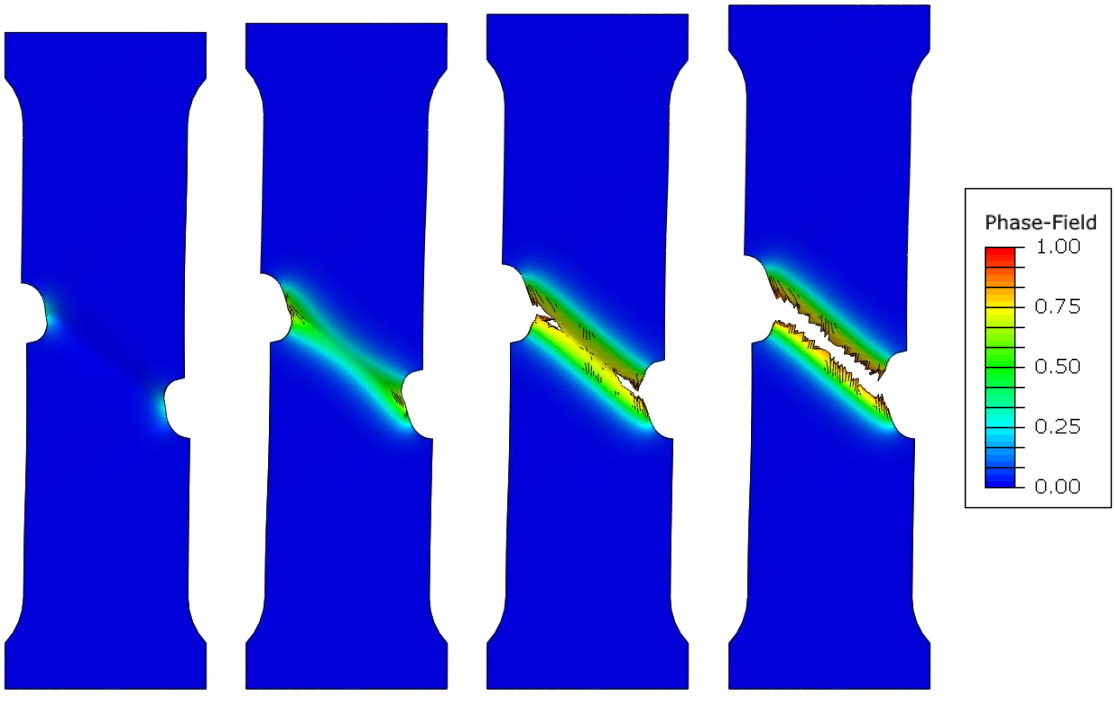

a) b) c) d)

Fig. 4.25. Asymmetrically notched specimen. Phase-field crack contour plot at a) u = 2 mm, b) u = 3 mm, c) u = 4 mm, d) u = 5 mm

4.2.3. Sandia fracture challenge 2012

To complete the testing of the proposed implementation in solving ductile fracture problems, a famous specimen geometry, which started out as a blind round-robin challenge proposed by Sandia National Lab in 2012, is analysed. The specimen geometry and loading conditions are shown in Fig. 4.26., taken directly from Boyce et al. [172]. The holes (B-C-D) are located approximately one plate thickness away from the tip of the blunt notch to induce a complex fracture process with three separate potential localization paths. The measured plate thickness was 3.124 mm.

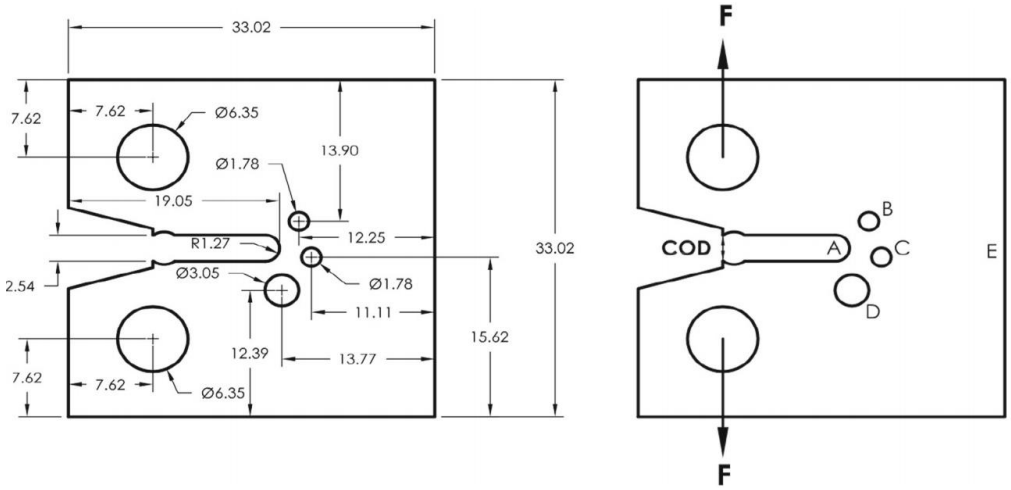

Fig. 4.26. Sandia Challenge Specimen. Geometry and loading conditions, dimensions in mm [172]

The material used was a precipitation hardened martensitic stainless-steel alloy 15-5 PH. In the original Sandia fracture challenge [172], the complete material chemical composition is given, together with the detailed records of heat treatment, machining diagrams and the metallographic analysis of the martensitic stainless-steel microstructure. Moreover, detailed tensile test results for different rolling directions were provided together with the fracture toughness test measurements on CT specimens. The amount of data provided was intended to be comparable with the amount of data typically available in real industrial engineering scenarios. The data were then used by challenge participants to calibrate the model parameters.

The experimental measurements on ten specimens were provided after the challenge completion. Fig. 4.27. shows the broken specimens where crack paths can be easily observed.

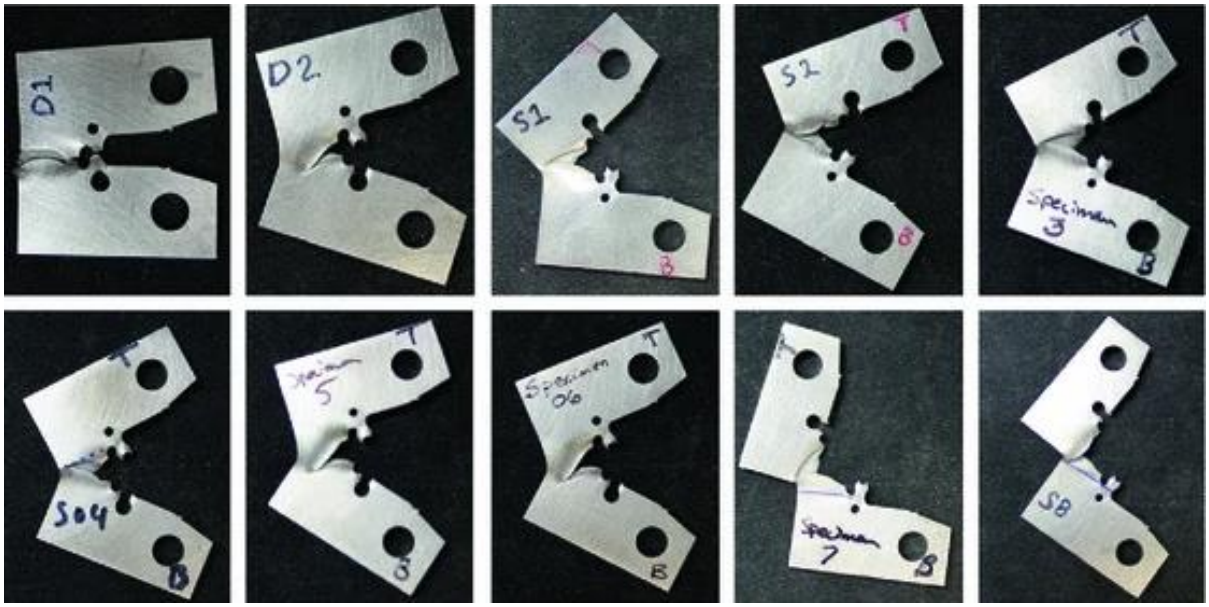

Fig. 4.27. Sandia Challenge Specimen. Post-test images of the ten specimens tested in the Sandia's Structural Mechanics laboratory [172]

The elastoplastic material parameters are taken over from Gross and Ravi-Chandar [173] as $E = 199$ GPa, $\nu = 0.3$, $C_1 = 755.4$ MPa, $C_2 = 818.1$ MPa, $C_3 = 0.005674$, $C_4 = 0.2889$, constituting general power law for isotropic hardening $\sigma_y = C_1 + C_2\left(C_3 + \varepsilon_p^{eqv}\right)^{C_4}$. Fracture material parameters are set to $G_c = 500$ N/mm and $l = 0.5$ mm. A 3D numerical model is used, with 31,220 hexahedral finite elements with symmetry employed in the thickness direction. The loading pins boundary conditions are simulated by kinematically constraining nodes at the hole edge constituting 60° angle with the reference point at the pin centreline, as shown in Fig. 4.28. Following the experimental setup description [172], the reference point corresponding to the top pin is fixed, while the load is imposed to the bottom pin reference point. Two cases of load implementation are considered here. First, the loading is realized by imposing the displacement-controlled load to the reference point using the standard Newton-Raphson solver, analogously to the previous examples. Secondly, the reference point is subjected to the force-controlled loading, and the problem is solved by the arc-length (Riks) solver.

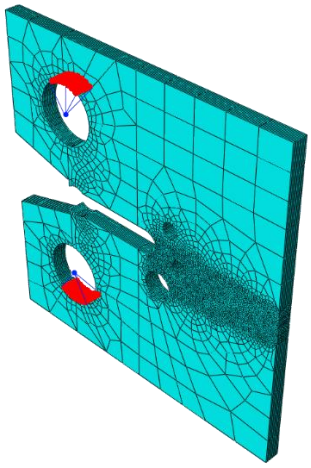

Fig. 4.28. Sandia Challenge Specimen. Loading pin boundary conditions and FE mesh

The final specimen configuration obtained by the proposed model is presented in Fig. 4.29., to visualize the final crack path. The resulting crack pattern follows the path *A-C-E* (marked in Fig. 4.26.), corresponding to the numerical results obtained in [172, 173].

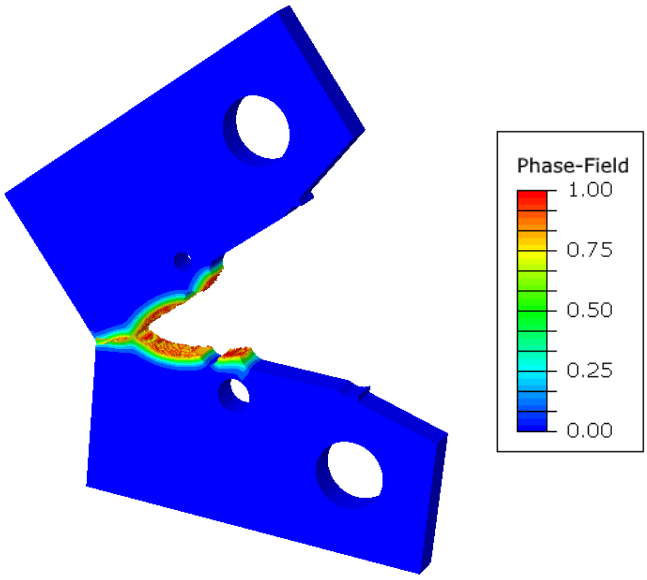

Fig. 4.29. Sandia Challenge Specimen. Final crack path numerical results

Furthermore, the equivalent plastic strain contours are presented in Fig. 4.30. in comparison with the experimental results obtained by DIC (digital image correlation) presented in Gross and Ravi-Chandar [173].

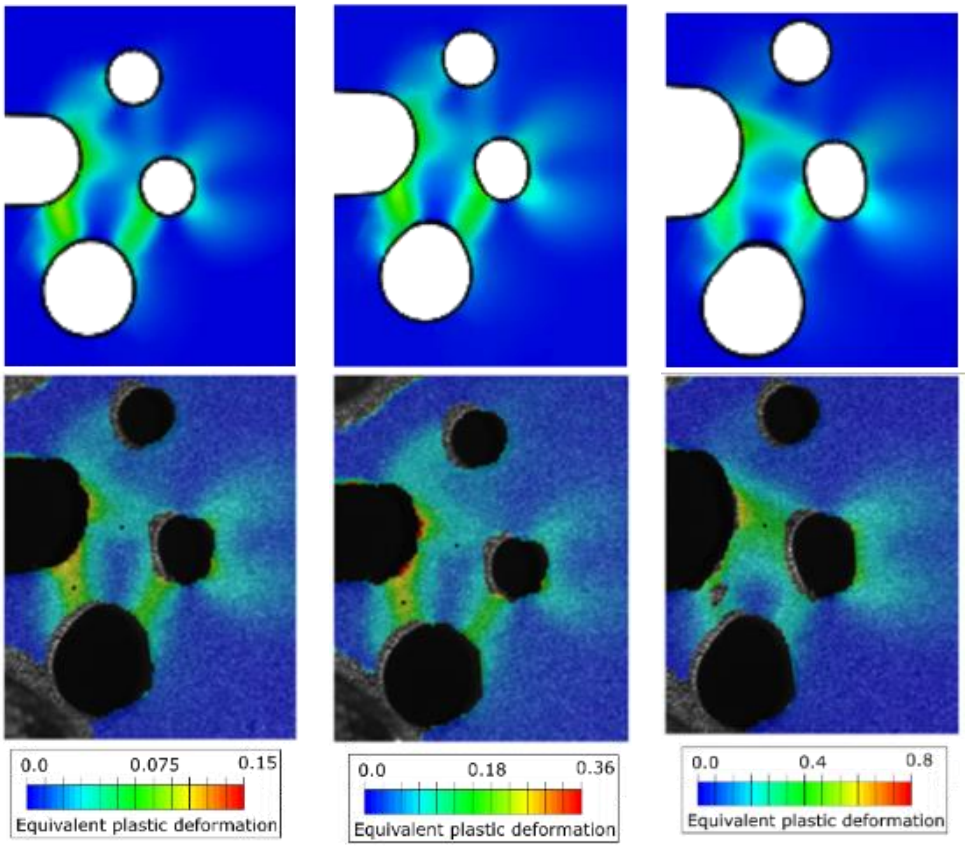

a) b) c)

Fig. 4.30. Sandia Challenge Specimen. Equivalent plastic strain development (top row) in comparison with experimental results obtained by 3D DIC and taken from [173] at a) COD ~ 1mm, b) COD ~ 2mm, c) COD ~ 3mm

The equivalent plastic strain development results match well with the experimental results. Slight discrepancies can be attributed to the employment of small-strain settings. Moreover, Fig. 4.31. presents the obtained load versus crack opening displacement (COD) in comparison with the experimental results from [172].

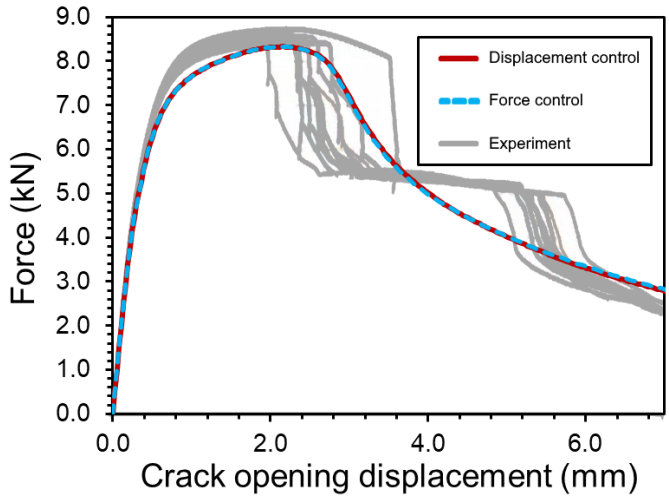

Fig. 4.31. Sandia Challenge Specimen. Force-COD comparison with experimental envelope [172]

The obtained computational results show a good agreement with the experimental results in terms of the crack pattern and the force-COD curves. However, the abrupt drop in load-displacement observed in experiments could not be captured but might be improved by further calibration of the plasticity and phase-field parameters. Both displacement- and force-controlled load boundary condition give the same result, as expected.

4.3. Cyclic loading - fatigue material behaviour examples

4.3.1. Homogeneous example

Following Section 2.3., the fatigue degradation function $\hat{F}(\bar{\psi})$ is added, with the material parameter $\bar{\psi}_\infty$ included, to recover high-cycle and transition to low-cycle regime. The cycle-skipping technique presented in Section 3.4. is used throughout this section, where applicable.

The first example is used to assess the ability of the model to recover the full scope of fatigue domain, ranging from low- to high-cyclic regime. It follows the example of a cyclically loaded round bar specimen, experimentally tested by Čanžar [174]. The specimen is discretized by a single truss element. The geometry and boundary conditions are illustrated in Fig. 4.32. The strain-controlled sinusoidal loading is used with load ratio $R = 0.$

Fig. 4.32. Cyclically loaded round bar specimen. Geometry and boundary conditions

The material properties of nodular cast iron with nonlinear isotropic and kinematic hardening are taken from [174] for the so-called Flotret casting technique. The elastoplastic material properties are set as follows: $E = 140$ GPa, $\nu = 0.3$, $\sigma_y^0 = 123$ MPa, $Q_\infty = 95$ MPa, $b = 18$, $C_1 = 22,734$ MPa, $\gamma_1 = 261.8$, $C_2 = 136,029$ MPa, $\gamma_2 = 2,113.5$. The fracture toughness is set to $G_c = 74$ N/mm following the *J*-integral measurements taken in [174, 175]. The length scale parameter is chosen to be $l = 0.25$ mm, while the fatigue material parameter is set to $\bar{\psi}_\infty = 5000$ MPa. First, the elastoplastic material model is tested in comparison with the experimental results for loading the amplitude $\varepsilon_a = 0.8\% \pm 0.8\%$. The stress-strain diagram in Fig. 4.33.a) shows the comparison with the experimental measurements from [175], until the

onset of fracture. The time evolution of stress, energetic values and phase-field parameter is shown in Fig. 4.33.b).

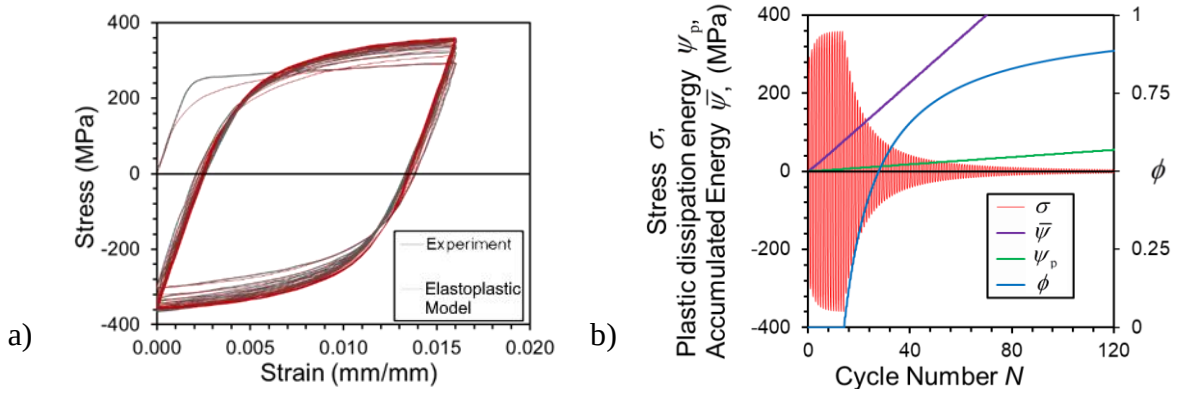

Fig. 4.33. Cyclically loaded round bar specimen. a) Stress-strain hysteresis loop experimental comparison [175], b) time evolution of stress, energy density variables and phase-field parameter

The results obtained with the proposed model match the experimental measurements well. A slight discrepancy can be observed in the first cycle, as expected, because the material properties were calibrated for the stabilized hysteresis loop. It can be clearly seen how the dissipated plastic energy ψ_{p} and accumulated energy density $\bar{\psi}$ grow with each cycle. Their respective slopes are influenced by the magnitude of load amplitude, i.e., the influence of ψ_{p} diminishes and eventually vanishes with lower amplitudes, which makes for the transition between low- and high-cyclic fatigue regime.

The specimen has been subjected to 35 different strain amplitudes to assess the model behaviour in different fatigue regimes. The simulations are stopped at cycle N_{f}, when the phase-field parameter reaches the value $\phi = 0.99$, thus assuming the total failure. Fig. 4.34. presents the $\varepsilon - N$ curve for the fatigue functions (2.49) presented in Chapter 2, with $\bar{\psi}_{\infty} = 5000$ MPa, as well as the case without the fatigue degradation named “noF”. Note that each marker in Fig. 4.34. represents a full simulation obtained with a different load amplitude.

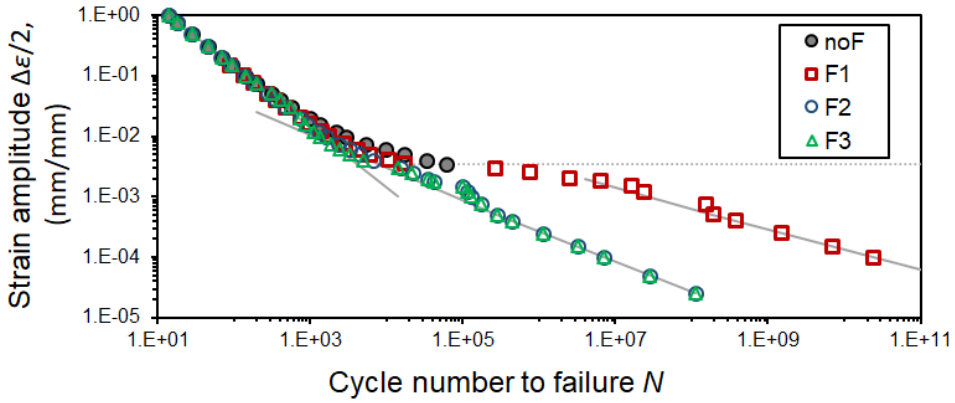

Fig. 4.34. Cyclically loaded round bar specimen. $\varepsilon - N$ curve

The obtained results show great resemblance to the theoretical $\varepsilon - N$ curve (Fig. 2.5.b). Clear difference can be seen in the results obtained by $\hat{F}_1$, when compared to the results obtained with $\hat{F}_2$ and $\hat{F}_3$, due to the difference in function descriptions. Moreover, it is obvious that the fracture can be obtained with large loading amplitude values even with the model without fatigue degradation, up until the point where plastic energy in system becomes negligible, shown as "noF limit". On the other hand, the so-called dynamic endurance threshold is not clearly shown. However, the total fracture cycle number grows beyond 10^8 for the strain amplitude values bellow 10^{-5} mm/mm, indicating the existence of this threshold. It can be thus concluded that the proposed generalized phase-field fracture model is capable of reproducing the low- and high-cycle regime and the transition in-between. Moreover, the strain amplitude and cycle number values N_f correspond to the values normally observed in literature, thus giving even more credibility to these results.

4.3.2. Compact Tension (CT) specimen test – low cyclic regime

To further assess the proposed model's capability in reproducing the fatigue crack evolution, the compact tension (CT) specimen subjected to a cyclic loading is simulated. The geometry is presented in Fig. 4.35., corresponding to the experimental setup made by Čanžar et al. [175].

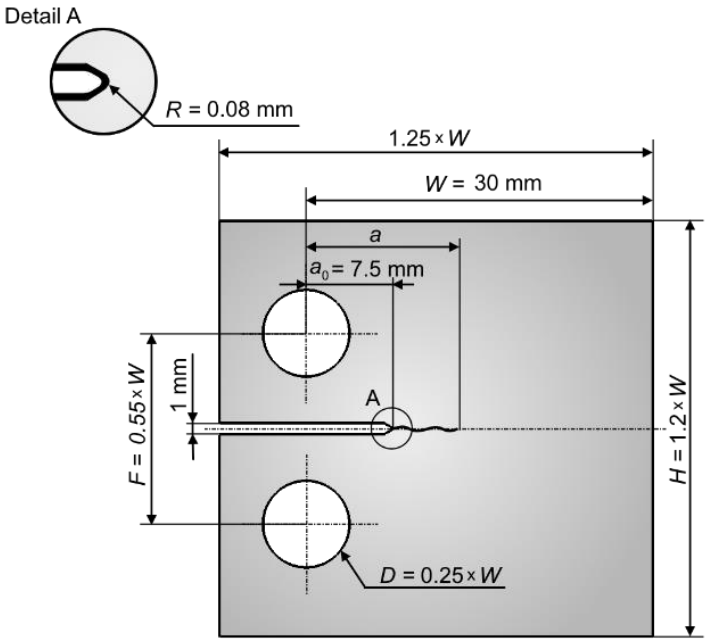

Fig. 4.35. Cyclically loaded CT specimen. Geometry with thickness $B = 0.5W$

The loading boundary conditions are modelled similarly to the previously shown Sandia challenge example. However, the reference point corresponding to the bottom pin is now fixed, while the force-controlled sinusoidal load is assigned to the top pin reference point. Even though the force-control is imposed, the standard Newton-Raphson solver can be efficiently used in this example until the complete failure point at which the Newton-Raphson solver is unable to converge.

The elastoplastic material properties are taken for the nodular cast iron, as presented in the previous example. The lengths scale parameter is chosen to be $l = 0.05$ mm, while the fracture toughness is set to $G_c = 0.74$ kN/mm accordingly. The fatigue parameter is set to $\bar{\psi}_\infty = 5000$ MPa. Following [174], the load amplitude is set to $F = 6$ kN with the load ratio $R = 0.1$. The obtained crack path after various number of cycles is presented in Fig. 4.36., while the energy density accumulation variable $\bar{\psi}$ (2.46) and the fatigue function $\hat{F}_2$ (2.49) are shown in Fig. 4.37. and Fig. 4.38., respectively.

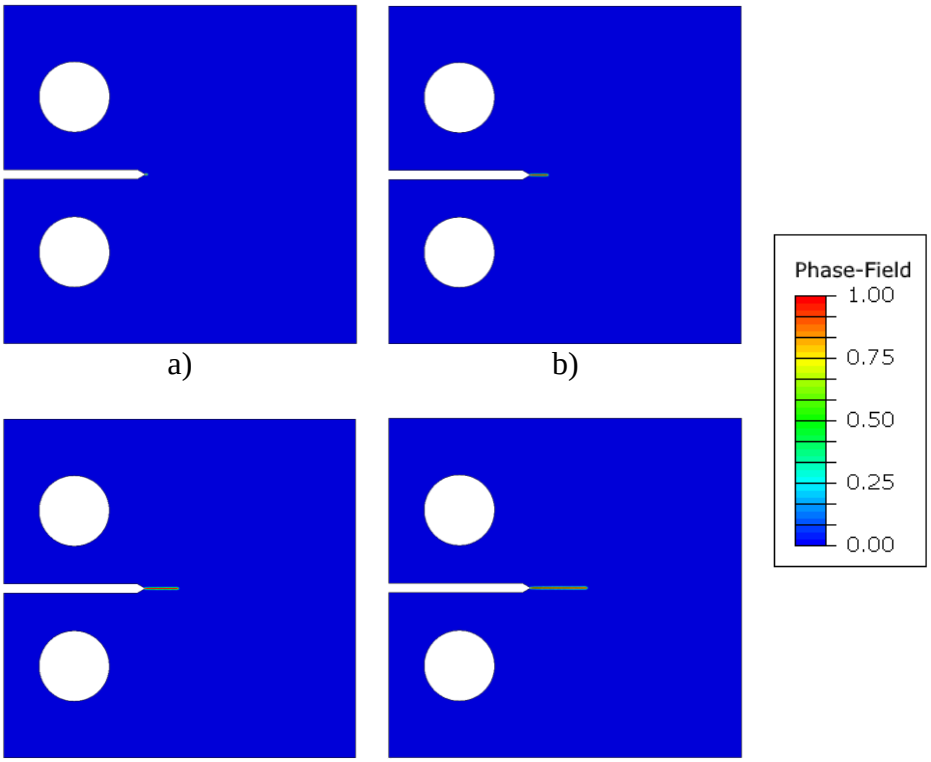

Fig. 4.36. Cyclically loaded CT specimen. Crack path after a) 2000 cycles, b) 7000 cycles, c) 10000 cycles, d) 13000 cycles

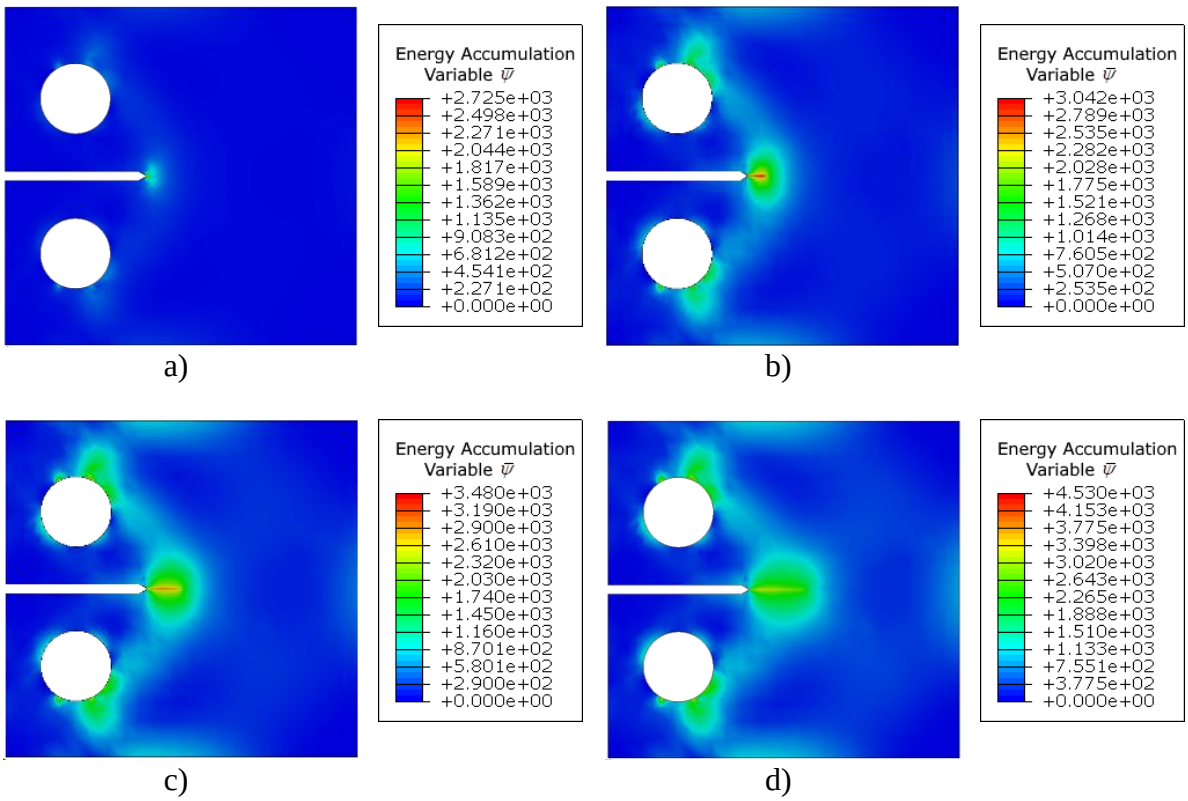

Fig. 4.37. Cyclically loaded CT specimen. Energy density accumulation variable $\bar{\psi}$ in MPa after a) 2000 cycles, b) 7000 cycles, c) 10000 cycles, d) 13000 cycles

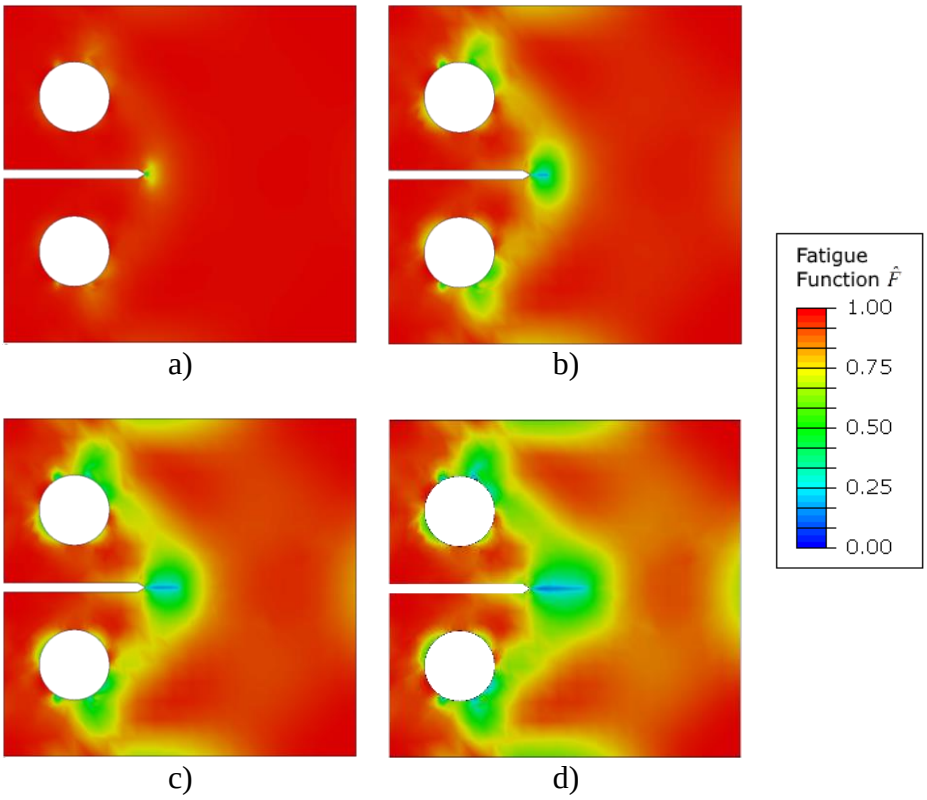

Fig. 4.38. Cyclically loaded CT specimen. Fatigue function $\hat{F}_2$ after a) 2000 cycles, b) 7000 cycles, c) 10000 cycles, d) 13000 cycles

The comparison with the experimentally observed crack propagation is now presented in Fig. 4.39.

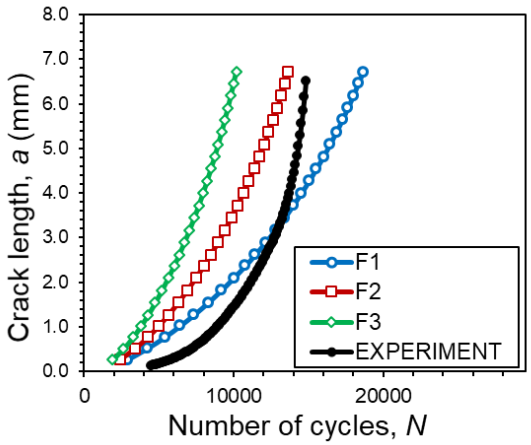

Fig. 4.39. Cyclically loaded CT specimen. Crack length vs cycle number

It can be seen there are some discrepancies between the experimentally observed and the numerically obtained results. Although better results could be obtained by carefully calibrating the fracture and fatigue material parameters, the corresponding *a* - *N* trend shows great potential in predicting fatigue fracture.

The change in the stress intensity factor can be now calculated as

$$\Delta K_i = \frac{\Delta F}{B\sqrt{W}} f\left(\frac{a_i}{W}\right) \tag{4.1}$$

according to ASTM standard [176], where ΔF is the difference between the minimal and maximal load magnitude, a_i is the current crack length, while B and W are geometric quantities of the specimen, shown in Fig. 4.35. The geometric function $f\left(\frac{a_i}{W}\right)$ [176] is calculated as

$$f\left(\frac{a_i}{W}\right) = \frac{\left(2+a_i/W\right)\cdot\left[0.886+4.64\cdot\left(a_i/W\right)-13.32\cdot\left(a_i/W\right)^2+14.72\cdot\left(a_i/W\right)^3-5.6\cdot\left(a_i/W\right)^4\right]}{\sqrt{\left(1-a_i/W\right)^3}}. \tag{4.2}$$

The crack growth rate $\mathrm{d}a/\mathrm{d}N$ versus the change in stress intensity factor ΔK can now be constructed and is shown in Fig. 4.40. in comparison with the experimental data and the NASGRO curve calculated in [174].

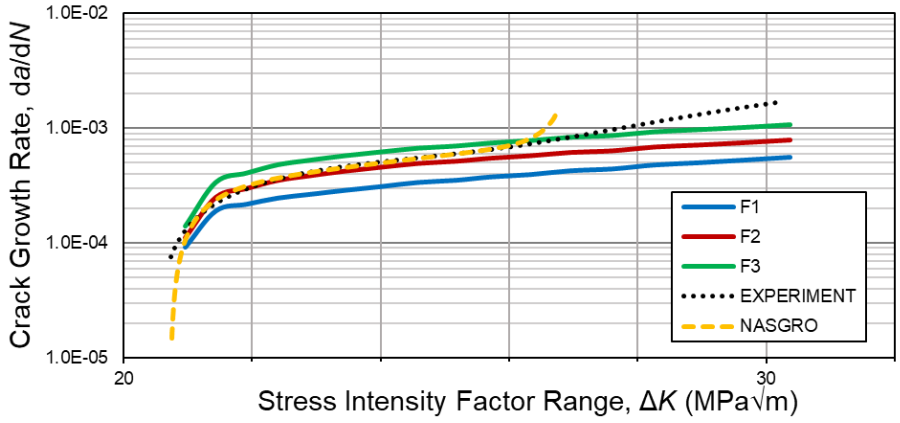

Fig. 4.40. Cyclically loaded CT specimen. Crack growth rate versus stress intensity factor change

It can be observed that there is a great overlap between the experimentally obtained curve, NASGRO equation and numerically obtained curves for the lower values of the stress intensity factor ΔK. However, there seems to be a discrepancy for the higher values of ΔK. The results obtained by the fatigue function $\hat{F}_2$ with the chosen material parameters show the best match in comparison with the experimental results. As already mentioned, a more careful calibration of the fracture and fatigue material parameters could lead to even better match. Nevertheless,

the results show the great potential of the phase-field fracture method in dealing with fatigue problems and in capturing the fundamental features of material fatigue. Again, it has to be noted that no *ad-hoc* criteria are added in this expansion of phase-field fracture model to fatigue, while only one additional parameter, $\bar{\psi}_\infty$, is introduced in the expansion.

4.3.3. Compact Tension (CT) specimen test – high cyclic regime

The same specimen geometry is used to assess the influence of different input material parameters. The material is chosen to be linear elastic with the following constant material properties: $E = 210$ GPa, $\nu = 0.3$ and $l = 0.5$ mm. The influence of the load ratio $R = \frac{F_{\min}}{F_{\max}}$, the fatigue parameter $\bar{\psi}_\infty$ and the fracture toughness G_c, is observed in terms of the Paris law and the Wöhler curves. First, the influence of loading amplitude on crack growth rate $\mathrm{d}a/\mathrm{d}N$ versus the stress intensity factor change ΔK is shown in Fig. 4.41. for constant $R = 0$, $G_c = 5$ kN/mm and $\bar{\psi}_\infty = 50$ MPa.

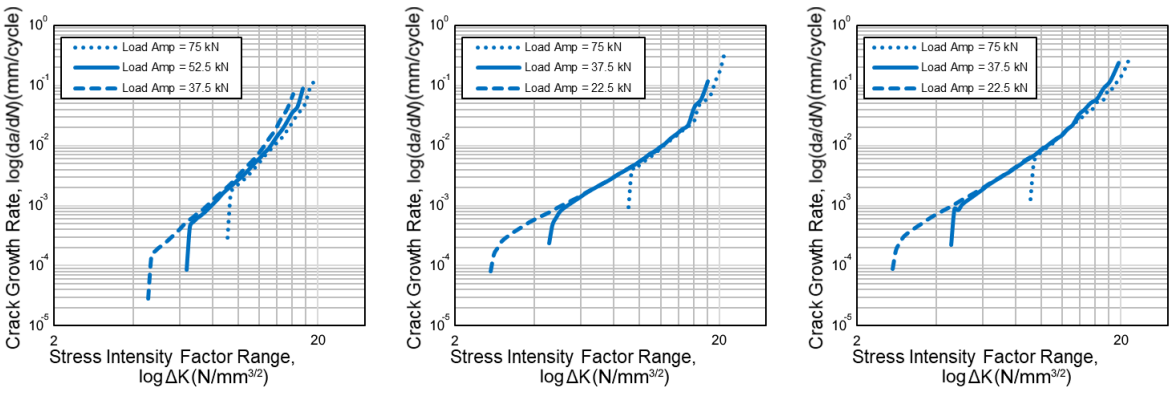

a) b) c)

Fig. 4.41. Crack rate growth versus stress intensity factor change loading amplitude influence for fatigue degradation function a) $\hat{F}_1$, b) $\hat{F}_2$, and c) $\hat{F}_3$

The curves in Fig. 4.41. follow a well-known empirical trend, recovering a major fatigue fracture feature. The steady linear propagation stage usually described by a Paris law follows the same slope for every amplitude. Moreover, the fracture initiation and final unstable growth can be clearly observed as described in Fig. 2.5.a). With the increase of loading amplitude, the threshold value ΔK_{th}, at which the crack initiates, is also increased, which is in accordance with known empirical data. The influence of the loading amplitude on the fatigue life, i.e., the number of cycles to the total failure is presented in Fig. 4.42. in terms of Wöhler curves, where instead of stress, the loading amplitude is set on the *y*-axis.

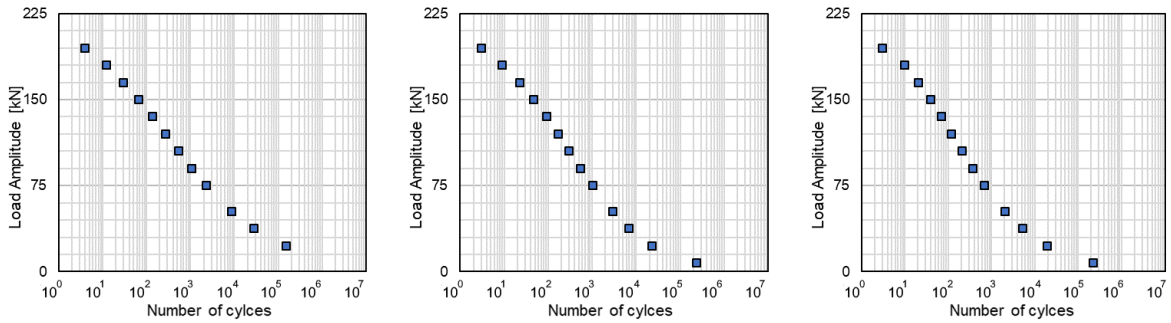

a) b) c)

Fig. 4.42. Fatigue life for a) $\hat{F}_1$, b) $\hat{F}_2$, and c) $\hat{F}_3$ fatigue degradation function

4.3.3.1. The influence of the load ratio R

The load ratio influence is tested by using the values $R=0$, $R=\frac{1}{3}$, $R=\frac{1}{2}$, and $R=\frac{2}{3}$, while the fracture toughness and the fatigue parameter are held constant at $G_c=5$ kN/mm and $\bar{\psi}_\infty=50$ MPa, respectively. The load ratio influence results are presented in Fig. 4.43. and Fig. 4.44. in terms of the Wöhler curves and the da/dN-versus-ΔK curves, respectively. In Fig. 4.44., three amplitude values according to Fig. 4.41. are used and shown in corresponding line style.

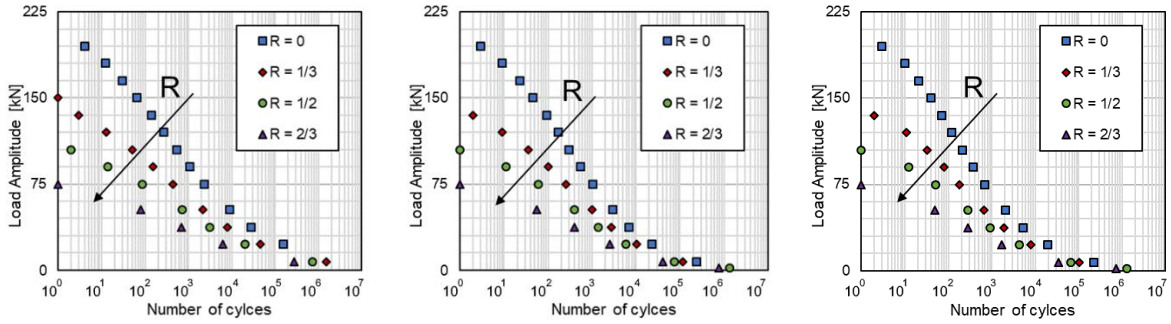

a) b) c)

Fig. 4.43. Load ratio influence on fatigue life for fatigue degradation function a) $\hat{F}_1$, b) $\hat{F}_2$, and c) $\hat{F}_3$

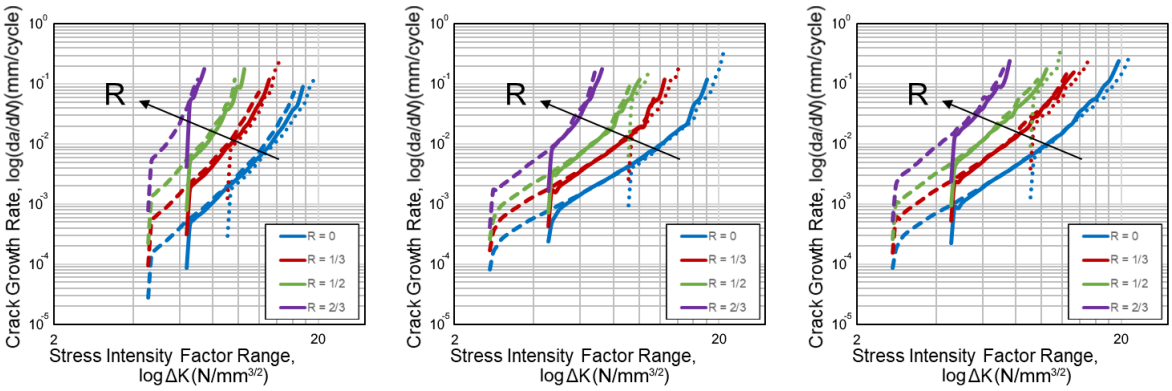

a) b) c)

Fig. 4.44. Load ratio influence on crack rate growth versus stress intensity factor change for fatigue degradation function a) $\hat{F}_1$, b) $\hat{F}_2$, and c) $\hat{F}_3$

Obvious load ratio influence is observed in accordance with known empirical trends. Note that no additional terms in the energy density accumulation variable expression (2.46) have been set to recover the load ratio influence. The results prove the validity of the energy density accumulation variable $\bar{\psi}$ choice where the mean load influence is implicitly included, as explained in Section 2.3.1.

4.3.3.2. The influence of fatigue parameter $\bar{\psi}_\infty$

The influence of the fatigue parameter $\bar{\psi}_\infty$ is tested by applying the loading with $R=0$, while the fracture toughness is again held constant at $G_c = 5$ kN/mm. Three different values of fatigue parameter $\bar{\psi}_\infty$ are tested; $\bar{\psi}_\infty = 20$ MPa, $\bar{\psi}_\infty = 50$ MPa and $\bar{\psi}_\infty = 100$ MPa. The results are shown in Fig. 4.45. and Fig. 4.46. in terms of Wöhler curves and the $\mathrm{d}a/\mathrm{d}N$ -versus- ΔK curves, respectively.

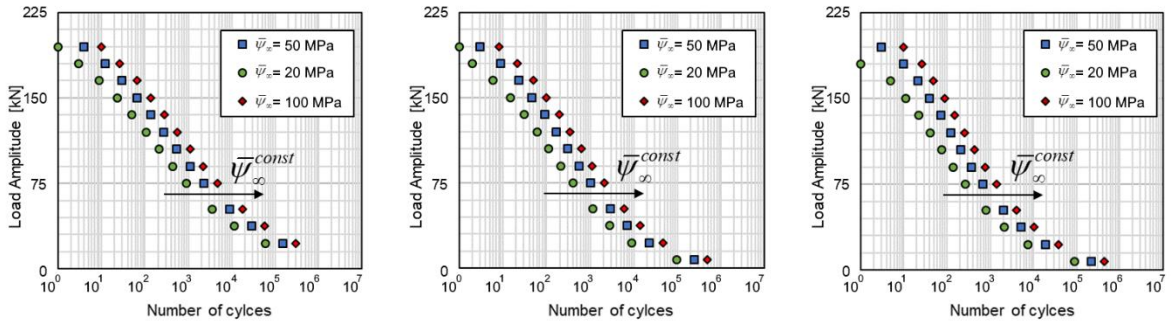

a) b) c)

Fig. 4.45. Fatigue parameter $\bar{\psi}_\infty$ influence on fatigue life for fatigue degradation function a) $\hat{F}_1$, b) $\hat{F}_2$, and c) $\hat{F}_3$

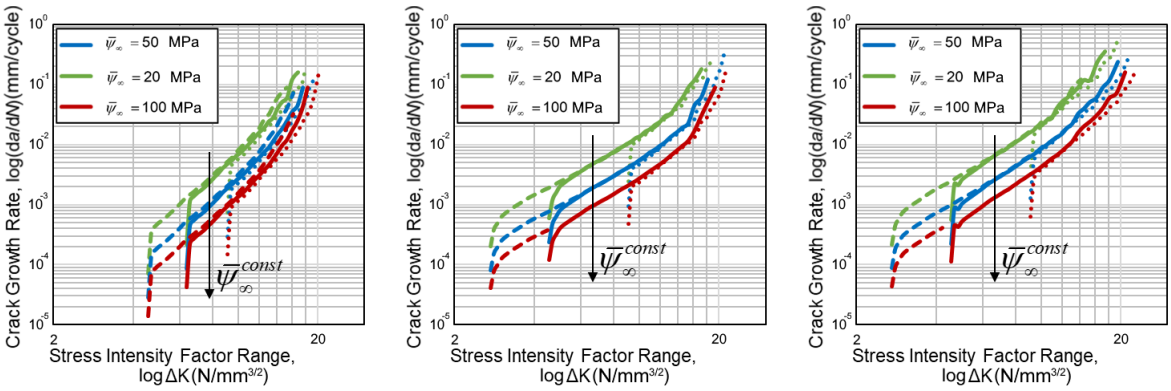

Fig. 4.46. Fatigue parameter $\bar{\psi}_\infty$ influence on crack rate growth versus stress intensity factor change for fatigue degradation function a) $\hat{F}_1$, b) $\hat{F}_2$, and c) $\hat{F}_3$

An increase in fatigue parameter $\bar{\psi}_\infty$ clearly shifts the Wöhler curves to the right by postponing the fatigue crack initiation and propagation. Furthermore, it shifts the crack growth rate $\frac{da}{dN}$ down. Such observation leads to the conclusion that the fatigue parameter $\bar{\psi}_\infty$ could be undoubtedly associated to the fatigue material parameter C used in Paris law $\frac{da}{dN} = C\left(\Delta K\right)^m$, as presented in Fig. 2.5.a). This adds to the validity of the proposed model as the parameter $\bar{\psi}_\infty$ is the only material parameter extending the phase-field fracture model to fatigue regime.

4.3.3.3. The influence of fracture toughness G_c

Following the Paris law empirical equation $\frac{da}{dN} = C\left(\Delta K\right)^m$, where the parameter C is now linked to the parameter $\bar{\psi}_\infty$, the slope in logarithmic scale, controlled by parameter m remains unexplored. It seems the slope in the proposed model is implicitly obtained by already existing fracture material properties, G_c and l. Therefore, to examine the fracture material properties influence on the slope, fracture toughness is changed to $G_c = 1$ kN/mm and $G_c = 25$ kN/mm, while keeping the $\bar{\psi}_\infty = 50$ MPa constant at $R = 0$.

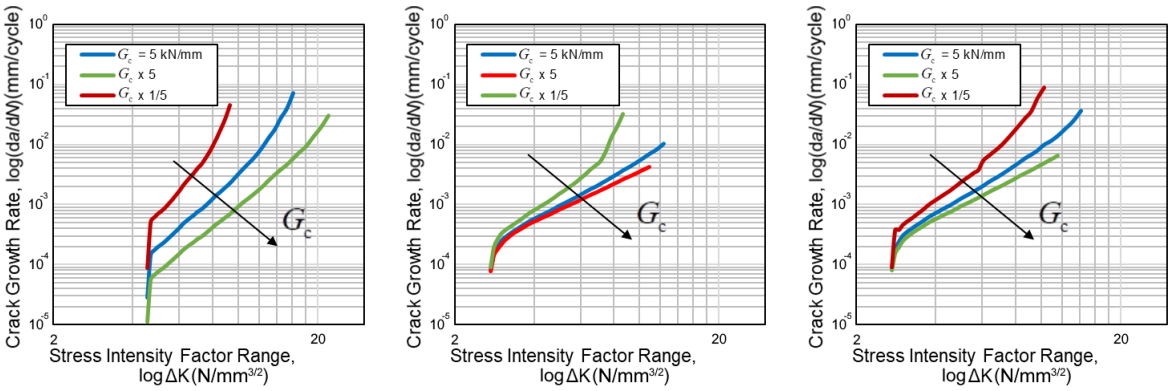

a) b) c)

Fig. 4.47. Fracture toughness G_c influence on crack rate growth versus stress intensity factor change for fatigue degradation function a) $\hat{F}_1$, b) $\hat{F}_2$, and c) $\hat{F}_3$

The results show clear fracture properties influence on the slope of the Paris law curve, more pronounced in the fatigue degradation functions $\hat{F}_2$ and $\hat{F}_3$. Therefore, it can be concluded that the parameter m in the empirical Paris law equation can be directly linked to the fracture material parameters already contained in the phase-field model for monotonic fracture.

Moreover, the fracture material parameters influence on fatigue life in terms of Wöhler curves is presented in Fig. 4.48.

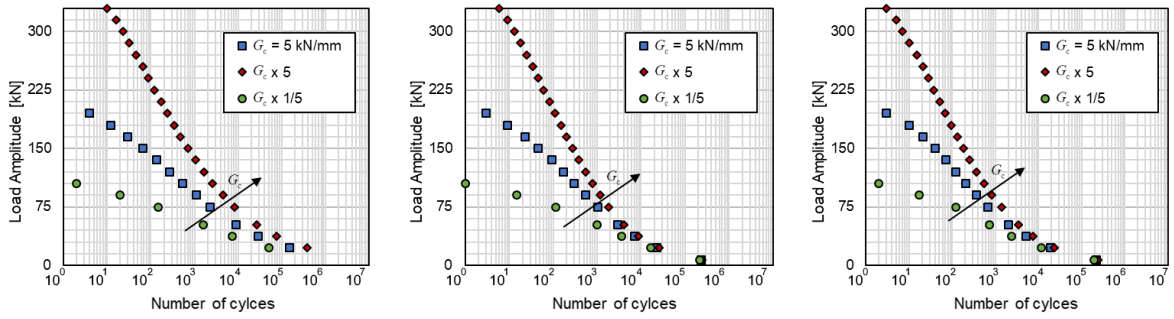

a) b) c)

Fig. 4.48. Fracture toughness G_c influence on fatigue life for fatigue degradation function a) $\hat{F}_1$, b) $\hat{F}_2$, and c) $\hat{F}_3$

The Paris law slope can also be finetuned using the parameter ξ in $\hat{F}_3$ (2.49). For this example, only the function $\hat{F}_3$ is used with $\bar{\psi}_\infty = 50$ MPa, $G_c = 5$ kN/mm and $R = 0$. The change in the Paris law slope is presented in Fig. 4.49. A similar parameter can be introduced into other functions as well, thus having the complete control on fatigue material behaviour described by the Paris law curve.

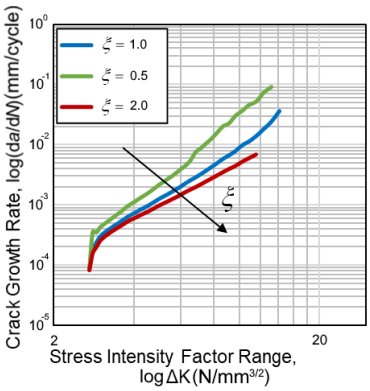

Fig. 4.49. ξ parameter influence on crack rate growth versus stress intensity factor change for fatigue degradation function $\hat{F}_3$

Chapter 5

Heterogeneous material numerical examples

Summary

In this chapter, the presented generalized phase-field fracture model is employed on the heterogeneous microstructural geometries obtained from the metallographic images of nodular cast iron from Čanžar [174]. This ductile nodular cast iron has a highly complex microstructure consisting of graphite nodules positioned in the ferritic matrix. The graphite nodules are modelled as perfectly circular holes, irregularly shaped holes or irregularly shaped inclusions with different material properties. The latter option is available through the coupled contact-fracture analysis, which is easily performed by the presented implementation. Different specimen sizes are drawn out of the metallographically obtained images. The specimens are thoroughly tested using the generalized phase-field fracture model in monotonic and cyclic tensile loading regimes, recovering corresponding brittle/ductile or fatigue material behaviour. The influence of the size, shape and arrangement of microconstituents is observed.

5.1. Nodular cast iron properties, specimen selection

The selected heterogeneous material is the nodular cast iron grade EN-GJS-400-18-LT investigated in Čanžar [174]. Fig. 5.1. shows its microstructure, in which the volume fraction of graphite nodules is approximately 7% with circularity of about 0.7 (a value of 1.0 indicates a perfect circle).

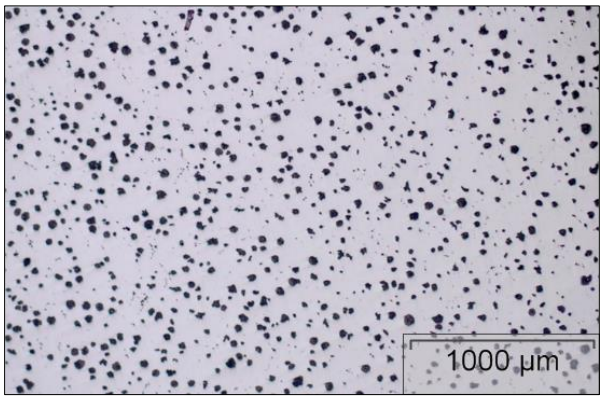

Fig. 5.1. Metallographic image of EN-GJS-400-18-LT microstructure [174]

Three different sample sizes (S, M, L) are randomly selected from the metallographic image to satisfy the average graphite nodules content of approximately 7%, as shown in Fig. 5.2. The length of Specimen M and L is increased 2 and 3 times, respectively, with regard to the length of Specimen S. The specimen sizes are shown in the legend.

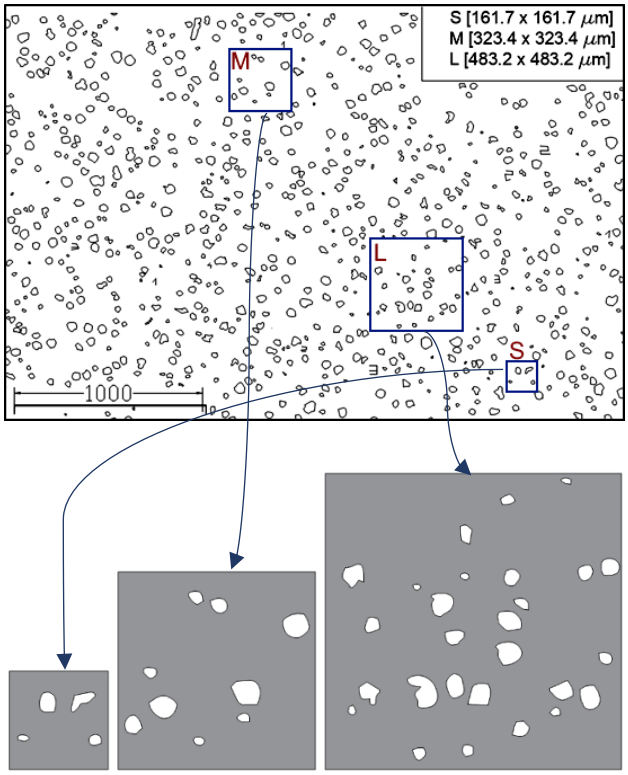

Fig. 5.2. Selection of different samples sizes satisfying the global average graphite nodules content

The specimens are then modelled in three different options ascending in the level of detail. First, the nodules are substituted with perfect spherical voids of the corresponding sizes. In the 2D settings, they are represented by circular holes. Secondly, the nodules are substituted with voids closely following the nodule geometry. Lastly, the nodules are modelled as inclusions with material properties corresponding to the graphite. These inclusions are connected to the matrix via the hard contact option, where the contact between the matrix void and the nodule surfaces is modelled using the penalty method with the friction coefficient value 0.2. The automatic stabilization of the nodule rigid body motion is introduced, activating the viscous damping at the interface nodes. However, as the damping energy is just a small fraction of the overall model energy, the influence of viscous damping on the system can be neglected. These options are hereafter called N1, N2 and N3, and are schematically presented in Fig. 5.3.

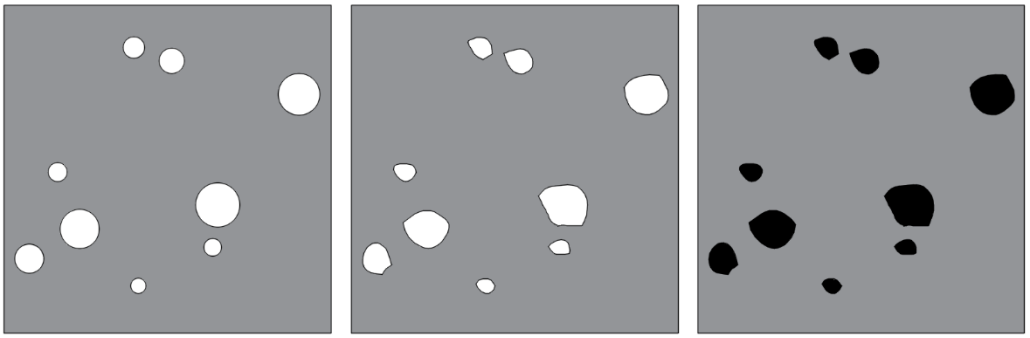

a) b) c)

Fig. 5.3. Schematical representation of nodule modelling options a) circular holes (N1), b) holes of corresponding to the nodule shape (N2), c) nodules as inclusions of corresponding shape (N3)

The samples, ascending in size, are uniformly discretized to retain the ratio $h/l < 0.5$, according to Miehe et al. [71], where h is the characteristic size of the finite elements. The FE mesh sizes for the specimens S, M and L with different nodule modelling options are shown in Table 5.1.

Table 5.1. Number of finite elements in the model

		Nodule modelling option		
		N1	N2	N3
Specimen size	S	26 691	27 144	31 924
	M	91 712	93 572	92 369
	L	199 121	556 291	329 409

Due to the absence of a more accurate material characterization of constituents at microlevel, which could be obtained by, e.g., the nanoindentation procedure, the nodular cast iron elastoplastic material properties at macrolevel, used in Section 4.3., are assigned to the matrix.

The nodule material properties are taken from [177] as the graphite material properties with the assumed purely elastic behaviour. Elastoplastic material properties for the modelled microstructural constituents are shown in Table 5.2.

Table 5.2. Elastoplastic material properties for each constituent

	E [GPa]	v [-]	σ_y^0 [MPa]	Q_∞ [MPa]	b [-]	C_1 [MPa]	γ_1 [-]	C_2 [MPa]	γ_2 [-]
Matrix	140	0.3	123	95	18	22,734	261.8	136,029	2,113.5
Nodule	5	0.3	1,000,000	*same*					

The length scale parameter is set to $l = 0.0025$ mm in order to match the small sample size. Accordingly, the matrix fracture toughness is set to $G_c^{\mathrm{M}} = 0.74$ N/mm, while the graphite nodule fracture toughness is assumed to be four times lower, i.e., $G_c^{\mathrm{N}} = 0.185$ N/mm.

To show the capability of the proposed generalized phase-field fracture model in modelling different fracture behaviour, fracture toughness is scaled down by two orders of magnitude, i.e., $G_c^{\mathrm{M}} = 0.002$ N/mm and $G_c^{\mathrm{N}} = 0.0005$ N/mm.

Lastly, it should be mentioned that the selected samples do not statistically represent the microstructural topology, as the amount of sampled material is too low to represent a statistical average arrangement of the constituents.

5.2. Monotonic loading - Brittle and ductile fracture material behaviour

The specimens are first subjected to monotonic tensile loading, as presented in Fig. 5.4. The periodic boundary conditions, frequently used in the microstructural analyses, are not considered here since the fracture process is generally non-periodic.

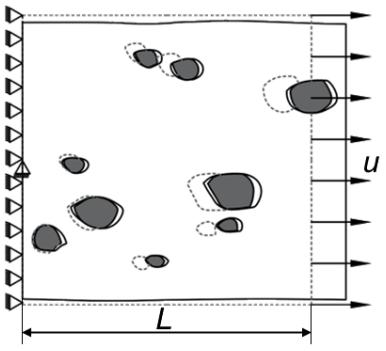

Fig. 5.4. Displacement boundary conditions

In the case of the tensile loading, tensile stresses play a dominant role in the model domain. For that reason, similar results can be obtained with the so-called isotropic material model, i.e. model without energy decomposition where $\psi_e^+ = \psi_e$ and $\psi_e^- = 0$. The corresponding stress-strain curves for both cases are obtained through the division of the resulting reaction force by the cross-sectional area $L \times 1$ and the division of the corresponding displacement by the specimen's length L. Similar procedure was conducted in [107].

Note again that, the generalized model used in this subsection is capable of recovering fatigue fracture. However, due to the careful description of energy density accumulation variable in Section 2.3.1., there is no influence of fatigue during the monotonic loading.

5.2.1. Ductile material behaviour

The comparison between the results obtained with different nodule modelling options on different specimen sizes is shown in Fig. 5.5 - Fig. 5.7.

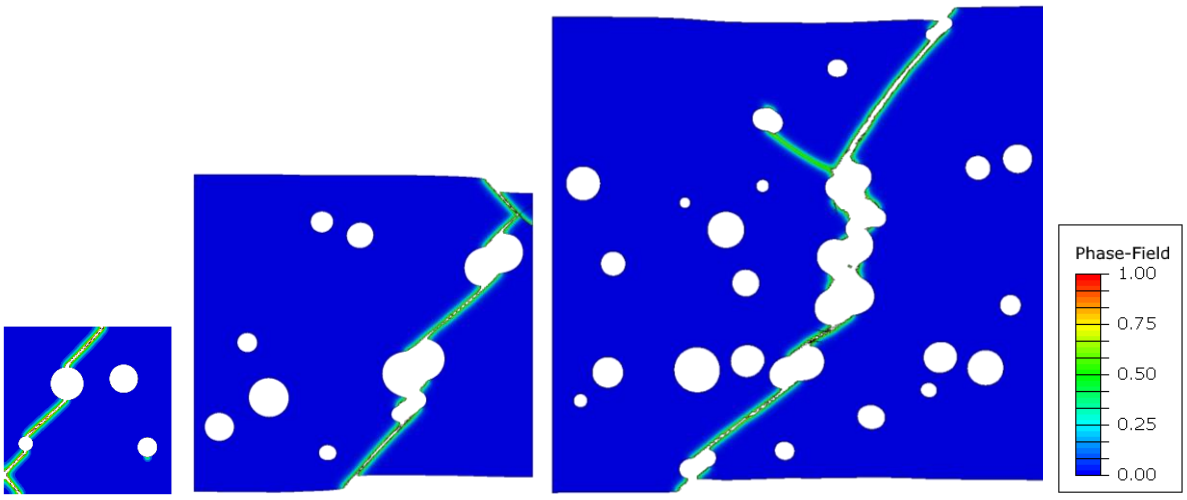

a) b) c)

Fig. 5.5. Monotonic loading. Ductile fracture pattern obtained on N1 nodule modelling option on specimen sizes a) S, b) M, and c) L

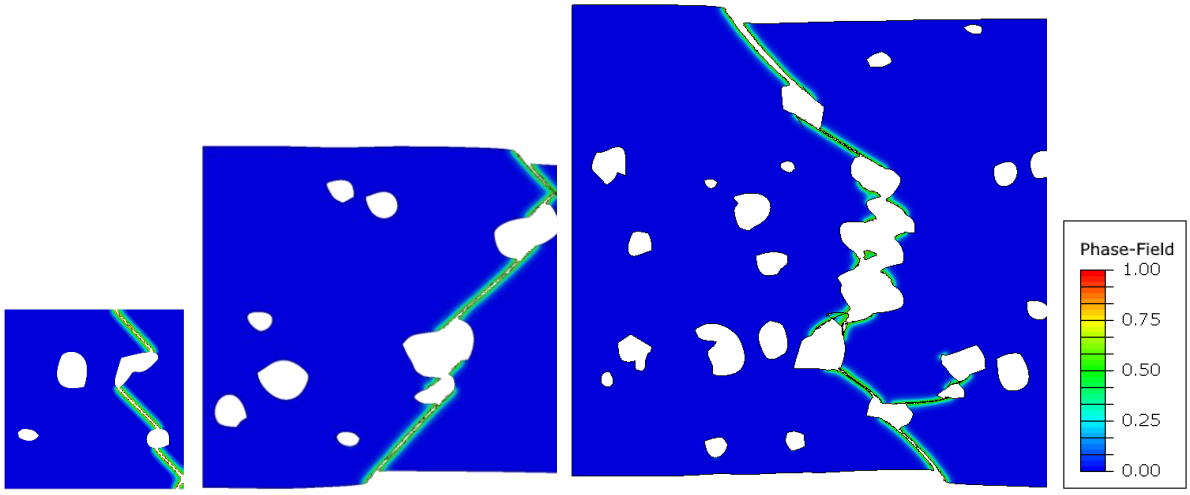

a) b) c)

Fig. 5.6. Monotonic loading. Ductile fracture pattern obtained on N2 nodule modelling option on specimen sizes a) S, b) M, and c) L

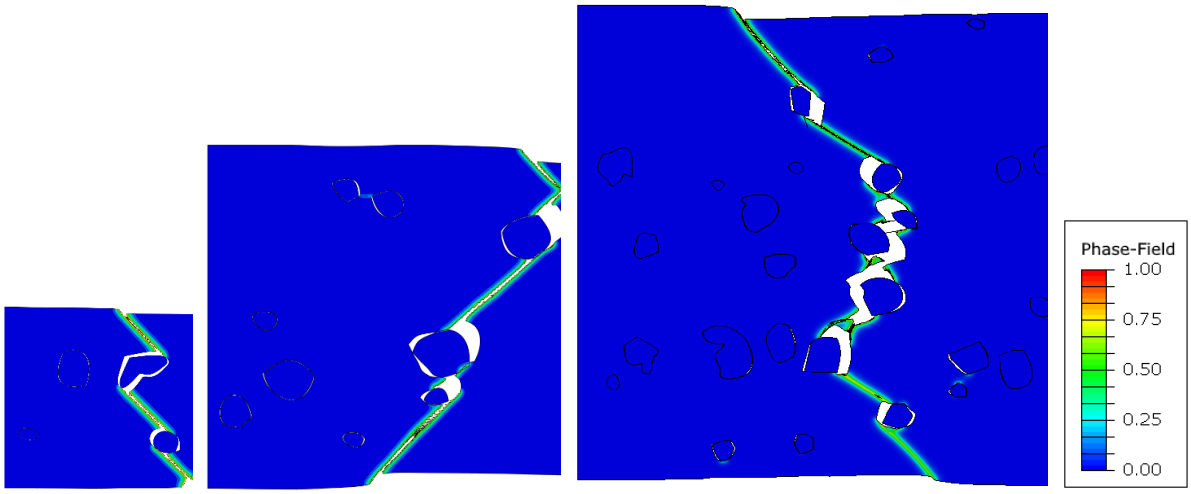

a) b) c)

Fig. 5.7. Monotonic loading. Ductile fracture pattern obtained on N3 nodule modelling option on specimen sizes a) S, b) M, and c) L

Obvious ductile fracture pattern can be observed, with 45° incline with respect to the loading direction. Moreover, the crack paths obtained by the N2 and N3 nodule modelling options are exceptionally close, while there are some discrepancies in comparison with N1. The respective stress-strain curves are shown in Fig. 5.8.

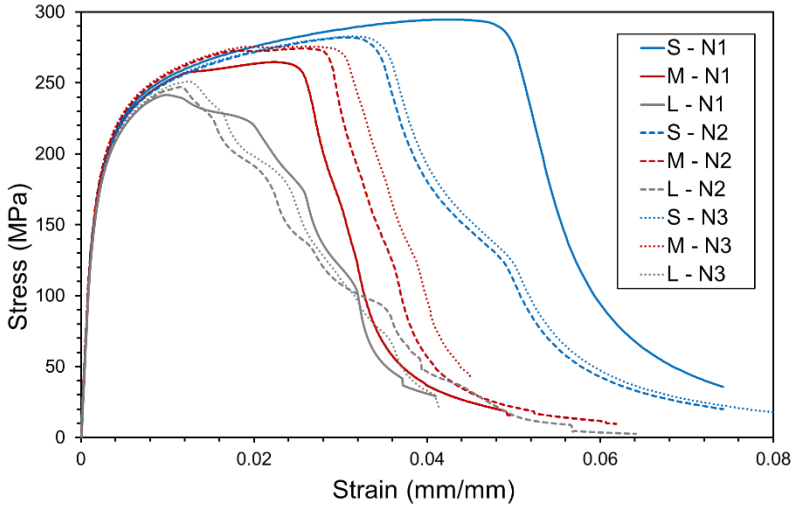

Fig. 5.8. Monotonic loading. Stress-strain response for different nodule modelling options and specimen sizes

As evident, the peak stress and strain values, at which the failure occurs, drop with the increase in the specimen size, thus clearly displaying the well-known size-effect. On the other hand, the difference in structural response due to the nodule modelling is somewhat inconclusive. Modelling nodules as real inclusions (N3) yields close results to the irregularly shaped void modelling option (N2). The option N3 is slightly, but consistently, stiffer and more resilient than N2 on every specimen size. However, the option with the perfect circular holes (N1) instead of the nodules yields different results. While it gives much stiffer and more resilient response than N2 and N3 on the smallest specimen size S, as is expected, this is not the case for specimen sizes M and L. The reason of such behaviour could be the nodule orientation. Coincidentally, the prevailing irregular nodule shape orientation (N2 and N3) seems to be generally parallel to the loading direction in specimen M and L, thus increasing the load-bearing capacity in comparison to the perfectly circular hole substitution (N1). Therefore, most of the sharp notches are also not stress-concentrators in this loading setup, which explains why, in some cases, the N1 option yields stiffer response, contrary to the initial expectation.

To prove that the proposed model can handle monotonic loading without the interference of the fatigue extension, the energy density accumulation variable $\bar{\psi}$, together with total energy $\left(\psi_{\mathrm{e}}+\psi_{\mathrm{p}}\right)$, is shown in Fig. 5.9, for the specimen S with nodule modelling option N1. Three timeframes are shown: frame where no damage has started yet, mid-frame where the localization bands have formed, and the final fracture frame.

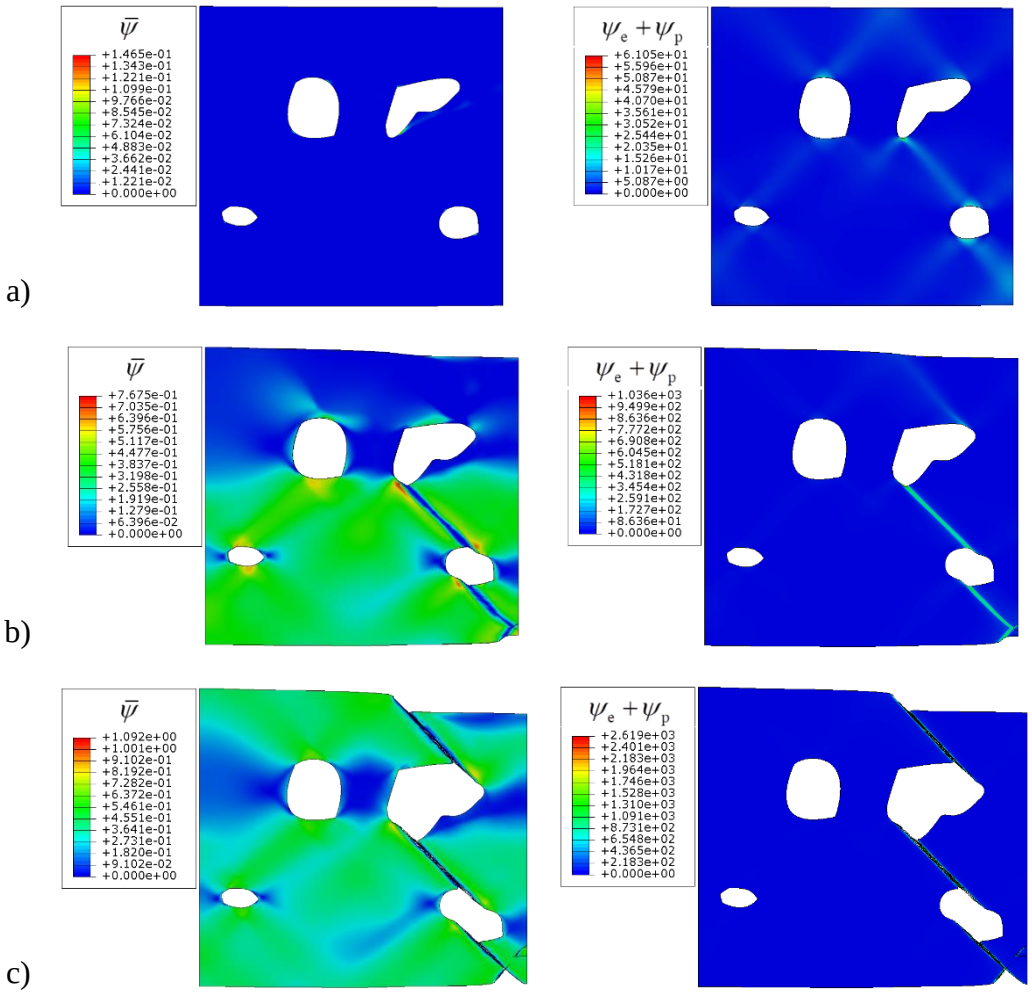

Fig. 5.9. Monotonic loading. Total energy density and energy density accumulation variable plot at timeframes when a) no damage have yet started, b) the localization bands have formed c) final fracture frame occurs

The energy density accumulation variable $\bar{\psi}$ obviously increases at the locations where total energy, i.e., elastic energy density decreases. The increase is negligible compared to the value of total energy density at the corresponding points. Moreover, the locations with high total energy density, corresponding to the localization of damage, do not exhibit the energy density accumulation variable increase. Therefore, this proves that the proposed model can handle monotonic loading case without the interference of the extension, which was not the case with previous phase-field fatigue extensions [120]. This can be further proven by comparing the stress-strain curves of the model with no fatigue degradation function with the models containing the fatigue function $\hat{F}$. The comparison is presented in Fig. 5.10. where three different $\bar{\psi}_\infty$ values are used.

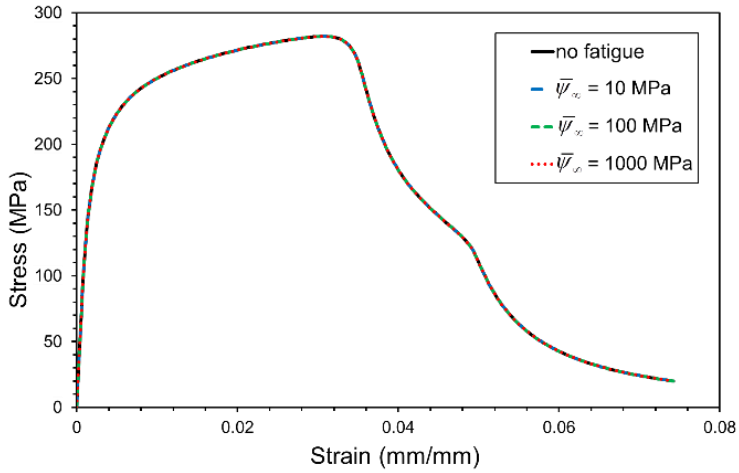

Fig. 5.10. Monotonic loading. Influence of the fatigue extension

No difference between the models with and without the fatigue degradation function $\hat{F}$ can be observed. Thus, it can be concluded the proposed fatigue extension does not interfere with the monotonic fracture analysis.

5.2.2. Brittle material behaviour

The same tests are now repeated with the lower fracture toughness, as explained in Section 5.2.1. The elastoplastic material model remains unchanged. Fig. 5.11. - Fig. 5.13. present the comparison between the results obtained with different nodule modelling options on different specimen sizes for such material properties.

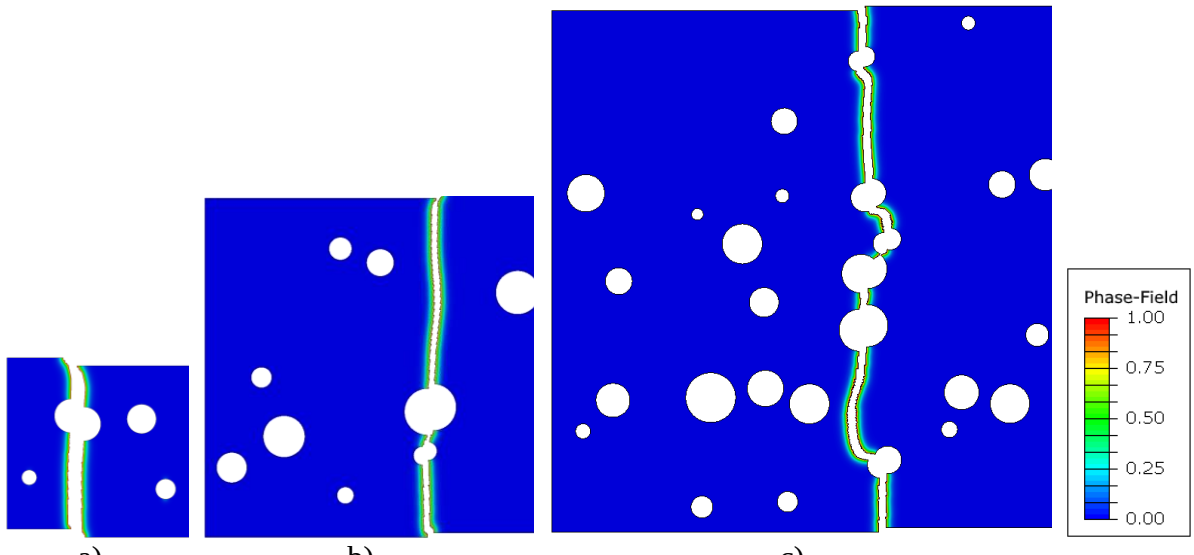

Fig. 5.11. Monotonic loading. Brittle crack pattern obtained with N1 nodule modelling option on different specimen sizes (scale factor 20 is applied for better visualization)

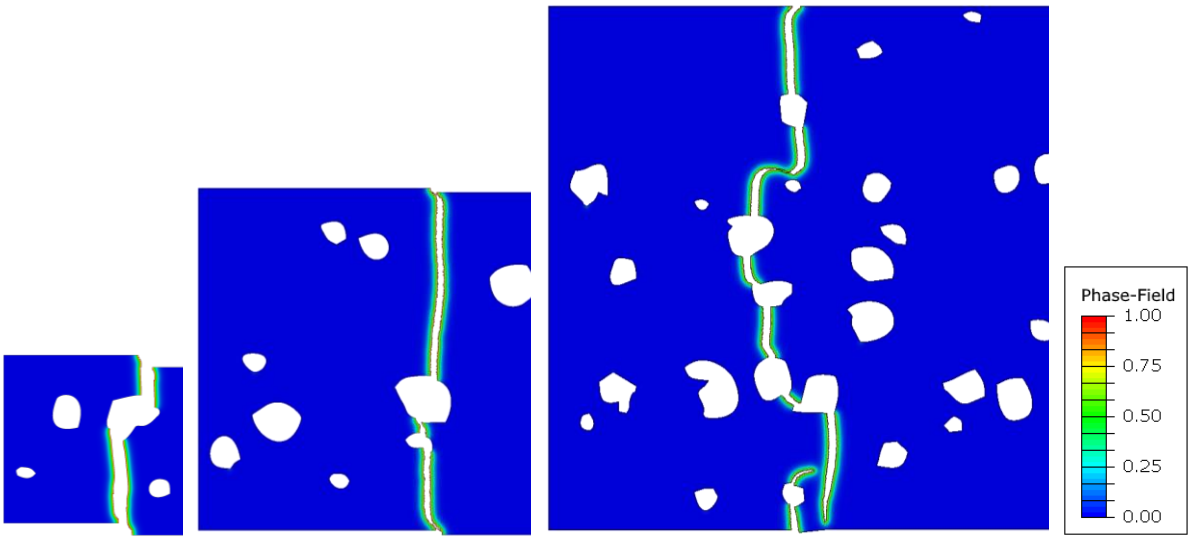

a) b) c)

Fig. 5.12. Monotonic loading. Brittle crack pattern obtained with N2 nodule modelling option on different specimen sizes (scale factor 20 is applied for better visualization)

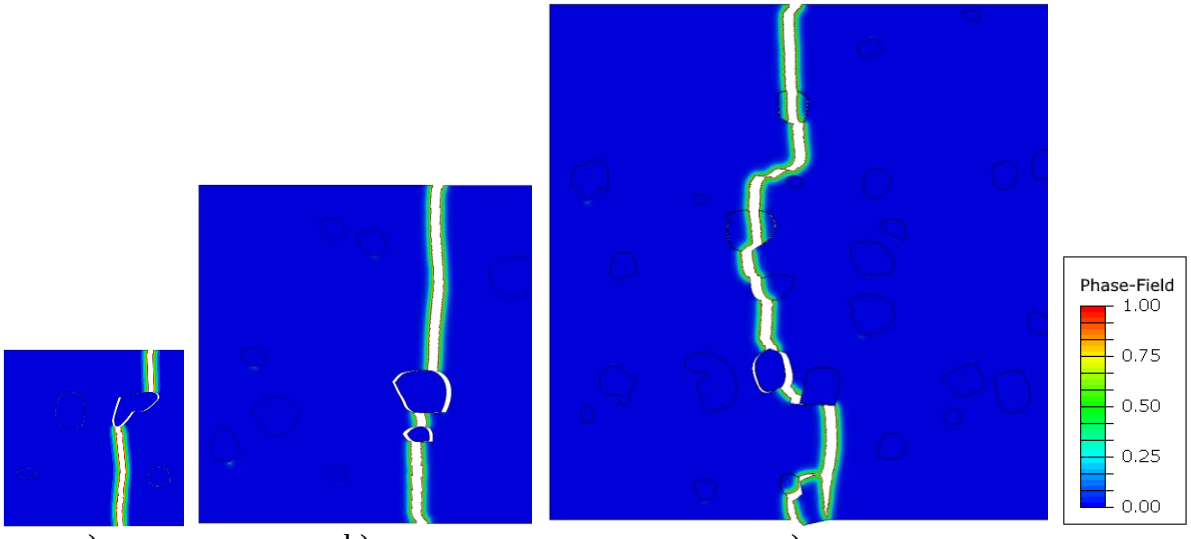

a) b) c)

Fig. 5.13. Monotonic loading. Brittle crack pattern obtained with N3 nodule modelling option on different specimen sizes (scale factor 20 is applied for better visualization)

In this case, brittle fracture patterns are observed as expected. Analogously to the previous examples, the crack patterns obtained with the N2 and N3 nodule modelling option are very similar, while there are some differences with respect to the N1 modelling option. Interestingly, in the N3 modelling option, occasionally the crack propagates across the nodules showing both intra- and trans-granulate fracture. The respective stress-strain curves are shown in Fig. 5.14.

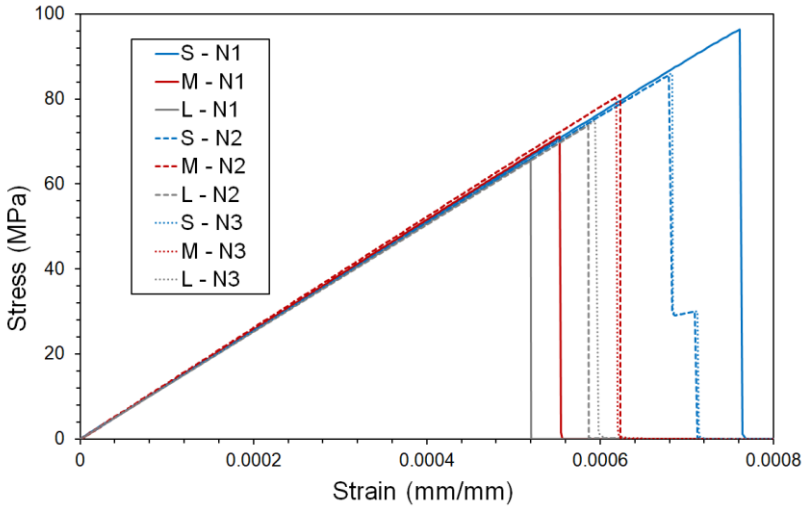

Fig. 5.14. Monotonic loading. Stress-strain response for different nodule modelling options and specimen sizes

The obtained structural response is analogous to the previously considered ductile fracture behaviour. In this case, a clear, sharp stress drop is observed, characteristic for the brittle fracture cases analysed in this work. Moreover, a certain size-effect is again observed. The influence of the nodule modelling options shows similar behaviour as in the previous example dealing with the ductile fracture. However, the explanation provided there can be more clearly observed on the curve slopes. It is evident that, while the modelling option N1 yields a bit steeper slope (thus also the stiffer response) for specimen S, the slope is less steep for specimens M and L.

5.2.3. Brittle-ductile transition

The proposed phase-field fracture model can clearly reproduce both brittle and ductile fracture behaviour, depending on the values of fracture material properties and the plastic yield limit. To further test this, the parametric study is conducted by changing the fracture toughness G_c. The smallest specimen size S is used together with the nodule modelling option N2.

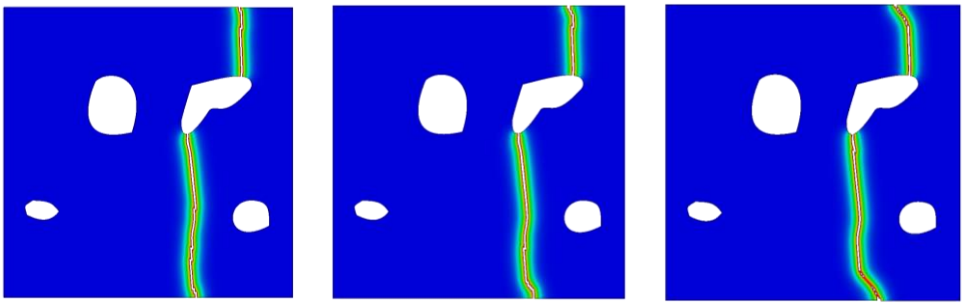

a) b) c)

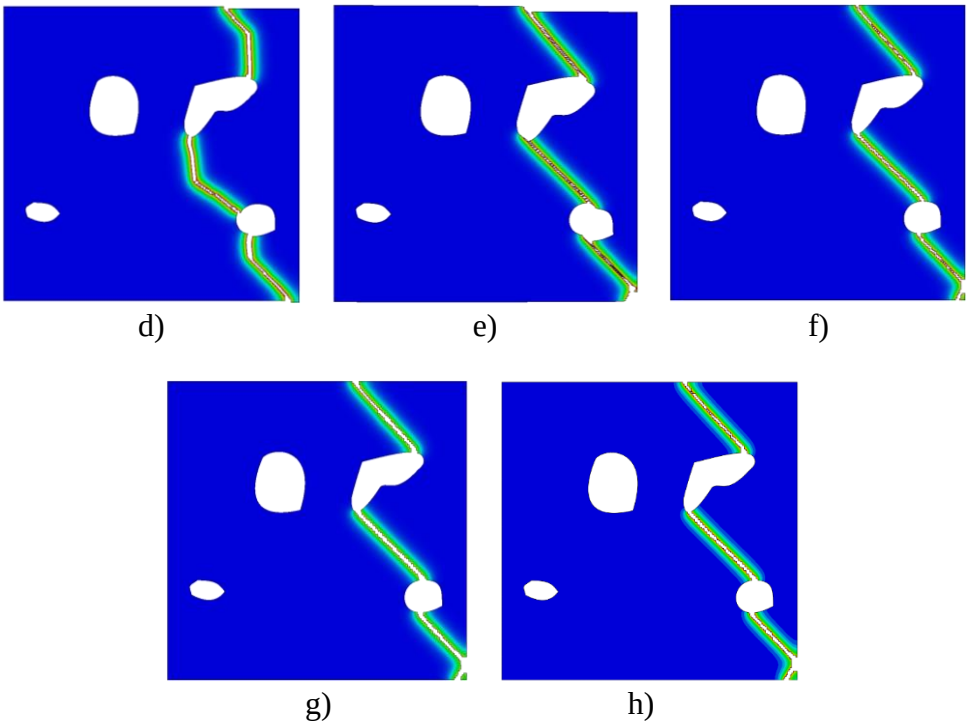

Fig. 5.15. Monotonic loading. Crack paths obtained on specimen S with N2 with a) $G_c = 0.001$ N/mm, b) $G_c = 0.002$ N/mm, c) $G_c = 0.005$ N/mm d) $G_c = 0.01$ N/mm, e) $G_c = 0.1$ N/mm, f) $G_c = 0.25$ N/mm, g) $G_c = 0.45$ N/mm, and h) $G_c = 0.74$ N/mm

The obtained results show the clear transition between the brittle and ductile fracture patterns depending on the change in the material fracture properties. The corresponding stress-strain curves are shown in Fig. 5.16.

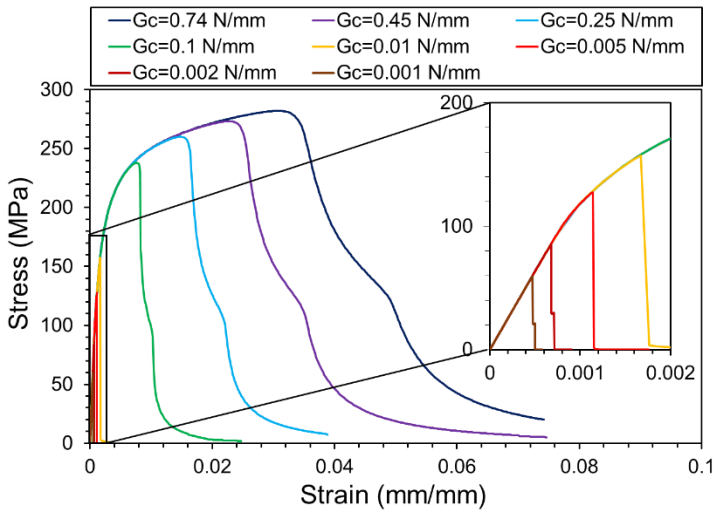

Fig. 5.16. Monotonic loading. Stress-strain response comparison for different values of fracture toughness

The ability of the proposed model to recover both brittle and ductile material behaviour, as well as the transition between, is clearly shown.

5.3. Cyclic loading - Fatigue fracture material behaviour

The specimen S with the nodule modelling option N2 is subjected to the cyclic displacement-controlled loading with 6 different amplitudes, namely, u_1 = 0.001 mm, u_2 = 0.00075 mm, u_3 = 0.0005 mm, u_4 = 0.00035 mm, u_5 = 0.0002 mm, u_6 = 0.0001 mm with R = 0. The fatigue function $\hat{F}_3$ is used with the fatigue parameter $\bar{\psi}_\infty = 500$ MPa. The corresponding force-displacement curves are shown in Fig. 5.17.

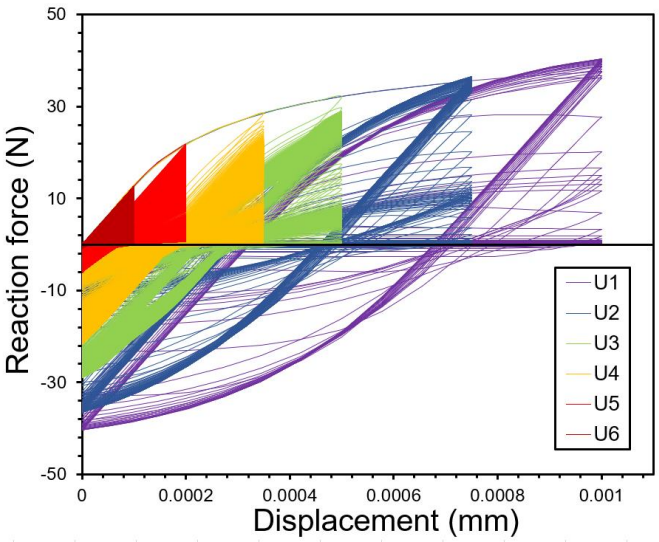

Fig. 5.17. Cyclic loading. Force-displacement curves

It is obvious that the case with the load amplitude u_1 yields plastic response with clear hysteresis loops. The cases with load amplitudes u_2 and u_3 produce similar behaviour. However, the hysteresis area is significantly lower, allowing for the higher number of loading cycles. Furthermore, as the load amplitudes decreases, the models exhibit less and less plasticity making the transition towards the high-cyclic regime. The case with load amplitude u_6 thus shows clear elastic behaviour with negligible influence of plastic deformations.

The corresponding fracture patterns are plotted in Fig. 5.18. at three different timeframes.

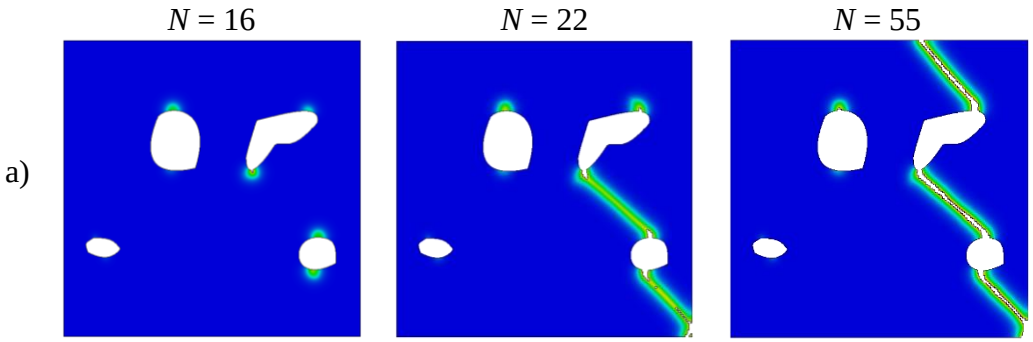

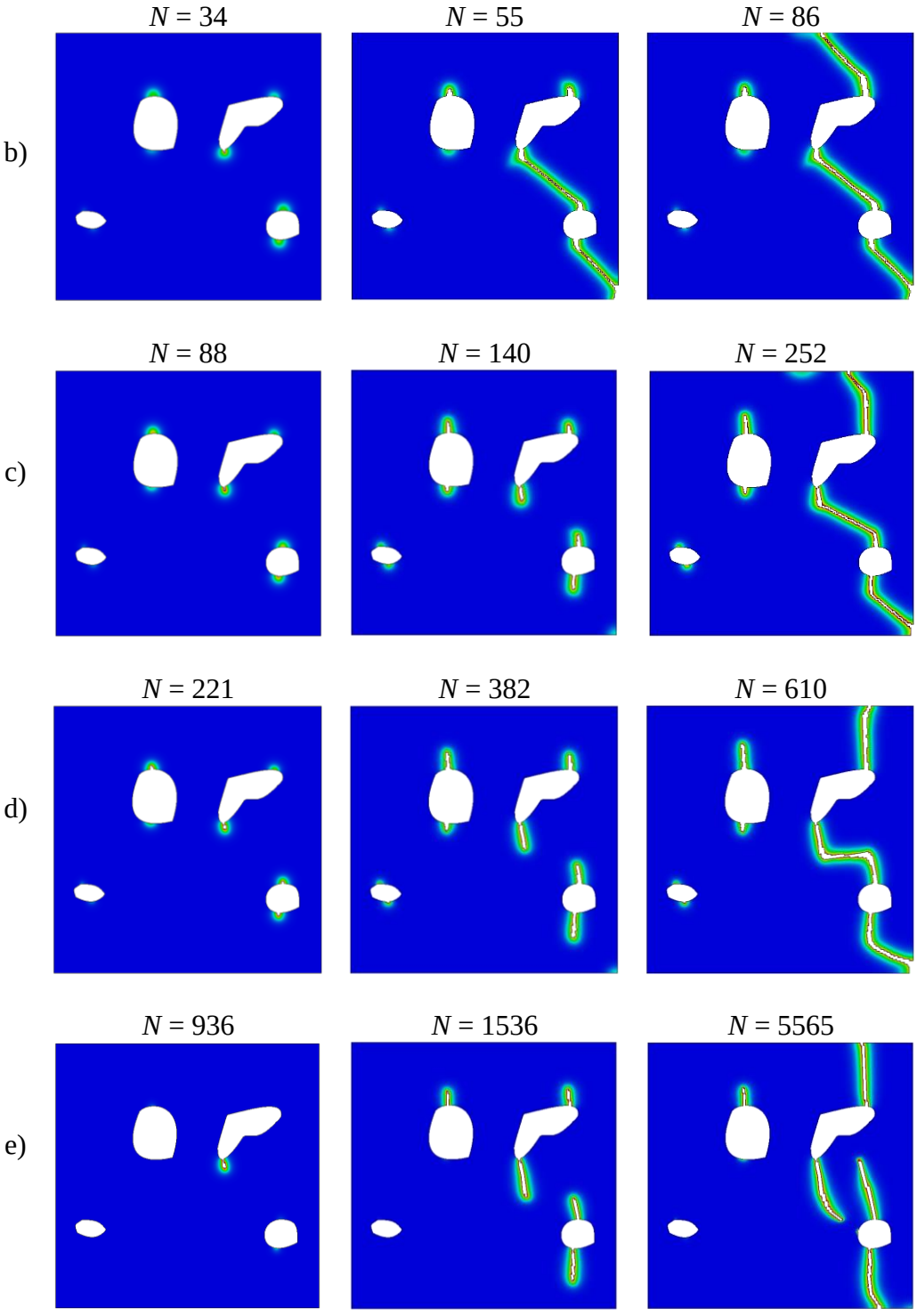
N = 34
N = 55
N = 86
b)
N = 88
N = 140
N = 252
c)
N = 221
N = 382
N = 610
d)
N = 936
N = 1536
N = 5565
e)

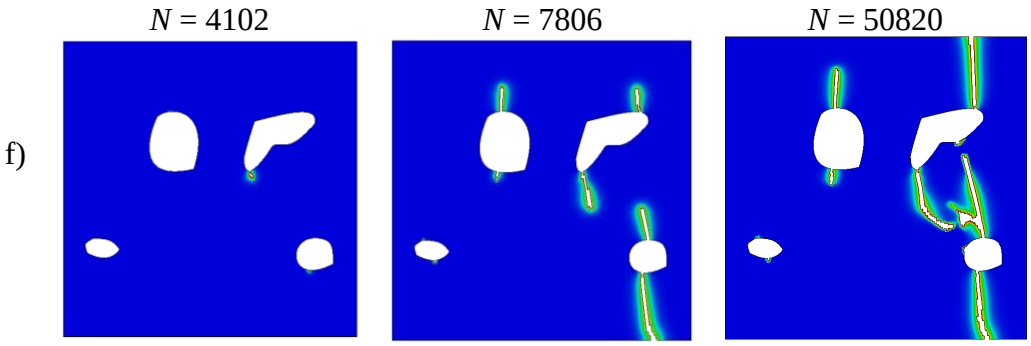

Fig. 5.18. Cyclic loading. Evolution of fatigue fracture for displacement amplitudes a) u_1 = 0.001, b) u_2 = 0.00075, c) u_3 = 0.0005, d) u_4 = 0.00035, e) u_5 = 0.0002, and f) u_6 = 0.0001

The case with the highest amplitude follows previously shown ductile fracture pattern, with 45° incline towards the loading direction. On the other hand, the lowest amplitude case has a fracture pattern following 90° incline, with the cases in-between showing a clear transition between regimes. The transition between the low- and high-cycle fatigue can thus be clearly seen. Moreover, as expected, the cases corresponding to higher load amplitudes, and thus more plasticity within the model, exhibit the total failure sooner. It is presented by a Wöhler curve in Fig. 5.19. with the displacement amplitudes on the *x*-axis.

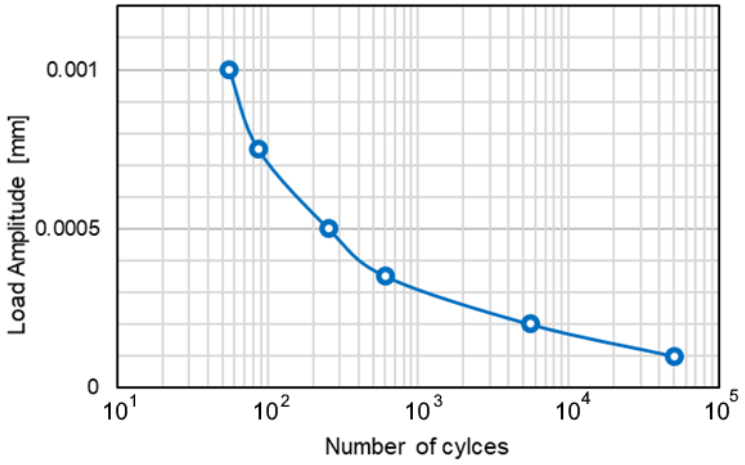

Fig. 5.19. Cyclic loading. Wöhler curve

Chapter 6

Conclusion

The prediction and prevention of material failure at a component design stage is an important aspect of modern-day engineering, with numerical simulations gradually becoming a primary method of choice. While the assumption of the material macrohomogeneity is often still valid in engineering practice, the prediction of fracture in advanced heterogeneous materials requires the consideration of material microheterogeneity and its influence on the macrobehaviour. Material failure is essentially a multiscale phenomenon. Macroscopic cracks are a direct result of the cascade of complex fracture processes happening at the microstructural level. While the multiscale methods open the way to the future multiscale fracture modelling, there still seems to be a long way before they can be consistently and reliably applied in realistic structural problems. Therefore, the development of a reliable numerical damage and fracture analysis method, considering material microstructural properties and topology, is crucial for the assessment of structural integrity, reliability, and component lifetime in modern structures and machine components. In turn, such method can assist in the development of advanced materials with enhanced properties coming from the desired microstructure, and enable the production of more efficient, safer and cheaper structures.

The most commonly used numerical fracture modelling methods introduce the crack as a sharp geometrical discontinuity. Along with the additional criteria for crack initiation, propagation or growth direction required in these discrete crack modelling methods, a major problem arises with the numerical tracking of the crack discontinuities. It can present significant implementation difficulties in the three-dimensional settings. The diffusive crack modelling approaches, introducing a damage parameter which controls the material stiffness and stress

release associated with the crack formation, pose as an alternative. The phase-field fracture method, which recently became a very popular diffusive fracture modelling method, is capable of successfully recovering the complex fracture processes occurring at the microstructural level, without introducing any *ad hoc* criteria. A length-scale parameter is introduced, similarly to other diffusive crack modelling approaches. Although extensive research has been carried out on the development of phase-field fracture theory, certain challenges still exist in the computational implementation of the method and have been dealt with in this thesis.

The generalized phase-field framework for brittle, ductile and fatigue fracture modelling has been developed and implemented into the commercial FE software ABAQUS. Two different phase-field formulations were included, affecting the (linear-)elastic structural response stage before the onset of crack. Moreover, different plasticity models, including the combined nonlinear isotropic-kinematic hardening model were also included. The staggered solution scheme with the stopping criterion based on the control of residual norm was developed and implemented within the framework, improving the convergence rate. The implementation of the algorithm was the first such implementation of an iterative phase-field fracture solution scheme in the ABAQUS software. The non-convexity of the underlying free energy functional, usually posing implementation problems concerning numerical instabilities, was thus tackled. The solution scheme was thoroughly tested and confirmed to be robust and more efficient in comparison with the commonly used single iteration staggered phase-field fracture algorithm. In contrast to the single iteration algorithm, the accuracy is no longer dependent on the careful selection of the size of loading increments, while the CPU time demand is substantially decreased. The importance of the stopping criterion within a staggered scheme was shown by illustrative examples.

The thread-parallelization and the element deletion option were introduced to reduce the common phase-field problem of high computational cost. The use of different ABAQUS solvers allows the calculation of both displacement- and force-controlled problems. The implementation is capable of calculating coupled contact-fracture problems. The cycle skipping technique was implemented to allow for the calculation of a very high number of loading cycles in the fatigue analysis on moderate size examples. Additional options available within this implementation, showing the great advantages of commercial FE software implementation, included the automatic incrementation and restart analysis options. Different element formulations in 1D, 2D and 3D were considered. The full source code together with

the examples presented in this thesis, tutorials and steps to reproduce was made publicly available to other researchers, students and engineers, thus promoting the phase-field fracture methodology. It is available on: https://data.mendeley.com/datasets/p77tsyrbx2/4

The developed framework was proven capable of accurately reproducing brittle/ductile or fatigue fracture, according to the underlying material behaviour and loading conditions. This capability was tested on examples ascending in complexity. Accordingly, a detailed discussion on the accuracy of results and analysis duration was provided. First, the framework was successfully verified and validated on the monotonically loaded examples of various materials exhibiting brittle fracture with the assumption of elastic homogeneous material behaviour. Benchmark examples with numerical and experimental results reported in literature were considered, including homogeneous plate, single edge notched plate subjected to tensile and shear loading, L-shaped beam and asymmetrically notched perforated three-point bending test specimen. The energy decompositions, preventing the unphysical crack propagation in compressive state, were tested. Moreover, the force-controlled loading and thread-parallelization options were tested within these examples, showing great advantages of the proposed framework. The monotonically loaded examples of steel and aluminium alloys exhibiting ductile fracture behaviour were considered next. The comparison was made with the experimental data in terms of force-displacement curves, crack and plastic deformation evolution patterns. The examples included V-notch bar, asymmetrically notched tensile specimen and Sandia challenge CT specimen. The capabilities of the implementation in 3D settings were shown here. Finally, the fracture analysis in homogeneous material behaviour was concluded by cyclically loaded round bar and CT specimen examples. The cyclic elastoplastic model and the obtained crack growth rate were successfully validated in comparison with experimental results from literature. Special attention was given to the verification of the fatigue part of the generalized framework through the parametric study. Therein, the influence of load ratio R, fatigue and fracture material properties is thoroughly tested. The parameters corresponding to the material fatigue properties were clearly linked to the well-known empirical parameters. Main features of fatigue, including Wöhler and Paris law curves in low- and high-cycle regimes, were easily recovered without any additional criteria.

Finally, realistic heterogeneous microstructure of nodular cast iron obtained from microtomography was tested. This highly complex microstructure consists of graphite nodules positioned in the ferritic matrix. Different-sized 2D samples were randomly selected from the

metallographic image to satisfy the average graphite nodules content of 7%. Three nodule modelling options differing in the level of detail were tested. The nodules were substituted with perfect circular voids of the corresponding sizes, voids closely following the actual nodule geometry, and inclusions with material properties corresponding to the graphite. Last option showed the ability of the implementation in handling coupled contact-fracture problems. Specimens were tested in both monotonic and cyclic loading regimes. The capability of the proposed framework in handling monotonic loading case without the interference of the fatigue extension was proven. The results showed clear size-effect behaviour as well as the influence of microstructural topology, i.e., the size, shape and distribution of the microconstituents on fracture patterns. The transition between the brittle and ductile fracture patterns was shown by a parametric study where fracture toughness property was intermittently changed. Lastly, the heterogeneous specimens were subjected to the cyclic loading and exhibited low- and high-cyclic fatigue fracture patterns, and the transition in-between.

Original scientific contributions to the field of computation fracture mechanics include:

1. Development of the novel generalized phase-field fracture model capable of recovering brittle/ductile or fatigue fracture patterns, following the underlying material behaviour and loading scenario

    - A novel description of energy density accumulation variable is introduced allowing the accurate monotonic fracture analysis without the influence of the fatigue extension. Only one additional parameter is included into the fatigue extension of the model, and is clearly linked to the well-known empirical parameters through the parametric analysis. The cycle skipping technique is implemented allowing high cycle number calculation on moderate size examples.

    - Different phase-field formulations affecting the (linear-) elastic material behaviour stage, before the onset of crack, are included together with a few different plasticity material models to account for the ductile fracture behaviour, as well as cyclic plasticity in low-cyclic fatigue regime.

    - The proposed model was thoroughly tested, verified and validated in comparison with numerical and experimental results from literature. Main features of fatigue, including Wöhler and Paris law curves in low- and high-cycle regimes, were easily recovered without any additional criteria.

2. Development of the staggered iterative solution scheme with residual norm control-based stopping criterion to tackle numerical efficiency and stability

    - The algorithm is thoroughly tested in comparison with commonly used single iteration staggered phase-field fracture algorithm. Detailed discussion on the accuracy of results and analysis duration is given.

    - In contrast to the single iteration algorithm, the accuracy is no longer dependent on the careful selection of the loading increment size, while the CPU time demand is substantially decreased.

    - The importance of the stopping criterion within a staggered scheme was emphasized.

3. The potential of the proposed model in modelling of the complex brittle, ductile and fatigue fracture processes, is thoroughly examined by the fracture analysis of real heterogeneous microstructural geometries of nodular cast iron obtained by metallography procedure.

    - The different specimen sizes are tested clearly observing the size-effect behaviour corresponding to the verified results reported in the literature. Three possibilities of nodule modelling differing in the level of detail were investigated, including the modelling of nodules as inclusions with graphite properties within the ferritic matrix. This option showed the capability of the proposed implementation in solving contact problems.

    - The influence of the microstructural topology, i.e., the size, shape and distribution of the microconstituents is clearly shown in the numerical examples. The proposed model can easily handle complex fracture processes, including crack initiation, localization, propagation, merging and branching, occurring at the microstructural scale.

    - Parametric study was conducted showing the effects of fracture toughness on the transition between brittle and ductile fracture patterns, within the proposed model. The cyclic loading examples show great potential of the proposed model to resolve fatigue fracture in both high- and low-cyclic regime. Clear transition between low- and high-cyclic fatigue fracture patterns was observed.

The future work on the proposed model includes the extension and upgrade of the implementation framework. The extension to the large-strain settings and a complete thread-parallelization should be the first step. Different finite element formulations, like tetrahedral or axisymmetric, could be considered. Other material models, e.g. Neo-Hooke, can also be straightforwardly introduced. Upon proper validation, the fatigue extension within the

proposed model should be upgraded and improved. The included cyclic jump technique should be thoroughly tested.

From the point of view of the general phase-field fracture theory, the phase-field fracture methodology should be extensively experimentally validated to become a true alternative for the fracture analysis of real-life structural components. The solution non-uniqueness coming from the numerical handling of the non-convexity of the underlying free energy functional, and irreversibility of the crack phase-field parameter, should be investigated further. A better-performing energy decomposition preventing the unphysical crack propagation in compressive state should be researched.

Finally, coupling the implementation with the ABAQUS local remeshing algorithm would solve the important problem of phase-field fracture models - high computational cost. Moreover, the proposed framework could be included into a multiscale framework, thus allowing the fracture analysis larger scale model while simultaneously considering actual microstructural topologies.

ŽIVOTOPIS

Karlo Seleš rođen je u Koprivnici, 8. ožujka 1993. Osnovnu školu pohađao je u Đurđevcu, gdje je 2007. godine upisao opću gimnaziju. 2011. godine upisuje Fakultet strojarstva i brodogradnje na Sveučilištu u Zagrebu, na kojem je 2016. godine diplomirao s najvišom pohvalom (summa cum laude). Dobitnik je Rektorove nagrade za individualni znanstveni i umjetnički rad 2016. godine koji je zajedno s Denisom Pevecom izradio u sklopu znanstveno-istraživačkog projekta „GT Exhaust System Enhanced Design“ provedenog u suradnji Fakulteta strojarstva i brodogradnje Sveučilišta u Zagrebu i tvrtke Alstom. Dobitnik je i Sveučilišne stipendije za izvrsnost 2016. godine te nagrade HEP-a d.d. 2015. godine. Jedan semestar diplomskog studija proveo je na Erasmus+ studentskoj razmjeni na Tehničkom sveučilištu u Münchenu. Od studenog 2016. godine zaposlen je na Fakultetu strojarstva i brodogradnje Sveučilišta u Zagrebu na Zavodu za tehničku mehaniku kao asistent na HRZZ projektu „Višerazinsko numeričko modeliranje deformiranja materijala od makro do nanorazine. Dobitnik je nagrade društva sveučilišnih nastavnika i drugih znanstvenika u Zagrebu mladim znanstvenicima i umjetnicima u 2019. godini. Proveo je četiri tjedna na znanstvenom usavršavanju na Tehničkom sveučilištu u Braunschweigu i sudjelovao na ljetnoj školi „Mesoscale Models: from Micro-Physics to Macro-Interpretation“ održanoj u Italiji. Autor je četiri članka objavljena u časopisima indeksiranim u CC bazi podataka, te osam konferencijskih članaka od kojih je pet međunarodno recenzirano, a dva su objavljena u međunarodnim časopisima indeksiranim u SCOPUS bazi.

CURRICULUM VITAE

Karlo Seleš was born on March 8, 1993 in Koprivnica. He attended primary and grammar school in Đurđevac. In 2011 he enrolled Faculty of Mechanical Engineering and Naval Architecture at the University of Zagreb, where he graduated with the highest honours (summa cum laude) in 2016. He received Rector's Award for individual scientific and artistic work in 2016, within the scientific research project "GT Exhaust System Enhanced Design" done in collaboration with the Faculty of Mechanical Engineering and Naval Architecture, University of Zagreb and Alstom. He also received the University Scholarship for Excellence in 2016 and the HEP plc award in 2015. He spent one semester of graduate study on an Erasmus + student exchange at the Technical University of Munich. Since November 2016, he has been employed at the Institute of Applied Mechanics, Faculty of Mechanical Engineering and Naval Architecture, University of Zagreb as a research assistant in scope of the project financed by the Croatian Science Foundation, named “Multiscale Numerical Modeling of Material Deformation Responses from Macro- to Nanolevel”. He received the award of the Society of University Teachers and Other Scientists in Zagreb for young scientists and artists in 2019. He spent four weeks in scientific training at the Technical University of Braunschweig and participated in the summer school "Mesoscale Models: From Microphysics to Macro-Interpretation" held in Udine, Italy. He authored 4 CC published scientific papers and 8 conference articles, 5 of which were internationally peer-reviewed, and 2 were published in an international journal indexed in the SCOPUS database.

LIST OF PUBLICATIONS

CROSBI: https://www.bib.irb.hr/profile/33879,

Google Scholar: https://scholar.google.com/citations?hl=en&user=_G84l0cAAAAJ

Declaration: Parts of the work presented in this Dissertation have been published in some of the articles listed below.

List of CC Scientific Journal Papers:

- Seleš, K., Lesičar, T., Tonković, Z., Sorić, J. *A Residual Control Staggered Solution Scheme for the Phase-Field Modeling of Brittle Fracture*, Engineering fracture mechanics, 205 (2018), 1; 370-386. doi: 10.1016/j.engfracmech.2018.09.027.

- Seleš, K., Perić, M., Tonković, Z., *Numerical simulation of a welding process using a prescribed temperature approach*, Journal of constructional steel research, 145 (2018), 49-57 doi: 10.1016/j.jcsr.2018.02.012.

- Seleš, K., Jurčević, A., Tonković, Z., Sorić, J. *Crack Propagation Prediction in Heterogeneous Microstructure Using an Efficient Phase-Field Algorithm*, Theoretical and applied fracture mechanics, 100 (2019), 289-297 doi: 10.1016/j.tafmec.2019.01.022.

- Perić, M., Seleš, K., Tonković, Z., Lovrenić-Jugović, M., *Numerical simulation of welding distortions in large structures with a simplified engineering approach*, Open Physics, 17 (2019), 719-730 doi: 10.1515/phys-2019-0076.

- Seleš, K., Aldakheel, F., Tonković, Z., Sorić, J., Wriggers, P., *A General Phase-Field Model for Fatigue Failure in Brittle and Ductile Solids*, (under review).

List of Scientific Papers in Other Databases (SCOPUS):

- Seleš, K., Lesičar, T., Tonković, Z., Sorić, J., *A Phase Field Staggered Algorithm for Fracture Modeling in Heterogeneous Microstructure*, Key Engineering Materials, 774 (2018), 632-637 doi: 10.4028/www.scientific.net/kem.774.632.

- Seleš, K., Tonković, Z., Jurčević, A., Sorić, J., *Strain Energy Decomposition Influence in the Phase Field Crack Modelling at the Microstructural Level of Heterogeneous Materials*, Key Engineering Materials, 827 (2019), 482-487 doi: 10.4028/www.scientific.net/KEM.827.482.

List of International Scientific Conference Papers:

- Seleš, K., Lesičar, T., Tonković, Z., Sorić, J., *Phase-field solution scheme for fracture in heterogeneous microstructure*. The 6th International Conference on CRACK PATHS (CP 2018, Verona, Italy, (2018) 637-642.

- Seleš, K., Lesičar, T., Tonković, Z., Sorić, J., *Residual Control Phase-field Staggered Algorithm for Brittle Fracture Modelling of Heterogeneous Microstructure*. 9th International Congress of Croatian Society of Mechanics Book of Abstracts, Split, Croatia: Croatian Society of Mechanics (2018).

- Tonković, Z., Seleš, K., Jurčević, A., Sorić, J. *Crack Propagation Prediction In Heterogeneous Microstructure Of Nodular Cast Iron*. Coexistence of material science and sustainable technology in economic growth, 18th International Foundrymen Conference. Sisak, Croatia (2019) 50-58.

REFERENCES

[1] A.A. Griffith, The phenomena of rupture and flow in solids, Philosophical Transactions of the Royal Society of London Series A 221(582-593) (1921) 163-198.

[2] G.R. Irwin, Fracture Dynamics, Fracturing of Metals, American Society for Metals, Cleveland, (1948) 147-166.

[3] G.R. Irwin, Onset of fast crack propagation in high strength steel and aluminum alloys, Sagamore Research Conference Proceedings, (1956) 289-305.

[4] P.C. Paris, M.P. Gomez, W.E. Anderson, A rational analytic theory of fatigue, The Trend in Engineering 13 (1961) 9−14.

[5] W.D. Callister, D.G. Rethwisch, Materials Science and Engineering, 9th ed., John Wiley & Sons Inc (2014).

[6] G.I. Barenblatt, The mathematical theory of equilibrium cracks in brittle fracture, Advances in Applied Mechanics 7 (1962) 55-129.

[7] D.S. Dugdale, Yielding of steel sheets containing slits, Journal of the Mechanics and Physics of Solids 8(2) (1960) 100-104.

[8] K. Park, G.H. Paulino, Cohesive Zone Models: A Critical Review of Traction-Separation Relationships Across Fracture Surfaces, Applied Mechanics Reviews 64(6) (2011) 20.

[9] F. Zhou, J.F. Molinari, Dynamic crack propagation with cohesive elements: a methodology to address mesh dependency, International Journal for Numerical Methods in Engineering 59(1) (2004) 1-24.

[10] N. Chandra, H. Li, C. Shet, H. Ghonem, Some issues in the application of cohesive zone models for metal-ceramic interfaces, International Journal of Solids and Structures 39(10) (2002) 2827-2855.

[11] M. Elices, G.V. Guinea, J. Gomez, J. Planas, The cohesive zone model: advantages, limitations and challenges, Engineering Fracture Mechanics 69(2) (2002) 137-163.

[12] A. Tradegard, F. Nilsson, S. Ostlund, FEM-remeshing technique applied to crack growth problems, Computer Methods in Applied Mechanics and Engineering 160(1-2) (1998) 115-131.

[13] A.R. Ingraffea, V. Saouma, Numerical modeling of discrete crack propagation in reinforced and plain concrete, Engineering Application of Fracture Mechanics, Springer, Dordrecht, (1985).

[14] N. Moes, J. Dolbow, T. Belytschko, A finite element method for crack growth without remeshing, International Journal for Numerical Methods in Engineering 46(1) (1999) 131-150.

[15] J. Dolbow, N. Moes, T. Belytschko, Discontinuous enrichment in finite elements with a partition of unity method, Finite Elements in Analysis and Design 36(3-4) (2000) 235-260.

[16] N. Moes, A. Gravouil, T. Belytschko, Non-planar 3D crack growth by the extended finite element and level sets - Part I: Mechanical model, International Journal for Numerical Methods in Engineering 53(11) (2002) 2549-2568.

[17] T. Belytschko, Y.Y. Lu, L. Gu, Crack-propagation by element-free Galerkin methods, Engineering Fracture Mechanics 51(2) (1995) 295-315.

[18] T. Belytschko, Y.Y. Lu, L. Gu, Element-free Galerkin methods, International Journal for Numerical Methods in Engineering 37(2) (1994) 229-256.

[19] I. Babuška, U. Banerjee, J.E. Osborn, Survey of meshless and generalized finite element methods: A unified approach, Acta Numerica 12 (2003) 1-125.

[20] Q. Qian, Y. Zhou, Harmonising Rock Engineering and the Environment, CRC Press (2011).

[21] R. de Borst, Damage, Material Instabilities, and Failure, Encyclopedia of Computational Mechanics (2004).

[22] E.C. Aifantis, On the role of gradients in the localization of deformation and fracture, International Journal of Engineering Science 30(10) (1992) 1279-1299.

[23] R. de Borst, L.J. Sluys, H.-B. Mühlhaus, J. Pamin, Fundamental issues in finite element analyses oflocalization of deformation, Engineering Computations 10(2) (1993) 99-121.

[24] Z.P. Bazant, T.B. Belytschko, Wave-propagation in a strain-softening bar - exact solution, Journal of Engineering Mechanics-Asce 111(3) (1985) 381-389.

[25] Z.P. Bazant, G. Pijaudiercabot, Nonlocal continuum damage, localization instability and convergence, Journal of Applied Mechanics-Transactions of the Asme 55(2) (1988) 287-293.

[26] R.H.J. Peerlings, R. deBorst, W.A.M. Brekelmans, J.H.P. deVree, Gradient enhanced damage for quasi-brittle materials, International Journal for Numerical Methods in Engineering 39(19) (1996) 3391-3403.

[27] Z.P. Bažant, B.H. Oh, Crack band theory for fracture of concrete, Mat. Constr. 16 (1983) 155−177.

[28] Y.D. Li, K.Y. Lee, Fracture analysis in micropolar elasticity: mode-I crack, International Journal of Fracture 156(2) (2009) 179-184.

[29] S. Forest, Micromorphic Approach for Gradient Elasticity, Viscoplasticity, and Damage, Journal of Engineering Mechanics-Asce 135(3) (2009) 117-131.

[30] A. Simone, H. Askes, L.J. Sluys, Incorrect initiation and propagation of failure in non-local and gradient-enhanced media, International Journal of Solids and Structures 41(2) (2004) 351-363.

[31] M.G.D. Geers, R. de Borst, W.A.M. Brekelmans, R.H.J. Peerlings, Strain-based transient-gradient damage model for failure analyses, Computer Methods in Applied Mechanics and Engineering 160(1-2) (1998) 133-153.

[32] G. Pijaudier-Cabot, K. Haidar, J.F. Dube, Non-local damage model with evolving internal length, International Journal for Numerical and Analytical Methods in Geomechanics 28(7-8) (2004) 633-652.

[33] L.H. Poh, G. Sun, Localizing gradient damage model with decreasing interactions, International Journal for Numerical Methods in Engineering 110(6) (2017) 503-522.

[34] F. Putar, J. Soric, T. Lesicar, Z. Tonkovic, Damage modeling employing strain gradient continuum theory, International Journal of Solids and Structures 120 (2017) 171-185.

[35] L. Salvo, P. Cloetens, E. Maire, S. Zabler, J.J. Blandin, J.Y. Buffiere, W. Ludwig, E. Boller, D. Bellet, C. Josserond, X-ray micro-tomography an attractive characterisation technique in materials science, Nuclear Instruments & Methods in Physics Research Section B-Beam Interactions with Materials and Atoms 200 (2003) 273-286.

[36] D.A.H. Hanaor, L. Hu, W.H. Kan, G. Proust, M. Foley, I. Karaman, M. Radovic, Compressive performance and crack propagation in Al alloy/Ti2AlC composites, Materials Science and Engineering a-Structural Materials Properties Microstructure and Processing 672 (2016) 247-256.

[37] K. Akutagwa, K. Yamaguchi, A. Yamamoto, H. Heguri, H. Jinnai, Y. Shinbori, Mesoscopic mechanical analysis of filled elastomer with 3D-Finite Element Analysis and transmission electron microtomography, Rubber Chemistry and Technology 81(2) (2008) 182-189.

[38] C. Sandino, P. Kroliczek, D.D. McErlain, S.K. Boyd, Predicting the permeability of trabecular bone by micro-computed tomography and finite element modeling, Journal of Biomechanics 47(12) (2014) 3129-3134.

[39] A. du Plessis, W.P. Boshoff, A review of X-ray computed tomography of concrete and asphalt construction materials, Construction and Building Materials 199 (2019) 637-651.

[40] T.J. Massart, V. Kouznetsova, R.H.J. Peerlings, M.G.D. Geers, Computational Homogenization for Localization and Damage. Advanced Computational Materials Modeling, in: M. Vaz Junior, E.A.N. de Souza , P.A. Munoz-Rojas (Eds.), Advanced Computational Materials Modeling: From Classical to Multi‐Scale Techniques, Wiley-VCH (2010) 111-164.

[41] V.P. Nguyen, M. Stroeven, L.J. Sluys, Multiscale continuous and discontinuous modeling of heterogeneous materials: A review on recent developments, Journal of Multiscale Modeling 3(4) (2011) 229-270.

[42] M.G.D. Geers, V. Kouznetsova, K. Matouš, J. Yvonnet, Homogenization Methods and Multiscale Modeling: Nonlinear Problems, Encyclopedia of Computational Mechanics Second Edition, John Wiley & Sons, Ltd. (2017).

[43] R. Hill, Elastic properties of reinforced solids - some theoretical principles, Journal of the Mechanics and Physics of Solids 11(5) (1963) 357-372.

[44] I. Temizer, T.I. Zohdi, A numerical method for homogenization in non-linear elasticity, Computational Mechanics 40(2) (2007) 281-298.

[45] C. McVeigh, F. Vernerey, W.K. Liu, L.C. Brinson, Multiresolution analysis for material design, Computer Methods in Applied Mechanics and Engineering 195(37-40) (2006) 5053-5076.

[46] Z. Yuan, J. Fish, Toward realization of computational homogenization in practice, International Journal for Numerical Methods in Engineering 73(3) (2008) 361-380.

[47] I. Ozdemir, W.A.M. Brekelmans, M.G.D. Geers, Computational homogenization for heat conduction in heterogeneous solids, International Journal for Numerical Methods in Engineering 73(2) (2008) 185-204.

[48] I. Ozdemir, W.A.M. Brekelmans, M.G.D. Geers, FE2 computational homogenization for the thermo-mechanical analysis of heterogeneous solids, Computer Methods in Applied Mechanics and Engineering 198(3-4) (2008) 602-613.

[49] L. Kaczmarczyk, C.J. Pearce, N. Bicanic, Scale transition and enforcement of RVE boundary conditions in second-order computational homogenization, International Journal for Numerical Methods in Engineering 74(3) (2008) 506-522.

[50] T. Lesicar, Z. Tonkovic, J. Soric, A second-order two-scale homogenization procedure using C-1 macrolevel discretization, Computational Mechanics 54(2) (2014) 425-441.

[51] T. Lesicar, Z. Tonkovic, J. Soric, Two-scale computational approach using strain gradient theory at microlevel, International Journal of Mechanical Sciences 126 (2017) 67-78.

[52] J. Lemaitre, A Course on Damage Mechanics, 2nd ed., Springer (1996).

[53] S. Murakami, Continuum damage mechanics: A Continuum Mechanics Approach to the Analysis of Damage and Fracture, 1st ed., Springer Netherlands (2012).

[54] P.R. Budarapu, X.Y. Zhuang, T. Rabczuk, S.P.A. Bordas, Multiscale modeling of material failure: Theory and computational methods, Advances in Crystals and Elastic Metamaterials, Pt 2 52 (2019) 1-103.

[55] F. Putar, J. Soric, T. Lesicar, Z. Tonkovic, A Multiscale Method for Damage Analysis of Quasi-Brittle Heterogeneous Materials, Cmes-Computer Modeling in Engineering & Sciences 120(1) (2019) 123-156.

[56] V.G. Kouznetsova, M.G.D. Geers, W.A.M. Brekelmans, Multi-scale second-order computational homogenization of multi-phase materials: a nested finite element solution strategy, Computer Methods in Applied Mechanics and Engineering 193(48-51) (2004) 5525-5550.

[57] T. Belytschko, S. Loehnert, J.-H. Song, Multiscale aggregating discontinuities: A method for circumventing loss of material stability, International Journal for Numerical Methods in Engineering 73(6) (2008) 869-894.

[58] T. Hettich, A. Hund, E. Ramm, Modeling of failure in composites by X-FEM and level sets within a multiscale framework, Computer Methods in Applied Mechanics and Engineering 197(5) (2008) 414-424.

[59] V.P. Nguyen, M. Stroeven, L.J. Sluys, An enhanced continuous-discontinuous multiscale method for modeling mode-I cohesive failure in random heterogeneous quasi-brittle materials, Engineering Fracture Mechanics 79 (2012) 78-102.

[60] V.P. Nguyen, O. Lloberas-Valls, M. Stroeven, L.J. Sluys, On the existence of representative volumes for softening quasi-brittle materials - A failure zone averaging scheme, Computer Methods in Applied Mechanics and Engineering 199(45-48) (2010) 3028-3038.

[61] V.P. Nguyen, O. Lloberas-Valls, M. Stroeven, L.J. Sluys, Homogenization-based multiscale crack modelling: From micro-diffusive damage to macro-cracks, Computer Methods in Applied Mechanics and Engineering 200(9-12) (2011) 1220-1236.

[62] V. Hakim, A. Karma, Laws of crack motion and phase-field models of fracture, Journal of the Mechanics and Physics of Solids 57(2) (2009) 342-368.

[63] H. Henry, H. Levine, Dynamic instabilities of fracture under biaxial strain using a phase field model, Physical Review Letters 93(10) (2004) 4.

[64] V.L. Ginzburg, L.D. Landau, On the theory of superconductivity, Zh. Eksp. Teor. Fiz 20 (1950) 1064-1082 (English translation in: L. D. Landau, "Collected papers," Oxford: Pergamon Press (1965), 546.).

[65] G.A. Francfort, J.J. Marigo, Revisiting brittle fracture as an energy minimization problem, Journal of the Mechanics and Physics of Solids 46(8) (1998) 1319-1342.

[66] D. Mumford, J. Shah, Optimal approximations by piecewise smooth functions and associated variational-problems, Communications on Pure and Applied Mathematics 42(5) (1989) 577-685.

[67] B. Bourdin, G.A. Francfort, J.J. Marigo, Numerical experiments in revisited brittle fracture, Journal of the Mechanics and Physics of Solids 48(4) (2000) 797-826.

[68] B. Bourdin, G.A. Francfort, J.J. Marigo, The variational approach to fracture, Journal of Elasticity 91(1-3) (2008) 5-148.

[69] L. Ambrosio, V.M. Tortorelli, Approximation of functionals depending on jumps by elliptic functionals via gamma-convergence, Communications on Pure and Applied Mathematics 43(8) (1990) 999-1036.

[70] R. de Borst, C.V. Verhoosel, Gradient damage vs phase-field approaches for fracture: Similarities and differences, Computer Methods in Applied Mechanics and Engineering 312 (2016) 78-94.

[71] C. Miehe, F. Welschinger, M. Hofacker, Thermodynamically consistent phase-field models of fracture: Variational principles and multi-field FE implementations, International Journal for Numerical Methods in Engineering 83(10) (2010) 1273-1311.

[72] C. Miehe, M. Hofacker, F. Welschinger, A phase field model for rate-independent crack propagation: Robust algorithmic implementation based on operator splits, Computer Methods in Applied Mechanics and Engineering 199(45-48) (2010) 2765-2778.

[73] C. Kuhn, A. Schluter, R. Muller, On degradation functions in phase field fracture models, Computational Materials Science 108 (2015) 374-384.

[74] M.J. Borden, T.J.R. Hughes, C.M. Landis, C.V. Verhoosel, A higher-order phase-field model for brittle fracture: Formulation and analysis within the isogeometric analysis framework, Computer Methods in Applied Mechanics and Engineering 273 (2014) 100-118.

[75] S. Teichtmeister, D. Kienle, F. Aldakheel, M.A. Keip, Phase field modeling of fracture in anisotropic brittle solids, International Journal of Non-Linear Mechanics 97 (2017) 1-21.

[76] M.J. Borden, C.V. Verhoosel, M.A. Scott, T.J.R. Hughes, C.M. Landis, A phase-field description of dynamic brittle fracture, Computer Methods in Applied Mechanics and Engineering 217 (2012) 77-95.

[77] M. Hofacker, C. Miehe, Continuum phase field modeling of dynamic fracture: variational principles and staggered FE implementation, International Journal of Fracture 178(1-2) (2012) 113-129.

[78] C. Steinke, K. Ozenc, G. Chinaryan, M. Kaliske, A comparative study of the r-adaptive material force approach and the phase-field method in dynamic fracture, International Journal of Fracture 201(1) (2016) 97-118.

[79] M. Ambati, T. Gerasimov, L. De Lorenzis, A review on phase-field models of brittle fracture and a new fast hybrid formulation, Computational Mechanics 55(2) (2015) 383-405.

[80] C. Miehe, F. Aldakheel, A. Raina, Phase field modeling of ductile fracture at finite strains: A variational gradient-extended plasticity-damage theory, International Journal of Plasticity 84 (2016) 1-32.

[81] C. Miehe, S. Teichtmeister, F. Aldakheel, Phase-field modelling of ductile fracture: a variational gradient-extended plasticity-damage theory and its micromorphic regularization, Philosophical Transactions of the Royal Society a-Mathematical Physical and Engineering Sciences 374(2066) (2016) 18.

[82] M.J. Borden, T.J.R. Hughes, C.M. Landis, A. Anvari, I.J. Lee, A phase-field formulation for fracture in ductile materials: Finite defonnation balance law derivation, plastic degradation,

and stress triaxiality effects, Computer Methods in Applied Mechanics and Engineering 312 (2016) 130-166.

[83] M. Ambati, T. Gerasimov, L. De Lorenzis, Phase-field modeling of ductile fracture, Computational Mechanics 55(5) (2015) 1017-1040.

[84] R. Alessi, J.J. Marigo, S. Vidoli, Gradient damage models coupled with plasticity: Variational formulation and main properties, Mechanics of Materials 80 (2015) 351-367.

[85] F. Aldakheel, P. Wriggers, C. Miehe, A modified Gurson-type plasticity model at finite strains: formulation, numerical analysis and phase-field coupling, Computational Mechanics 62(4) (2018) 815-833.

[86] M. Dittmann, F. Aldakheel, J. Schulte, P. Wriggers, C. Hesch, Variational phase-field formulation of non-linear ductile fracture, Computer Methods in Applied Mechanics and Engineering 342 (2018) 71-94.

[87] R. Alessi, M. Ambati, T. Gerasimov, S. Vidoli, L. De Lorenzis, Comparison of Phase-Field Models of Fracture Coupled with Plasticity, in: E. Oñate, D. Peric, E. de Souza Neto, M. Chiumenti (Eds.), Advances in Computational Plasticity. Computational Methods in Applied Sciences, Springer, Cham (2018).

[88] C. Miehe, L.M. Schanzel, H. Ulmer, Phase field modeling of fracture in multi-physics problems. Part I. Balance of crack surface and failure criteria for brittle crack propagation in thermo-elastic solids, Computer Methods in Applied Mechanics and Engineering 294 (2015) 449-485.

[89] P. Sicsic, J.J. Marigo, C. Maurini, Initiation of a periodic array of cracks in the thermal shock problem: A gradient damage modeling, Journal of the Mechanics and Physics of Solids 63 (2014) 256-284.

[90] M. Dittmann, F. Aldakheel, J. Schulte, F. Schmidt, M. Kruger, P. Wriggers, C. Hesch, Phase-field modeling of porous-ductile fracture in non-linear thermo-elasto-plastic solids, Computer Methods in Applied Mechanics and Engineering 361 (2020).

[91] M.F. Wheeler, T. Wick, W. Wollner, An augmented-Lagrangian method for the phase-field approach for pressurized fractures, Computer Methods in Applied Mechanics and Engineering 271 (2014) 69-85.

[92] K.C. Li, S.W. Zhou, Numerical investigation of multizone hydraulic fracture propagation in porous media: New insights from a phase field method, Journal of Natural Gas Science and Engineering 66 (2019) 42-59.

[93] C. Miehe, F. Welschinger, M. Hofacker, A phase field model of electromechanical fracture, Journal of the Mechanics and Physics of Solids 58(10) (2010) 1716-1740.

[94] T. Cajuhi, L. Sanavia, L. De Lorenzis, Phase-field modeling of fracture in variably saturated porous media, Computational Mechanics 61(3) (2018) 299-318.

[95] T. Wu, L. De Lorenzis, A phase-field approach to fracture coupled with diffusion, Computer Methods in Applied Mechanics and Engineering 312 (2016) 196-223.

[96] M. Kr?ger, M. Dittmann, F. Aldakheel, A. H?rtel, P. Wriggers, C. Hesch, Porous-ductile fracture in thermo-elasto-plastic solids with contact applications, Computational Mechanics 65(4) (2020) 941-966.

[97] C. Miehe, D. Kienle, F. Aldakheel, S. Teichtmeister, Phase field modeling of fracture in porous plasticity: A variational gradient-extended Eulerian framework for the macroscopic analysis of ductile failure, Computer Methods in Applied Mechanics and Engineering 312 (2016) 3-50.

[98] D. Kienle, F. Aldakheel, M.A. Keip, A finite-strain phase-field approach to ductile failure of frictional materials, International Journal of Solids and Structures 172 (2019) 147-162.

[99] M.A. Keip, B. Kiefer, J. Schroder, C. Linder, Special Issue on Phase Field Approaches to Fracture In Memory of Professor Christian Miehe (1956-2016), Computer Methods in Applied Mechanics and Engineering 312 (2016) 1-2.

[100] L. De Lorenzis, T. Gerasimov, Numerical Implementation of Phase-Field Models of Brittle Fracture, in: L. De Lorenzis, D. A. (Eds.), Modeling in Engineering Using Innovative Numerical Methods for Solids and Fluids (2020) 75-101.

[101] T.T. Nguyen, J. Yvonnet, M. Bornert, C. Chateau, K. Sab, R. Romani, R. Le Roy, On the choice of parameters in the phase field method for simulating crack initiation with experimental validation, International Journal of Fracture 197(2) (2016) 213-226.

[102] K.H. Pham, K. Ravi-Chandar, C.M. Landis, Experimental validation of a phase-field model for fracture, International Journal of Fracture 205(1) (2017) 83-101.

[103] S.W. Zhou, X.Y. Zhuang, H.H. Zhu, T. Rabczuk, Phase field modelling of crack propagation, branching and coalescence in rocks, Theoretical and Applied Fracture Mechanics 96 (2018) 174-192.

[104] J. Bleyer, R. Alessi, Phase-field modeling of anisotropic brittle fracture including several damage mechanisms, Computer Methods in Applied Mechanics and Engineering 336 (2018) 213-236.

[105] M. Ambati, R. Kruse, L. De Lorenzis, A phase-field model for ductile fracture at finite strains and its experimental verification, Computational Mechanics 57(1) (2016) 149-167.

[106] T.T. Nguyen, J. Yvonnet, Q.Z. Zhu, M. Bornert, C. Chateau, A phase field method to simulate crack nucleation and propagation in strongly heterogeneous materials from direct imaging of their microstructure, Engineering Fracture Mechanics 139 (2015) 18-39.

[107] K. Seles, A. Jurcevic, Z. Tonkovic, J. Soric, Crack propagation prediction in heterogeneous microstructure using an efficient phase-field algorithm, Theoretical and Applied Fracture Mechanics 100 (2019) 289-297.

[108] K. Seleš, T. Lesičar, Z. Tonković, J. Sorić, A Phase Field Staggered Algorithm for Fracture Modeling in Heterogeneous Microstructure, Key Engineering Materials 774 (2018) 632-637.

[109] P. Chakraborty, P. Sabharwall, M.C. Carroll, A phase-field approach to model multi-axial and microstructure dependent fracture in nuclear grade graphite, Journal of Nuclear Materials 475 (2016) 200-208.

[110] P. Chakraborty, Y.F. Zhang, M.R. Tonks, Multi-scale modeling of microstructure dependent intergranular brittle fracture using a quantitative phase-field based method, Computational Materials Science 113 (2016) 38-52.

[111] F. Aldakheel, A microscale model for concrete failure in poro-elasto-plastic media, Theoretical and Applied Fracture Mechanics 107 (2020) 9.

[112] R.U. Patil, B.K. Mishra, I.V. Singh, An adaptive multiscale phase field method for brittle fracture, Computer Methods in Applied Mechanics and Engineering 329 (2018) 254-288.

[113] G. Zi, J.H. Song, E. Budyn, S.H. Lee, T. Belytschko, A method for growing multiple cracks without remeshing and its application to fatigue crack growth, Modelling and Simulation in Materials Science and Engineering 12(5) (2004) 901-915.

[114] Z.S. Hosseini, M. Dadfarnia, B.P. Somerday, P. Sofronis, R.O. Ritchie, On the theoretical modeling of fatigue crack growth, Journal of the Mechanics and Physics of Solids 121 (2018) 341-362.

[115] R. Branco, F.V. Antunes, J.D. Costa, A review on 3D-FE adaptive remeshing techniques for crack growth modelling, Engineering Fracture Mechanics 141 (2015) 170-195.

[116] J.L. Boldrini, E.A.B. de Moraes, L.R. Chiarelli, F.G. Fumes, M.L. Bittencourt, A non-isothermal thermodynamically consistent phase field framework for structural damage and fatigue, Computer Methods in Applied Mechanics and Engineering 312 (2016) 395-427.

[117] M. Caputo, M. Fabrizio, Damage and fatigue described by a fractional derivative model, Journal of Computational Physics 293 (2015) 400-408.

[118] G. Amendola, M. Fabrizio, J.M. Golden, Thermomechanics of damage and fatigue by a phase field model, Journal of Thermal Stresses 39(5) (2016) 487-499.

[119] R. Alessi, S. Vidoli, L. De Lorenzis, A phenomenological approach to fatigue with a variational phase-field model: The one-dimensional case, Engineering Fracture Mechanics 190 (2018) 53-73.

[120] P. Carrara, M. Ambati, R. Alessi, L. De Lorenzis, A framework to model the fatigue behavior of brittle materials based on a variational phase-field approach, Computer Methods in Applied Mechanics and Engineering 361 (2020) 29.

[121] M. Seiler, T. Linse, P. Hantschke, M. Kastner, An efficient phase-field model for fatigue fracture in ductile materials, Engineering Fracture Mechanics 224 (2020) 15.

[122] C.V. Verhoosel, J.J.C. Remmers, M.A. Gutierrez, A dissipation-based arc-length method for robust simulation of brittle and ductile failure, International Journal for Numerical Methods in Engineering 77(9) (2009) 1290-1321.

[123] T. Gerasimov, L. De Lorenzis, A line search assisted monolithic approach for phase-field computing of brittle fracture, Computer Methods in Applied Mechanics and Engineering 312 (2016) 276-303.

[124] T. Wick, Modified Newton methods for solving fully monolithic phase-field quasi-static brittle fracture propagation, Computer Methods in Applied Mechanics and Engineering 325 (2017) 577-611.

[125] T. Heister, M.F. Wheeler, T. Wick, A primal-dual active set method and predictor-corrector mesh adaptivity for computing fracture propagation using a phase-field approach, Computer Methods in Applied Mechanics and Engineering 290 (2015) 466-495.

[126] A. Kopanicakova, R. Krause, A recursive multilevel trust region method with application to fully monolithic phase-field models of brittle fracture, Computer Methods in Applied Mechanics and Engineering 360 (2020) 29.

[127] G. Molnar, A. Gravouil, 2D and 3D Abaqus implementation of a robust staggered phase-field solution for modeling brittle fracture, Finite Elements in Analysis and Design 130 (2017) 27-38.

[128] G.W. Liu, Q.B. Li, M.A. Msekh, Z. Zuo, Abaqus implementation of monolithic and staggered schemes for quasi-static and dynamic fracture phase-field model, Computational Materials Science 121 (2016) 35-47.

[129] C. Hesch, K. Weinberg, Thermodynamically consistent algorithms for a finite-deformation phase-field approach to fracture, International Journal for Numerical Methods in Engineering 99(12) (2014) 906-924.

[130] F.P. Duda, A. Ciarbonetti, P.J. Sanchez, A.E. Huespe, A phase-field/gradient damage model for brittle fracture in elastic-plastic solids, International Journal of Plasticity 65 (2015) 269-296.

[131] P. Farrell, C. Maurini, Linear and nonlinear solvers for variational phase-field models of brittle fracture, International Journal for Numerical Methods in Engineering 109(5) (2017) 648-667.

[132] K. Seleš, T. Lesičar, Z. Tonković, J. Sorić, A residual control staggered solution scheme for the phase-field modeling of brittle fracture, Engineering Fracture Mechanics (2018).

[133] K. Seleš, Abaqus Code for a Residual Control Staggered Solution Scheme for the Phase-Field Modeling of Brittle and Ductile Fracture, version 4, Mendeley Data, 2020. url: https://data.mendeley.com/datasets/p77tsyrbx2/4, doi: 10.17632/p77tsyrbx2.4.

[134] H. Amor, J.J. Marigo, C. Maurini, Regularized formulation of the variational brittle fracture with unilateral contact: Numerical experiments, Journal of the Mechanics and Physics of Solids 57(8) (2009) 1209-1229.

[135] A. Mesgarnejad, B. Bourdin, M.M. Khonsari, Validation simulations for the variational approach to fracture, Computer Methods in Applied Mechanics and Engineering 290 (2015) 420-437.

[136] J.J. Marigo, C. Maurini, K. Pham, An overview of the modelling of fracture by gradient damage models, Meccanica 51(12) (2016) 3107-3128.

[137] T. Gerasimov, L. De Lorenzis, On penalization in variational phase-field models of brittle fracture, Computer Methods in Applied Mechanics and Engineering 354 (2019) 990-1026.

[138] S. Burke, C. Ortner, E. Suli, An adaptive finite element approximation of a variational model of brittle fracture, Siam Journal on Numerical Analysis 48(3) (2010) 980-1012.

[139] S. Nagaraja, M. Elhaddad, M. Ambati, S. Kollmannsberger, L.D. Lorenzis, E. Rank, Phase-field modeling of brittle fracture with multi-level hp-FEM and the finite cell method, Computational mechanics 63 (2018) 1283 − 1300.

[140] M. Klinsmann, D. Rosato, M. Kamlah, R.M. McMeeking, An assessment of the phase field formulation for crack growth, Computer Methods in Applied Mechanics and Engineering 294 (2015) 313-330.

[141] N. Noii, F. Aldakheel, T. Wick, P. Wriggers, An adaptive global-local approach for phase-field modeling of anisotropic brittle fracture, Computer Methods in Applied Mechanics and Engineering 361 (2020).

[142] B. Bourdin, mef90. url: https://github.com/bourdin/mef90, doi: 10.5281/zenodo.3242132.

[143] M.S. Alnaes, J. Blechta, J. Hake, A. Johansson, B. Kehlet, A. Logg, C. Richardson, J. Ring, R.M. E., G.N. Wells, The FEniCS Project Version 1.5, Archive of Numerical Software 3 (2015) 9-23.

[144] W. Bangerth, D. Davydov, T. Heister, L. Heltai, G. Kanschat, M. Kronbichler, M. Maier, B. Turcksin, D. Wells, The deal.II Library, Version 8.4, Journal of Numerical Mathematics 24(3) (2016) 135-141.

[145] Abaqus 6.14-1, Dassault Systemes Simulia Corp., Providence, RI, USA, (2014).

[146] M.A. Msekh, J.M. Sargado, M. Jamshidian, P.M. Areias, T. Rabczuk, Abaqus implementation of phase-field model for brittle fracture, Computational Materials Science 96 (2015) 472-484.

[147] U. Pillai, Y. Heider, B. Markert, A diffusive dynamic brittle fracture model for heterogeneous solids and porous materials with implementation using a user-element subroutine, Computational Materials Science 153 (2018) 36-47.

[148] S. Bhowmick, G.R. Liu, Three Dimensional CS-FEM Phase-Field Modeling Technique for Brittle Fracture in Elastic Solids, Applied Sciences-Basel 8(12) (2018).

[149] J.G. Fang, C.Q. Wu, T. Rabczuk, C. Wu, C.G. Ma, G.Y. Sun, Q. Li, Phase field fracture in elasto-plastic solids: Abaqus implementation and case studies, Theoretical and Applied Fracture Mechanics 103 (2019).

[150] P. Zhang, X.F. Hu, X.Y. Wang, W.A. Yao, An iteration scheme for phase field model for cohesive fracture and its implementation in Abaqus, Engineering Fracture Mechanics 204 (2018) 268-287.

[151] J.Y. Wu, Y.L. Huang, V.P. Nguyen, On the BFGS monolithic algorithm for the unified phase field damage theory, Computer Methods in Applied Mechanics and Engineering 360 (2020).

[152] J.Y. Wu, Y.L. Huang, Comprehensive implementations of phase-field damage models in Abaqus, Theoretical and Applied Fracture Mechanics 106 (2020) 21.

[153] K. Pham, H. Amor, J.J. Marigo, C. Maurini, Gradient Damage Models and Their Use to Approximate Brittle Fracture, International Journal of Damage Mechanics 20(4) (2011) 618-652.

[154] J.M. Sargado, E. Keilegavlen, I. Berre, J.M. Nordbotten, High-accuracy phase-field models for brittle fracture based on a new family of degradation functions, Journal of the Mechanics and Physics of Solids 111 (2018) 458-489.

[155] C. Steinke, M. Kaliske, A phase-field crack model based on directional stress decomposition, Computational Mechanics 63(5) (2019) 1019-1046.

[156] K. Seleš, Z. Tonković, A. Jurčević, J. Sorić, Strain Energy Decomposition Influence in the Phase Field Crack Modelling at the Microstructural Level of Heterogeneous Materials, Key Engineering Materials 827 (2019) 482-487.

[157] F. Freddi, G. Royer-Carfagni, Regularized variational theories of fracture: A unified approach, Journal of the Mechanics and Physics of Solids 58(8) (2010) 1154-1174.

[158] J.Y. Wu, V.P. Nguyen, H. Zhou, Y.L. Huang, A variationally consistent phase-field anisotropic damage model for fracture, Computer Methods in Applied Mechanics and Engineering 358 (2020) 28.

[159] F. Aldakheel, B. Hudobivnik, A. Hussein, P. Wriggers, Phase-field modeling of brittle fracture using an efficient virtual element scheme, Computer Methods in Applied Mechanics and Engineering (2018).

[160] C. Miehe, M. Hofacker, L.M. Schanzel, F. Aldakheel, Phase field modeling of fracture in multi-physics problems. Part II. Coupled brittle-to-ductile failure criteria and crack propagation in thermo-elastic-plastic solids, Computer Methods in Applied Mechanics and Engineering 294 (2015) 486-522.

[161] F. Aldakheel, B. Hudobivnik, P. Wriggers, Virtual element formulation for phase-field modeling of ductile fracture, International Journal for Multiscale Computational Engineering 17(2) (2019) 181-200.

[162] R. Alessi, J.J. Marigo, C. Maurini, S. Vidoli, Coupling damage and plasticity for a phase-field regularisation of brittle, cohesive and ductile fracture: One-dimensional examples, International Journal of Mechanical Sciences 149 (2018) 559-576.

[163] J.L. Chaboche, Constitutive equations for cyclic plasticity and cyclic viscoplasticity, International Journal of Plasticity 5(3) (1989) 247-302.

[164] R.G. Forman, S.R. Mettu, Behavior of surface and corner cracks subjected to tensile and bending loads in Ti-6Al-4V alloy, in: H.A. Ernst, A. Saxena, D.L. McDowell (Eds.) Fracture Mechanics: 22nd Symposium, American Society for Testing and Materials, Philadelphia, (1992) 519−546.

[165] D. Cojocaru, A.M. Karlsson, A simple numerical method of cycle jumps for cyclically loaded structures, International Journal of Fatigue 28(12) (2006) 1677-1689.

[166] J. Vignollet, S. May, R. de Borst, C.V. Verhoosel, Phase-field models for brittle and cohesive fracture, Meccanica 49(11) (2014) 2587-2601.

[167] B. Winkler, G. Hofstetter, G. Niederwanger, Experimental verification of a constitutive model for concrete cracking, Proceedings of the Institution of Mechanical Engineers Part L-Journal of Materials-Design and Applications 215(L2) (2001) 75-86.

[168] A.R. Ingraffea, M. Grigoriu, Probabilistic fracture mechanics: a validation of predictive capability, Technical report, (1990) 155.

[169] T.N. Bittencourt, P.A. Wawrzynek, A.R. Ingraffea, J.L. Sousa, Quasi-automatic simulation of crack propagation for 2D LEFM problems, Engineering Fracture Mechanics 55(2) (1996) 321-334.

[170] H. Li, M.W. Fu, J. Lu, H. Yang, Ductile fracture: Experiments and computations, International Journal of Plasticity 27(2) (2011) 147-180.

[171] C. Miehe, F. Aldakheel, S. Teichtmeister, Phase-field modeling of ductile fracture at finite strains: A robust variational-based numerical implementation of a gradient-extended theory by micromorphic regularization, International Journal for Numerical Methods in Engineering 111(9) (2017) 816-863.

[172] B.L. Boyce, S.L.B. Kramer, H.E. Fang, T.E. Cordova, M.K. Neilsen, K. Dion, A.K. Kaczmarowski, E. Karasz, L. Xue, A.J. Gross, A. Ghahremaninezhad, K. Ravi-Chandar, S.P. Lin, S.W. Chi, J.S. Chen, E. Yreux, M. Ruter, D. Qian, Z. Zhou, S. Bhamare, D.T. O'Connor, S. Tang, K.I. Elkhodary, J. Zhao, J.D. Hochhalter, A.R. Cerrone, A.R. Ingraffea, P.A. Wawrzynek, B.J. Carter, J.M. Emery, M.G. Veilleux, P. Yang, Y. Gan, X. Zhang, Z. Chen, E. Madenci, B. Kilic, T. Zhang, E. Fang, P. Liu, J. Lua, K. Nahshon, M. Miraglia, J. Cruce, R. DeFrese, E.T. Moyer, S. Brinckmann, L. Quinkert, K. Pack, M. Luo, T. Wierzbicki, The Sandia Fracture Challenge: blind round robin predictions of ductile tearing, International Journal of Fracture 186(1-2) (2014) 5-68.

[173] A.J. Gross, K. Ravi-Chandar, Prediction of ductile failure using a local strain-to-failure criterion, International Journal of Fracture 186(1-2) (2014) 69-91.

[174] P. Canzar, Experimental and numerical modelling of fatigue behavior of nodular cast iron, doctoral thesis (in croatian), Faculty of Mechanical Engineering and Naval Architecture, University of Zagreb (2012).

[175] P. Canzar, Z. Tonkovic, J. Kodvanj, Microstructure influence on fatigue behaviour of nodular cast iron, Materials Science and Engineering a-Structural Materials Properties Microstructure and Processing 556 (2012) 88-99.

[176] ASTM Standard E647: Standard Test Method for Measurement of Fatigue Crack Growth Rates (2002).

[177] T. Andriollo, J. Hattel, On the isotropic elastic constants of graphite nodules in ductile cast iron: Analytical and numerical micromechanical investigations, Mechanics of Materials 96 (2016) 138-150.